ISSN 1407-5806

COMPUTER MODELLING AND NEW TECHNOLOGIES

Volume 14
No 3

2010

Transporta un sakaru institūts
(Transport and Telecommunication Institute)

Computer Modelling and New Technologies

Volume 14, No.3 – 2010

ISSN 1407-5806
ISSN 1407-5814
(On-line: www.tsi.lv)

Riga – 2010

Host Organization:
Transport and Telecommunication Institute

Supporting Organizations:
Latvian Transport Development and Education Association
Latvian Academy of Sciences
Latvian Operations Research Society

THE JOURNAL IS DESIGNED FOR PUBLISHING PAPERS CONCERNING THE FOLLOWING FIELDS OF RESEARCH:

- mathematical and computer modelling
- mathematical methods in natural and engineering sciences
- physical and technical sciences
- computer sciences and technologies
- semiconductor electronics and semiconductor technologies
- aviation and aerospace technologies
- electronics and telecommunication
- navigation and radar systems
- telematics and information technologies
- transport and logistics
- economics and management
- social sciences

In journal articles can be presented in English. All articles are reviewed.

EDITORIAL CORRESPONDENCE
Transporta un sakaru institūts (Transport and Telecommunication Institute)
Lomonosova iela 1, LV-1019, Riga, Latvia. Phone: (+371) 67100593. Fax: (+371) 67100535.
E-mail: journal@tsi.lv, www.tsi.lv

COMPUTER MODELLING AND NEW TECHNOLOGIES, 2010, Vol. 14, No.3
ISSN 1407-5806, **ISSN** 1407-5814 (on-line: www.tsi.lv)
Scientific and research journal of Transport and Telecommunication Institute (Riga, Latvia)
The journal is being published since 1996.

CONTENTS

Editors' Remarks

An Astrologer's Song

****

To the Heavens above us
O look and behold
The Planets that love us
All harnessed in gold!
What chariots, what horses
Against us shall bide
While the Stars in their courses
Do fight on our side?

All thought, all desires,
That are under the sun,
Are one with their fires,
As we also are one:
All matter, all spirit,
All fashion, all frame,
Receive and inherit
Their strength from the same.

(Oh, man that deniest
All power save thine own,
Their power in the highest
Is mightily shown.
Not less in the lowest
That power is made clear.
Oh, man, if thou knowest,
What treasure is here!)

Earth quakes in her throes
And we wonder for why!
But the blind planet knows
When her ruler is nigh;
And, attuned since Creation
To perfect accord,
She thrills in her station
And yearns to her Lord.

The waters have risen,
The springs are unbound -
The floods break their prison,
And ravin around.
No rampart withstands 'em,
Their fury will last,
Till the Sign that commands 'em
Sinks low or swings past.

Through abysses unproven
And gulfs beyond thought,
Our portion is woven,
Our burden is brought.
Yet They that prepare it,
Whose Nature we share,
Make us who must bear it
Well able to bear.

Though terrors o'ertake us
We'll not be afraid.
No power can unmake us
Save that which has made.
Nor yet beyond reason
Or hope shall we fall -
All things have their season,
And Mercy crowns all!

Then, doubt not, ye fearful -
The Eternal is King -
Up, heart, and be cheerful,
And lustily sing: -
What chariots, what horses
Against us shall bide
While the Stars in their courses
Do fight on our side?

****

Rudyard Kipling, (1865–1936)[1]

[1] Rudyard Kipling (1865-1936) was born in India at the time of the British Empire. His father was the Headmaster of a school in Bombay, and Kipling was sent at age six to a boarding school in England. He returned to India in 1882, and began work as a journalist on the 'Civil and Military' Gazette, while quickly gaining a reputation as a great writer. Kipling stands as a literary giant with a whole host of classic books to his name such as *Kim*, and *The Jungle Book.* Of his many poems the most famous is probably *'If'*, which the encapsulation of a mini-degree course in human psychology is even today. He received the Nobel Prize for literature in 1907, and when he died, he was buried in Poet's corner at Westminster Abbey.

This 14th volume No.3 presents results of researches in fields of **Nanodevices and Nanotechnologies, Material Science, Computer Modelling** and **Computer Technologies.** The innovative researches in the field of applied computer modelling from **India, Israel, Ukraine** are presented in this issue.

Our journal policy is directed on the fundamental and applied sciences researches, which are the basement of a full-scale modelling in practice.

This edition is the continuation of our publishing activities. We hope our journal will be interesting for research community, and we are open for collaboration both in research and publishing. This number continues the current 2010 year of our publishing work. We hope that journal's contributors will consider the collaboration with the Editorial Board as useful and constructive.

EDITORS

Yu.N. Shunin

I.V. Kabashkin

Computer Modelling and New Technologies, 2010, Vol.14, No.3, 7–11
Transport and Telecommunication Institute, Lomonosova 1, LV-1019, Riga, Latvia

GAS SENSOR ARRAYS FOR SPECIAL APPLICATIONS

***D. Fink*[1], *D. Fuks*[2], *A. Kiv*[2], *V. Golovanov*[3]**

[1]*Helmholtz-Center Berlin, Lise-Meitner Campus, 14109, Berlin*
[2]*Department of Materials Engineering, Ben-Gurion University of the Negev, 84105, Israel*
[3]*Department of Physical and Mathematical Modelling, South-Ukrainian National University, 65020, Odessa*

Different types of sensor arrays are discussed. Special cases are indicated when the application of sensor arrays is the only one way to solve the problems of the environment protection and defense. Nanotube sensor arrays are reviewed. New perspectives of the novel sensor arrays creation are connected with the development of the track electronics. The main features of the track electronics are indicated. Principal ways are shown that lead to the development of the multifunctional sensor arrays based on track electronics.

Keywords: *sensor arrays, nanotubes sensors, track electronics*

1. Introduction

One single sensor in many cases cannot give the necessary information to determine the chemical composition of the substances to control, for example of a high-temperature, harsh environment. Last time the nose sensor arrays are composed of sensors designed for high-temperature environments fabricated using micro-electromechanical systems (MEMS) based technology [1]. This array can include a tin-oxide-based sensor doped for nitrogen oxide sensitivity, a SiC-based hydrocarbon sensor, and an oxygen sensor. The individual sensors are different devices (resistors, diodes, and electrochemical cells respectively) and have different responses to the individual gases in the environment. Neural network processing has to be used to integrate and to interpret this information to determine the chemical signatures of harsh, high-temperature environments. At present sensor arrays are necessary to provide the ecological security in the chemical industry, to control the work of power plants, in the cases of the automotive exhaust, the environmental protection, the planetary science, and other situations. A promising way of increasing the selectivity and sensitivity of gas sensors is to treat the signals from a number of different gas sensors with pattern recognition (PARC) methods [1].

The achievements in the field of the nanoscience and nanotechnology led to new possibilities in the creation of sensor arrays. Novel nanomaterials, because of their size, large surface to volume ratio, and properties that differ from their bulk counterparts, promise to offer better performance than micro- and macro-sensors. The perspective nanomaterials include carbon nanotubes (CNTs) [2], inorganic nanowires of high-temperature oxides, semiconducting elements or compounds [3], and quantum dots [4].

An application of the gas sensor array for rapid bioanalysis is presented in [5]. An array of temperature-modulated semiconductor sensors was used to characterize the headspace above a cell culture. The sensor array was capable of detecting changes in the volatile organic compound composition of the headspace above the cultured cells, which can be associated with metabolic changes induced by a chemical compound. This finding suggests the possibility of using cross-selective gas-sensor arrays for analysis of drugs or bioactive molecules through their interaction with cell systems, with the advantage of providing information on their bio-availability.

The wide possibilities in the field of the bioanalysis are opened due to the development of the track electronics [6–10].

2. Nanotube Sensors

CNTs have attracted much attention for physical, chemical, and biosensors due to their interesting physical, electrical, and other properties. In [11] the sensor array is described that consists of carbon nanotubes as sensing material and an interdigitated electrode (IDE) as a transducer. The ability of carbon nanotubes and their derivatives to operate as gas and glucose sensors has been recently demonstrated [12].

In [13] it was the first demonstrated that semiconducting single-wall carbon nanotubes (SWNTs) act as rapid and sensitive chemical sensors at ambient temperature. These authors devised a simple sensing system, in which a single semiconducting SWNT was kept in contact with titanium and/or gold metal pads at the two ends. Using the metal pads as the electrodes for electrical measurements, the authors found that the conductivity of the semiconducting SWNT changed rapidly over several orders of magnitude upon exposure while the conductivity decreased by two orders of magnitude within 2 min upon exposure to 1% NH_3 vapour to nitrogen dioxide and ammonia. In particular, an increase in the conductivity by up to three orders of magnitude was observed within 10 s after exposing the semiconducting SWNT to 200 ppm NO_2.

The electrical conductivity of conjugated polymers can be reliably regulated over a wide range through interactions with electron acceptors and donors [14]. This, together with the fast optical dynamics of most conjugated polymers, has made conjugated polymers very attractive as transducer-active materials. On the other hand, the unusual electronic, mechanical, and thermal properties of carbon nanotubes have also led to their potential use in a wide range of devices, including sensors.

Conductometry is the most commonly used sensing method, in which the change in conductivity of the device is measured. Many processes that lead to changes in carrier density or mobility will cause changes in conductivity. The early work on the conductivity measurements of polyacetylene films upon doping with vapours of iodine, bromine, or AsF_5, and subsequent compensation with NH_3 constitutes the simplest conducting polymer gas sensors [15–17].

Voltammetric sensors generate the sensing response from the redox peak current characteristic of the analyte under a sweep of the electrode voltage over a range of redox potentials associated with the target redox reaction. The conjugated conducting polymer in the voltammetric sensors may act either as a redox-active material to reduce the redox potential for the analyte of interest, and hence reduce the influence of background and interfering currents, or merely as the substrate for immobilizing a redox mediator molecule. Unlike The voltammetric sensors offer an additional advantage with which redox signals for reference molecules added to the sample can be simultaneously measured to improve accuracy [18].

Due to the curvature of the graphene sheet in single-walled carbon nanotubes (SWNTs), the electron clouds change from a uniform distribution around the C–C backbone in graphite to an asymmetric distribution inside and outside the cylindrical sheet of the nanotube. Since the electron clouds are distorted, a rich-electron conjugation forms outside the tube, therefore making the carbon nanotube electrochemically active [19]. These types of electrochemical sensors depend on the transfer of charge from one electrode to another electrode. By measuring the conductivity change of the CNT device, the concentration of the chemical species or gas molecules can be measured. The carbon nanotube sensing devices provide opposite polarities of sensor signals from NO_2 and NH_3 exposures. Surface and bulk modifications of carbon nanotubes can be utilized to improve the selectivity of the carbon nanotube sensors, such as coating the carbon nanotubes with different polymers10 or doping the carbon nanotube with different metal clusters [20–21].

Most biological processes that occur in / or around a living cell are electrostatic or electrochemical in nature, and so sensors and field-effect transistors that use single-walled carbon nanotubes (SWNTs) can be used as sensitive probes for various cell studies. It was shown by researchers at the Kavli Institute of Nanoscience in The Netherlands that SWNT sensors can electrically interrogate the cellular activity of macrophages – a type of cell that scavenges and degrades foreign materials.

The new sensor configuration is described in [22]. A circular disk resonator is used to study the gas sensing properties of carbon nanotubes. It detects the presence of gases based on the change in the dielectric constant rather than electrical conductivity of SWNTs upon gas exposure. A conducting circular disk was coated with electric arc prepared SWNTs and degassed by heating under a high vacuum. It exhibited noticeable shifts in resonant frequency to both polar (NH_3 and CO and nonpolar gases He, Ar, N_2, and O_2). Gas concentrations as low as 100 ppm was detected using this sensor configuration.

While the feasibility of developing chemical and biological sensors based on conjugated polymers and carbon nanotubes for detecting various sophisticated analytes, ranging from gas molecules to glucose, has been clearly demonstrated, the recent research and development of conducting polymer sensor arrays (electronic noses) should, in principle, to identify complex mixture systems even without separation.

3. Sensor Arrays and Track Electronics

Sensor arrays allow solving many complex problems linked to the investigation of hard environmental pollutions, many-component mixture systems and others. These devices become important, in particular, for the controlling of a cleanliness of the sky space in connection with the volcano eruptions [23].

Sensor arrays based on using the SWNTs [19] have the good perspectives for the creation novel sensor devices for multiple applications. But in special cases we have to overcome serious difficulties connected with the necessity to change the physical-chemical properties of the separate groups of nanotubes. In the case of gas sensors, for example, we need the corresponding electron withdrawing properties of nanotubes to impart the selectivity to different pollution molecules.

The structures of the track electronics [6–10] open the new horizons in the development of multifunctional sensor arrays. The track electronics is based on the new types of porous electronic materials [24, 25], so-called "TEMPOS" structures (Tunable Electronic Material in Pores in Oxide on Semiconductors). These structures are artificially created aligned quasi one-dimensional nanosystems. The swift heavy ion irradiation of insulating layers on a semiconducting substrate leaves behind them the so called (latent) ion tracks, which can be filled with various (semi)conducting materials (either in the shape of compact nanowires or nanotubules) after etching them to the desired size and shape. Thus, a multitude of embedded parallel semiconducting pathways can be created that are absent in the classical field electric transistor concept. In contrast to the latter all contacts are connected here conductively as well as capacitively to the device7. It is the independence of the nanowires from each other, which allows one to design intelligent track-to-track interaction strategies, and attain the range of unusual properties of TEMPOS structures among which the most interesting features are the occurrence of the following:

- the tunable diode polarities [26];
- the self-oscillations [27];
- the electroluminescence [28];
- the negative differential resistances (NDR) [29].

The incorporation of suitable materials in etched tracks and on the surface of TEMPOS structures transforms the latter ones to sensors for physical, chemical or biological signals. Sensing properties for many physical-chemical parameters such as light, temperature, magnetic fields, humidity, alcohol and ammonia vapour have already been proven [25, 30]. These parameters can be used to trigger the onset of NDRs [31] and construct active sensing elements with signal amplification up to a factor of ~ 25.

Figure 1 [32] shows the summarized experimental results indicating the possible effects in conducting track networks that are obtained with different materials and accordingly reveal different electronic properties.

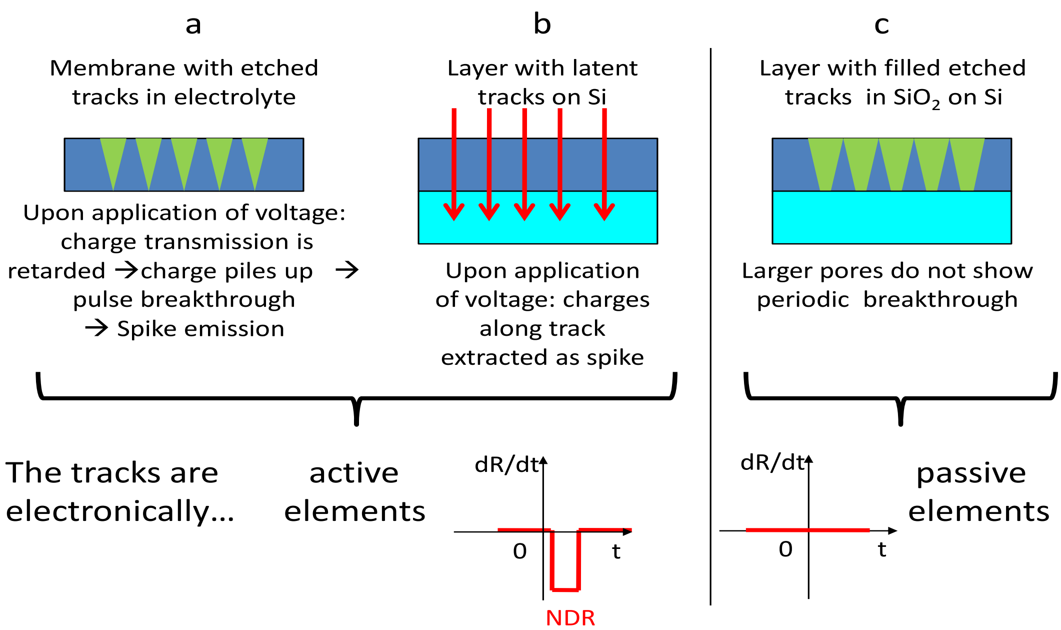

Figure 1. Schematic overview about the different electronic ion track structures [32]

In [32] the electronic behaviour of conducting swift heavy ion track networks is described. Depending on the track construction, they either act as electronically active or passive elements. The individual tracks are found to emit current spikes and interact among themselves leading to phase-locked synchronous coupled oscillations with resulting in complex patterns that are similar to neural networks. The latter case corresponds to networks of electronically passive conducting tracks which have been examined earlier in connection with TEMPOS structures. They show the important feature of becoming overall electronically active through collective interactions.

It is clear that the track structures as “artificially created aligned quasi one-dimensional nanosystems” are more convenient objects to create sensor arrays in comparison with nanotubes structures. These advantages are determined by as follows:

- the possibility to vary the density and the spatial distribution of tracks using the corresponding beam technique;
- the technological simplicity of the incorporation of different substances into the tracks in comparison with the same procedure for nanotubes;
- the possibility to realize the necessary geometry of the regions of tracks incorporated with different materials.

Recently [33] it was shown that in the case of TEMPOS structures the interaction of a network of passive elements with each other can lead to an overall electronically active behaviour of the device which shows up by the emergence of the NDR and the possibility to apply these elements for the construction of amplifiers, oscillators etc.

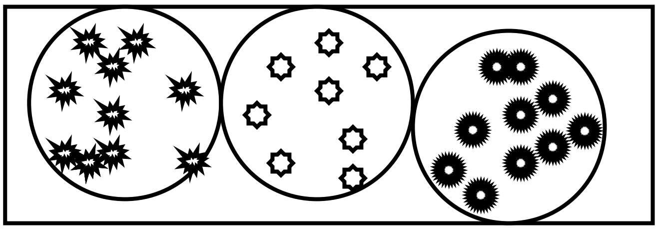

Figure 2. Schematic image of the regions of TEMPOS structure in which tracks are incorporated with different substances

On Figure 2 the regions in TEMPOS structure incorporated with different substances are shown. (We do not consider here the technological aspects of the creation of such device). In each region the incorporated substances are chosen that provide the adsorption of the settled molecules. It means that each region will reveal the sensitivity of the electrical characteristics of the electronic circuit to the certain type of molecule.

To explain the idea of the application of the neural networks models to the track electronic devices we use the simplest integrate-and-fire neural network model [34].

The neuron kinetics is represented in time by equation: $I(t) = C_m \frac{dV_m}{dt}$.

This equation is the time derivative of the law $Q = CV$. When an input current is applied, the membrane voltage increases with time until it reaches a constant threshold, V_{th}, at which point a delta function spike occurs and the voltage is reset to its resting potential, after which the model continues to run. The firing frequency, f of the model thus increases linearly without bound as input current increases.

For each region with the certain filler (Figure 2) we get the corresponding parameters V_{th} and f that can identify the certain molecules. In particular, the different adsorbed molecules lead to the different changes of the input current with corresponding changes of the firing frequencies. These effects may be used for the adsorbed molecules identification.

Acknowledgment

This work has been funded by the Binational Science Foundation (No. 2006056).

References

1. Hunter, G. W., Chung-Chiun, L., Makel, D. B. *Microfabricated Chemical Sensors for Aerospace Applications: The MEMS Handbook / Mohamed Gad-el-Hak, ed.* Boca Raton, FL: CRC Press, 2002. 22–1–22–24
2. Sueiro, J., Zhou, G., Masanori, H. *J.Phys.D:Appl.Phys., Vol.* 36, 2003, L109–L114 (rapid communication).
3. Yuna, M., Myunga, N. V., Vasqueza, R. P. et al. *Nanofabrication Technologies / Ed. E. A. Dobisz: SPIE Proceedings 5220,* 2002.

4. Mosadegh Sedghi, S., Mortazavi, Y., Khodadadi, A., Alizadeh Sahraei, O., Naseh, M. V. Sonochemically Prepared SnO_2 Quantum Dots as a Selective and Low Temperature CO Sensor. World Academy of Science, *Engineering and Technology,* Vol. 49, 2009.
5. Pasini, P., Powar, N., Gutierrez-Osuna, R., Daunert, S., Roda, A. *Analytical and Bioanalytical Chemistry,* Vol. 378, No 1, 2004.
6. Fundamentals of ion irradiated polymers / Ed. D. Fink, *Springer Series in Materials Science*, Vol. 63, 2004 (and references therein).
7. Transport Processes in Ion Irradiated Polymers / Ed. D. Fink, *Springer Series in Materials Science,* Vol. 65, 2004 (and references therein).
8. Fink, D., Kiv, A., Fuks, D. and Chandra, A. Collective Interaction in Ion Track Electronics. In: *Proc. Of the 6th Int. Conf. 'Information Technologies and Management'*, Riga, Latvia, April 10–11, 2008.
9. Ivanovskaya M., Khirunenko L. and Fuks D. *J. Mater.Sci.: Mater. Electron,* Vol. 19, 2008, pp. 1222–1227.
10. Fink, D., Klinkovich, I., Bukelman, O., Marks, R. S., Kiv, A., Fuks, D., Fahrner, W. R., Alfonta, L. *Biosensors & Bioelectronics,* Vol. 24, 2009, pp. 2702–2706.
11. Artzi-Gerlitz, R., Benkstein, K., Lahr, D., Hertz, J., Montgomery, C., Bonevich, J., Semancik, S., Tarlov, M. Fabrication and gas sensing performance of parallel assemblies of metal oxide nanotubes supported by porous aluminium oxide membranes, *Sensors and Actuators* B: Chemical, 2008. On-line from Nov. 11, 2008.
12. Dai, L., Soundarrajan, P., Kim, T. *Pure Appl. Chem,,* Vol. 74, No 9, 2002, pp. 1753–1772.
13. Dai, L., Mau, A. W. H. *Adv. Mater.,* Vol. 13, 2001, p. 899; Li, J., Lu, Y., Ye, Qi, Delzeit, L., Meyyappan, M. *Electrochemical and Solid-State Letters*, Vol. 8, No 11, 2005, H100–H102.
14. Kong, J., Franklin, N. R., Zhou, C., Chapline, M. G., Peng, S., Cho, K., Dai, H. *Science,* Vol. 287, 2000, p. 622.
15. Chien, J. C. W. *Polyacetylene: Chemistry, Physics and Materials Science.* New-York: Academic Press, 1984.
16. Wong, S. S., Joselevich, E., Woolley, A. T., Cheung, C., Lieber, C. M. *Nature*, Vol. 394, 1998, p. 52.
17. Wong, S. S., Woolley, A. T., Joselevich, E., Cheung, C., Lieber, C. M. *J. Am. Chem. Soc.,* Vol. 120, 1998, p. 8557.
18. Fabre, B., Burlet, S., Cespuglio, R., Bidan, G. *J. Electroanal. Chem.* Vol. 426, 1997, pp. 75–83.
19. *Carbon Nanotubes: Science and Applications / Ed. M. Meyyappan,* Boca Raton, FL: CRC Press, 2004.
20. Young, P., Lu, Y., Terrill, R., Li, J. *J. Nanosci. Nanotechnol.,* Vol. 5, 2005, p. 1.
21. Lu, Y., Li, J., Han, J., Ng, H.-T., Binder, C., Partridge, C., Meyyappan, M. *Chem.Phys.Lett.,* Vol. 391, 2004, p. 344.
22. Sundgren, H. et al. *Meas. Sci. Technol.,* Vol. 2, 1991, p. 464; doi: 10.1088/0957–0233/2/5/008
23. http://interceder.net/news/island-ash
24. Hoppe, K., Fahrner, W. R., Fink, D. et al. *Nucl. Instr. Meth. B*, Vol. 266, 2008, pp.1642–1646.
25. Fink, D., Petrov, A., Fahrner, W. R. et al. *Int. Journal of Nanoscience,* Vol. 4 (5–6), 2005, pp. 965–973.
26. Fink, D., Chandra, A., Opitz-Coutureau, J., Fahrner, W. R. et al. *J.Appl.Phys. A,* Vol. 86, 2007, pp. 469–476.
27. Fink, D., Kiv, A., Fuks, D., Golovanov, V. et al. *Applied Physics Letters,* Vol. 91(8), 2007, 083512.
28. Fink, D. et al. In: *Physics, Chemistry and Application of Nano-Structures*. World Scientific Publ., 2005, pp. 474–481.
29. Fink, D., Chadderton, L. T., Kiv, A., Saad, A., Tabacnics, M. *Rad. Eff. Def. Sol.,* Vol. 162 (7–8), 2007, pp. 543–555.
30. Fahrner, W. R., Kiv, A., Fuks, D., Fink, D. et al. (2009); submitted to *J. Appl. Phys. A.*
31. Fink, D., Kiv, A., Golovanov, V. et al. *J. Mater Sci.: Mater. Electron.*, Vol. 19, 2008, pp. 1222–1227.
32. Fink, D., Kiv, A., Fuks, D., Saad, A., Vacík, J., Hnatowicz, V., Chandra, A. *Radiation Effects and Defects in Solids: Incorporating Plasma Science and Plasma Technology,* Vol. 165, Issue 3, 2010, pp. 27–244.
33. Hoppe, K., Fink, D., Fahrner, W. R. *J. Electrochem. Society,* Vol. 155, 2008. K19-K22, P7-P11
34. Abbott, L. F. *Brain Research Bulletin*, 50, Nos. 5/6, 1999, pp. 303–304.

Received on the 21st of April, 2010

Computer Modelling and New Technologies, 2010, Vol.14, No.3, 12–16
Transport and Telecommunication Institute, Lomonosova 1, LV-1019, Riga, Latvia

MECHANISM OF STRENGTHENING OF NANOCRYSTALLINE TUNGSTEN

D. Fuks, A. Kiv, A. Nemtsoff

Department of Materials Engineering, Ben-Gurion University of the Negev
POB 653, Beer-Sheva, Israel

The work is aimed to study the influence of interaction between nanocrystals in nanocrystalline tungsten on its mechanical properties. The modified Molecular Dynamics (MD) technique was used to calculate the potential relief (PR) for the mutual shifting of two nanocrystals inside the nanocrystalline tungsten. We considered two tungsten nanocrystals sliding relatively the common interface with one or two vacancies in the sliding lattice planes. It was found that defects in sliding planes lead to increase of potential barrier for mutual shifting of nanocrystals and thus cause the increase of microscopic "friction" in nanocrystalline material. This means that a creation of point defects in contacting layers of nanocrystals can provide the strengthening of such materials.

Keywords: *nanocrystalline materials (NCM), Molecular Dynamics Simulation*, *mechanical properties of nanocrystalline tungsten*

1. Introduction

Recently nanocrystalline materials (NCM) are widely used for creation of devices with the typical length scale for internal components of the order of nanometres. These materials allow producing nanosensors, nanoelectrical, nanomechanical and other novel devices. New possibilities arise to solve actual problems in high technologies, industry, medicine etc. The service characteristics of NCM have been found to be superior in comparison with properties of conventionally coarse-grained polycrystals.

The ability of nanocrystalline alloys to deform superplastically at lower temperatures and higher strain rates is expected to significantly lower the costs of metal-forming technologies. High strength, ductility, and wear resistance can make the use of nanocrystalline refractory metals and ceramics as parts of high-temperature devices such as engines. Enhanced soft magnetic properties of nanocrystalline alloys, such as the low coercivity and high magnetic permeability, are already in use in transformers. The NSMs have many orders of magnitude higher diffusion coefficient that can find applications, for example, in hydrogen storage technologies. The nanostructured coatings significantly increase the wear resistance of otherwise soft materials. Modified electronic and electric properties of nanostructured metals and covalent ceramics may find wide applications in electronics.

Two main factors are considered to determine the properties of NSMs. First, when the grain diameter approaches a few nanometres, the structure modulation length becomes comparable to the characteristic distances of physical processes in solids and the size effects are pronounced. The second important factor is that a significant volume fraction of NSMs is occupied by the atoms at defect sites, mainly in interfaces. Thus, the atomic structure of interfaces is crucial for the properties of these materials.

2. Molecular Dynamics Simulation

MD is a computer modelling technique where the time evolution of a set of interacting atoms is followed by integrating equations of motion [1–3]. There are several algorithms that are used in MD problems. In this study we realized an accelerated version of *Verlet* algorithm [4]. One of the most important stages of MD application is a choosing the interatomic potential (IAP). We have used the Morse-type IAP, $\Phi(r_{ik})$ [5]. Its parameters were obtained by *ab initio* calculations in [6].

$$\Phi(r_{ik}) = \begin{cases} De^{-2\lambda(r_{ik}-r_0)} - 2De^{-\lambda(r_{ik}-r_0)}, & when\ r_{ik} \le r_{max}, \\ 0, & when\ r_{ik} > r_{max}, \end{cases} \tag{1}$$

where $D = 0.04775\ Ry\ (0.6497\ eV)$ [8] , $\lambda = 0.82330\ a.u.^{-1}$ [8], $r_0 = 5.15278\ a.u.$ [8].

In our calculations the cut-off radius was: $r_{ik} = r_{max} = 3.05\ r_0$. The simulation model was built as a three-dimensional tungsten nanocrystal with 855–997 atoms. Atoms were located in bcc lattice sites of tungsten.

2.1. Description of the Model

First, the bcc lattice of tungsten atoms was constructed. The standard procedure of MD was applied [1]. In the relaxation procedure the total energy of the system was minimized with the accuracy not less than 0.003 *Ry*. To get the final simulation model we used rotational matrices. The model nanocrystal was cut into two parts. One part was rotating using transformation matrix by angle of 180^0 around the [111] axis (Fig. 1).

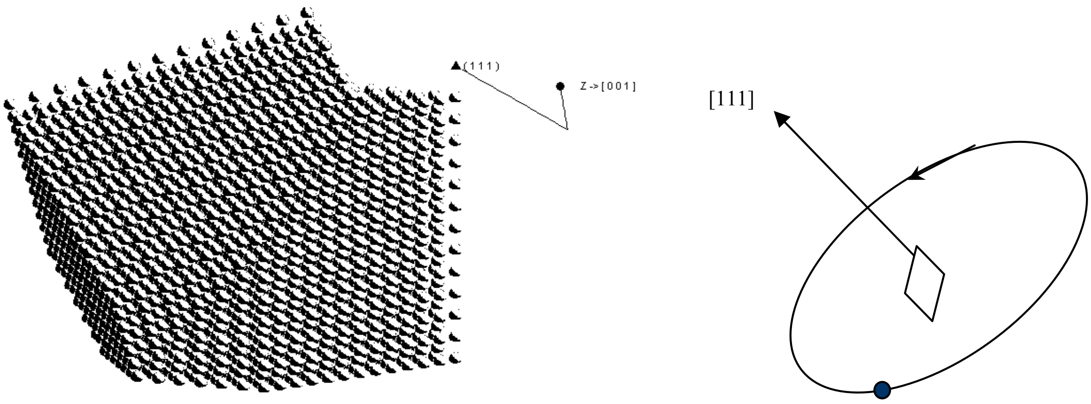

Figure 1. The rotating of the "cut" (top) crystal on (111) plane by 180^0

We proposed a *method of embedded volume* (MEV) and applied it to decrease the calculation time. In our problem the embedded volume is a spherical cluster that is intersected by the contacting plane: each semi-sphere belongs to one of contacting nanocrystals. The embedded sphere contained 120 atoms (~ 12% of the whole system). Such technique provides the decrease of calculation time while preserving the accuracy of results.

MEV consists of three steps:

- Fixing the outer border atoms.
- Relaxation of the entire system of the two contacting nanocrystals.
- Calculating the potential energy only within the embedded spherical volume.

A simulation procedure was performed so that embedded spherical volume and its center remain still. No shifting of half-spheres occurs while one of the nano-crystals is sliding atop another. To study the influence of point defects in the plain of sliding on the interaction between two contacting nanocrystals monovacancies and divacancies have been located in the centre of the embedded spherical volume.

2.2. Calculations of Potential Barriers

Calculations of PB for mutual shifting of two contacting nanocrystals were performed in accordance with the following scheme:

1. Calculation of the total energy of the relaxed model system at the start position: contacted nanocrystals are not shifted.
2. Step by step shifting of contacted nanocrystals along [11–2] direction (x-direction) and calculation of the total energy after relaxation of the system at each step.
3. Determination of the saddle point as a configuration of contacting nanocrystals that corresponds to maximal value of total energy.
4. Determination of PB as a difference between total energies in the start configuration and the saddle point configuration of the model system.
5. Repeating of the same scheme for the system with point defects in the plane of sliding (Σ_3 (111)).

3. Results and Discussion

Figure 2 shows the profile of PB for sliding of the ideal tungsten nanocrystals.

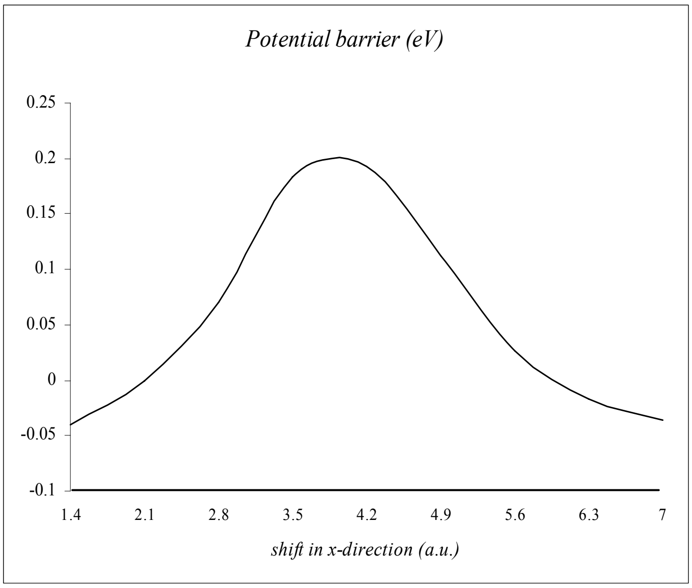

Figure 2. The profile of PB for the ideal tungsten nanocrystals sliding

The result (~ 0.242 eV) is consistent with obtained in [6, 7]. To study the relaxation of atoms in vicinity of the sliding plane the embedded volume was chosen as cylinder. The sliding plane passed through the axis of cylinder. Calculations gave the vertical displacements of atoms inside the embedded cylinder.

The results showed a quasi-periodic dependence of atomic displacements on the distance from the interface. The highest displacements (up to 1.1 a. u.) are in the contacting layers.

As it was mentioned above, a monovacancy defect had been introduced into the middle of the structure of nanocrystals boundary and similar procedures were repeated with the modified structure.

The resultant energy barrier for nanocrystals sliding is presented on Figure 3.

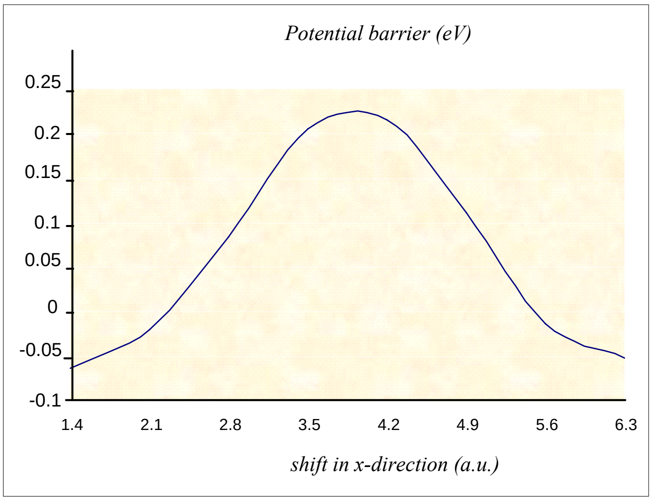

Figure 3. The profile of PB for sliding of tungsten nanocrystals with monovacancy in the interface

The effect of the interface monovacancy can be easily seen from the above figure: the significant raise in the energy barrier of about 15% comparatively to ideal nanocrystals brings to tribologic change that is difficult to ignore. In the same way a divacancy was implanted in the centre of the investigated system (in such a way, that both its parts lie on the nanointerface).

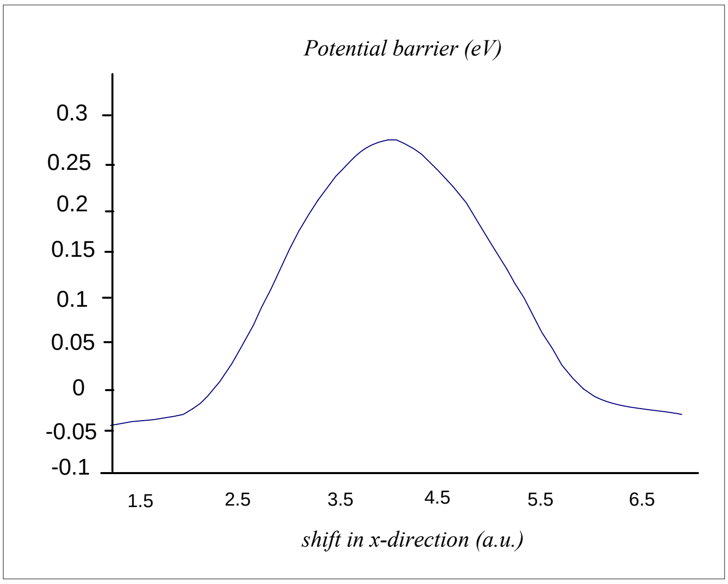

Figure 4. The profile of PB for sliding of tungsten nanocrystals with divacancy in the interface

In the case of divacancy located in sliding plane PB increases by more than 33% (~ 0.076 eV).

4. Discussion and Conclusions

To characterize the interaction of contacting nano-particles we introduce the term “nano-grains friction”. The “tribological” characteristics of nano-crystals can be considered using the analogy with corresponding characteristics of macroscopic surfaces. We concluded that such approach is fruitful for understanding the mechanisms of strengthening of nano-crystal materials. Thus the friction of contacting surfaces of nano-particles should determine mechanical properties of nano-materials. To achieve the main goal of the work we worked out original approaches concerning:

- The design of the two-particle model for the nanoparticles sliding for the further MD simulation;
- Using of the embedded relaxation volume in the interface region for a simplification of the calculation procedure;
- The way of introducing the surface vacancies and their complexes into the model.

In order to obtain the most common results we have chosen in our MD simulation procedure the effective Morse-type potential that has a typical form of the most of known potentials. For our case of tungsten particles simulation we used the potential parameters obtained in *ab initio* calculations [6].

The main result of our work is the increase of the potential barrier (PB) for the nanoparticles sliding in the case of point defects existing in the contacting surfaces. In fact it means that we observe the strengthening effect in nanocrystal material caused by the defect structure of nanoparticles. The increase of PB is of the 15–30% and even more in comparison with sliding of “ideal” nanoparticles (without surface defects). It is reasonable to believe that this result does not depend on the features of the model and on the type of potential due to large enough changes in the value of PB and due to the choice of the common enough potential form.

Thus summing up we can claim that:

- The consideration of “tribological” properties of nanoparticles is a fruitful approach in investigations and predictions of mechanical properties of nanocrystal materials.
- Point defects in contacting layers of tungsten particles led to the significant increase of their “friction” and thus to the strengthening of material.
- Using different ways of creation of point defects in nanomaterials (γ- and X-ray irradiation, thermal treatment etc.) one can expect their strengthening or other practically significant effects.

References

1. Grould, H., Tobochnik, J. *An Introduction to Computer Simulation Method.* N-Y: Addison & Wesley Press, 1988.
2. Heerman, D. W. *Computer Simulation Methods in Theoretical Physics.* N-Y: Springer-Verlag, 1986.
3. Nose, S. *Progr. Theor. Phys.*, Suppl. No 103, 1991, pp. 1–46.
4. Verlet, L. *Phys. Rev.,* Vol. 159, 1967, p. 98.
5. Morse, P. M. *Phys. Rev.,* Vol. 34, 1929, p. 57.
6. Dorfman, S., Liubich, V., Fuks, D., Mundim, K. C. *J. Phys.: Condens. Matter,* Vol. 13, 2001, pp. 6719–6740.
7. Fuks, D., Mundim, K., Liubich, V., Dorfman, S. *Composites. Part A,* Vol. 32, 2001, pp. 591–594.

Received on the 11th of July, 2010

Computer Modelling and New Technologies, 2010, Vol.14, No.3, 17–29
Transport and Telecommunication Institute, Lomonosova 1, LV-1019, Riga, Latvia

EFFECT OF SLIDING VELOCITY AND PLASMA SPRAYING PARAMETERS ON WEAR RESISTANCE OF NiCrBSiCFe PLASMA SPRAYED ON AUSTENITIC STAINLESS STEEL AT HIGH TEMPERATURE

N. L. Parthasarathi, M. Duraiselvam**[*]**

Department of Production Engineering, National Institute of Technology
Tiruchirappalli-620 015, Tamil Nadu, India
[*] Phone: +91 431 2503509. Fax: +91 431 2500133

The tribological tests were carried out on AISI 316 austenitic stainless steel (ASS) plasma coated with NiCrBSiCFe alloy powder under two set of plasma spraying parameters (PSP 1 and PSP 2) using a pin-on-disc-apparatus. EN 8 medium carbon steel was used as a counterface material. The tests were carried out at load of 20 N with sliding velocities of 1m/s and 2m/s at room temperature (35°), 150°C, 250°C and 350°C. Metallographic characterization was carried out by optical microscope (OM) and Scanning electron microscope (SEM). Between PSP 1 and PSP2, a stand-off distance of 125 mm (PSP1) was found to be more suitable for producing uniform lamellar microstructure with fewer amounts of pores with better wear resistance. The wear rate at 1m/s was comparatively more than 2m/s due to the adhesive wear and material softening. The worn debris during sliding at 350°C turn in to oxides which further behaves like a protective and lubricative film eliminating the chances of severe material loss. SEM was used to characterise the worn track and to identity the wear mechanism.

Keywords: *AISI 316 ASS, NiCrBSiCFe, sliding velocity, stand-off distance, abrasive wear, plasma spraying*

1. Introduction

Austenitic stainless steels are widely employed in nuclear reactors, biomedical implants, machinery for chemical and food processing industries. In nuclear industries, engineering components namely control rod actuator mechanisms and valves made of stainless steel encountered unlubricated contacts against mild steel at 200°C. The coatings without cobalt (Co60) were preferred for hard facings since it is a major contributor of radiation exposure [1]. As austenitic stainless steels exhibit poor wear resistance, surface modification techniques were used to improve its tribological properties. The interacting solid surfaces with the interfacing materials and environment result in material loss from the surface. Relative sliding between the contacting surfaces leads to the rupture of these junctions and subsequent material transfer from one surface to the other, in addition to the production of debris and material loss. The plasticity-dominated sliding wear prevails at lower sliding velocities [2].

A blasted austenitic stainless steel plate (JIS-SUS304) has been characterized and compared to the scraped and non-blasted specimens. A martensite phase is formed in the surface layer of both blasted and scraped specimens. It is concluded that the deterioration of corrosion resistance of austenitic stainless steel through blasting is caused by the roughed morphology of the surface [3]. Special attention has been paid to NiCrBSi alloys, since they provide an excellent wear and corrosion resistance at high temperatures. The influence of several factors such as load, temperature, presence of reinforcement particles and the type of thermal spray technique on the wear behaviour of NiCrBSi alloy was studied by Rodriguez et al. [4]. The effects of boronizing on plain carbon steel AISI 1018; high-strength alloy steel AISI 4340 and AISI 304 ASS was investigated. The presence of boronized coatings on ferrous alloys improved their microhardness, oxidation resistance and corrosion resistance [5]. TiCrC-FeCr composite coating was deposited on steel and titanium alloy by plasma method. The composition, structure and tribological properties of these coatings are studied in comparison with traditional materials based on the Ni-Cr alloy. Titanium-chromium carbide has greater wear resistance than that of Ni-Cr alloys with almost equal friction coefficients [6]. The sliding wear of AISI 304 and AISI 316 austenitic stainless steels in pin-on-disc equipment was studied as a function of applied load (6-20N) and tangential velocity (0.07–0.81 m/s). Worn surfaces and wear debris were analysed through SEM, XRD, Mossbauer spectroscopy, surface temperature and instrumented indentation.

Results indicated that plasticity-dominated wear (metallic particle oxidation, adhesive and mixed wear) as the sliding wear mechanisms [7]. The influence of a post spray heat treatment on the microstructure, microhardness and abrasive wear behaviour of the flame sprayed Ni-WC coating deposited on the mild steel was studied. As the normal load was increased, the wear rate was also increased. The SEM study indicated that the wear largely takes place by groove formation and scoring of eutectic matrix and the fragmentation of the carbide particles [8].

The influence of the addition of chromium carbide (CrC) particles on the microstructure, micro-hardness and abrasive wear behaviour of flame sprayed NiCrSiB coatings deposited on low carbon steel substrate was studied. The addition of CrC reduces the wear rate from three to eightfold. Wear resistance was greater against coarse abrasives at high loads than against fine abrasives. Heat treatment of both unmodified and CrC modified powder coatings deteriorated the abrasive wear resistance [9]. Ni-Al-SiC feed stock powder containing 12.5% SiC was plasma sprayed on CK 45 steel substrates. The coatings were composed of different intermetallics including Ni-Al and Ni_2Al_3. The mean hardness of the coating was 567 HV.

It was reported that by increasing current density of atmospheric plasma spraying (APS), the coating/substrate adhesive strength was increased [10]. Plasma-sprayed Ni-50% Cr, plasma-sprayed Al_2O_3-13%TiO_2 and high-velocity oxygen-fuel sprayed (HVOF) WC-17%Co coatings for enhancing the wear resistance and the corrosion protectiveness of a diamond-like carbon (DLC)-based thin film were deposited onto a carbon steel substrate. At 300°C, the DLC-based film on the Al_2O_3-13%TiO_2 interlayer offers the best tribological performance due to the increased toughness of the ceramic interlayer at this temperature [11]. Glow discharge (GD) nitrocarburizing, at low carbon content and different working temperatures, was performed on AISI 316L and AISI 304 stainless steels. At working temperatures higher than 400°C, roughness increased and wear was limited to asperity compaction. Wear was reduced by up to a factor of 5 in treated steels [12]. Industrial alternative application to hard chromium plating was proposed as NiCrBSi coating. Tribological characterization was carried out in order to determine the alternative potential of NiCrBSi coatings compared to electrolytic hard chromium plating, in applications to resist wear [13]. NiCrBSi was deposited on 0Cr13Ni5Mo stainless steel using the activated combustion high velocity air fuel (AC-HVAF) technique. The structure and morphologies of the Ni-based coatings were investigated by XRD, SEM and EDS [14].

The present study aims to analyse the influence of sliding velocity and plasma spraying parameters on the high temperature wear properties of NiCrBSiCFe plasma sprayed on AISI 316 ASS. The micro-structure of the coating was studied and the microhardness was measured with respect to the plasma spraying parameters. The worn surface morphology were examined by SEM and correlated with the experimental results.

2. Experimental Procedure

2.1. Materials

AISI 316 ASS in as-received condition was used as a substrate by machining to a dimension of 100 mm diameter with 4mm thickness. Degreasing of surfaces was performed using acetone. The substrate was then grit blasted by Al_2O_3 in order to improve the roughness in the order of 10–12 µm. EN8 medium carbon steel was used as a counterface material. NiCrBSiCFe self fluxing alloy was used as the feedstock powder. The average size of the powder was 63.72 µm. The chemical compositions of the materials used are shown in Table 1.

Table 1. Chemical composition (wt. %) of substrate, spray powder and counterbody

Elements	**Ni**	**Cr**	**B**	**Si**	**C**	**Fe**	**S**	**Mn**	**Mo**	**P**
AISI 316 Substrate	14	18	--	1.0	0.08	Bal.	0.03	2.00	3.00	0.045
NiCrBSiCFe Powder	Bal.	13.3	3.1	3.9	0.5	3.7	--	--	--	--
EN-8 counterbody	--	--	--	0.15	0.35	Bal.	--	0.6	--	0.04

2.2. Plasma Spraying

Plasma spraying is a high-energy process in which a high current arc is generated within the torch and a gas is injected into the arc chamber, where it is heated and converted into high temperature plasma. The plasma spraying parameters (PSP-1 and PSP-2) used for coating on AISI 316 ASS are tabulated (Table 2). The stand-off distance, current and voltage parameters are varied to study the influence on coating characteristics. The NiCrBSiCFe alloy powder was fed on the 4 MP dual powder feed unit (SST-25). The Metco spray gun (SST-24) was stationary and the AISI 316 ASS specimen was mounted on a rotating table. The powder was introduced in the plasma jet generated from the plasma torch. The coating feedstock material was injected vertically into the plasma jet by argon (Ar) carrier gas for primary flow and hydrogen gas (H_2) for secondary flow. In the plasma jet, the temperature is around 6,600°C to 16,600°C which is responsible for melting. The particle flight in velocity up to 600 m/s is responsible for propelling towards the AISI 316 substrate [15]. The plasma coating was performed ~ 500 µm thickness.

Table 2. Plasma spraying parameters

Plasma spray parameter	PSP 1	PSP 2
Substrate	AISI 316 ASS	AISI 316 ASS
D.C. Current (A)	480	500
D.C. Volts (v)	70	60
Primary gas flow rate (slpm) Argon	150	150
Hydrogen	15	18
Feedstock carrier gas flow rate (slpm) Argon	37	37
Powder flow rate (g/min)	120	120
Stand-off spray distance (mm)	125	100
Scanning velocity (mm/sec)	6	6
Coating thickness (µm)	500	500

2.3. Wear Tests

Dry sliding tests were carried out using a DUCOM TR-20-M-106 pin-on-disc test rig. The test was performed as per ASTM standard G99-05 [16] with coating on the disc rather than on the pin material to simulate wear behaviour in specific application listed elsewhere [1]. The pins, with a diameter of 6 mm and a height of 31 mm, were machined from EN8 medium carbon steel as a counterface material. The NiCrBSiCFe coated AISI 316 ASS discs with two parameters were used as samples. The experiments were carried at loads of 20N and 40 N at different temperatures such as room temperature, 150°C, 250°C and 350°C. The sliding velocity was 1m/s and the sliding distance was 2000 m. The LVDT (linear variable differential transducer) was positioned on the weights to measure displacement and the load cell to sense the tangential force. An induction coil was inbuilt in the system to raise the temperature to the desired levels to carry out the experiment.

The wear and frictional force were simultaneously recorded by data acquisition system. The wear resistance was calculated by cumulative weight residual method. The mass loss of the uncoated and NiCrBSiCFe coated discs were measured after the completion of every cycle of experiment with an electronic weighing balance of 0.1 mg accuracy. The volume loss was calculated by the equation (1). The wear rate and wear resistance were calculated by equations 3 and 4, respectively. Coefficient of Friction (CoF) was calculated by the equation (5). The set of calculation is:

$$Volume\ \ loss\ \ (mm^3) = \left(\frac{Mass\ \ loss}{\rho}\right) \times 1000\ , \tag{1}$$

$$Coating\ \ density\ \ (\rho) = \rho_1 \times \left(\frac{m_a}{m_a - m_1}\right)\ , \tag{2}$$

where ρ_1 is the density of water 1 g/cm^3 at room temperature, m_a the weight of the plasma coating in air (g) and $m_1$is the weight of plasma coating in water (g),

$$Wear\ \ rate\ \ (mm^3/m) = \left(\frac{Volume\ \ loss}{Sliding\ \ dis\tan ce}\right)\ , \tag{3}$$

$$Wear\ \ resis\tan ce\ \ (m/mm^3) = \left(\frac{Sliding\ \ dis\tan ce}{Volume\ \ loss}\right)\ , \tag{4}$$

$$Coefficient\ \ of\ \ Friction,\ \ \mu = \left(\frac{F}{N}\right), \tag{5}$$

where F is the Frictional force and N is normal applied load in Newtons.

2.4. Coating Characterisation: *Microstructural and Microhardness Characterisation*

The plasma sprayed AISI 316 ASS samples were sectioned, polished and etched with Nital. The etched specimens were studied by optical microscopy (OM). The micrograph of EN-8 medium carbon steel was also analysed. The as-sprayed specimens of PSP-1 and PSP-2 were first cut suitably and analysed by SEM (HITACHI S 3000H). The worn tracks of the plasma sprayed specimens were also analysed using SEM to identify the mode of material loss during sliding at different temperatures. The worn debris of the NiCrBSiCFe coated discs at 350° were collected after the completion of the experiments. The morphology of the wear asperities collected were characterised by SEM. The microhardness of the plasma sprayed specimens was measured using Zwick MHT Vickers hardness tester at a load of 300 g for 20 seconds.

3. Results and Discussions

3.1. Microstructural Characterisation of the Coating

The largely employed Ni-based powder belongs to the NiBSi system with the addition of other alloying elements like C, Fe and Cr. The addition of chromium enhances the corrosion resistance at elevated temperatures and increases the hardness of the coating by the formation of hard phases. Boron decreases the melting temperature and contributes to the formation of hard phases. Silicon is added to increase the self-fluxing properties. Carbon produces hard carbides with elevated hardness, thus improving the wear resistance of the coatings. Solid solution of chrome in nickel with dispersed phases of borides, silicides and carbon borides forms a base of the NiCrBSiCFe layers.

The cross-sectional microstructures of PSP-1 and PSP-2 are shown on Figure 1(a) and (b). PSP-1 with a stand-off distance of 125 mm resulted in relatively fine lamellar microstructure with uniform molten splat formations and the even distribution of NiCrBSiCFe layers (Figure 1(a)). This microstructure resists loss of material in a better manner than PSP-2.

The unmelted spherical powder particles and pores were visible in PSP-2 sprayed relatively with a shorter stand-off distance of 100mm. This shorter stand-off distance prevents the powder from complete melting and the flight in velocity was relatively reduced. Formation of splats by the impact of spherical particles is visible in PSP-1 (Figure 1(b)). In PSP-2, small voids and unmelted particles are present which is unfavourable to the coating performance.

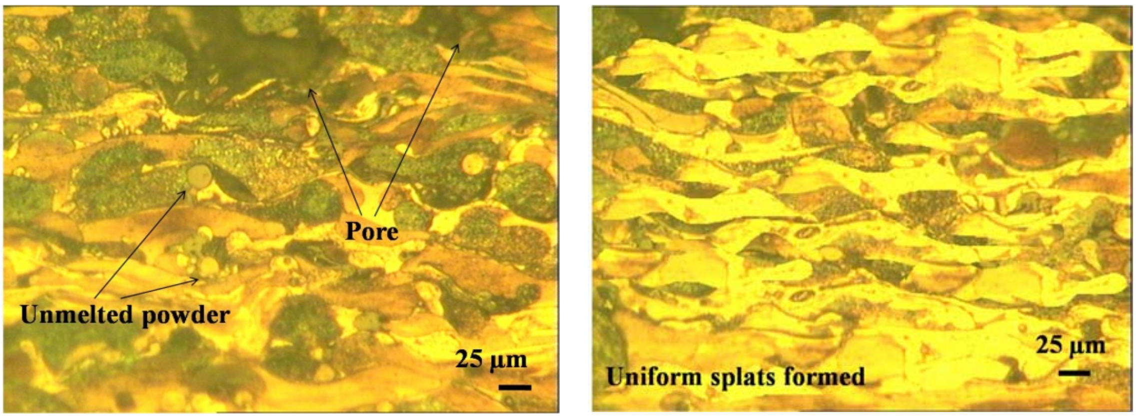

(a) (b)

Figure 1. Cross sectional microstructure of plasma sprayed coatings: (a) PSP-1; (b) PSP-2

3.2. Micro Hardness Characterisation

The initial hardness of the AISI 316 and EN 8 medium carbon steel pins was 223 $HV_{0.3}$ and 302$HV_{0.3}$, respectively. The obtained microhardness of the PSP-1 and PSP-2 are shown on Figure 2. With the increase in the stand-off distance, the microhardness also increases. The microhardness of PSP-2 with a shorter stand-off distance of 100mm was relatively lower at 780 $HV_{0.3}$ whereas the microhardness of PSP-1 with 25 mm more stand-off distance than PSP-2 was relatively higher at 823 $HV_{0.3}$. The microhardness values are also in direct correlation with the coating microstructure. A relatively higher value of the microhardness is a representative phenomenon of presence of adequate lamellar structure with high cohesion strength between the layers and high adhesion strength on the coating/substrate interface. The spray distance of 125 mm was sufficient enough to enable adequate melting and flow of the powder and higher microhardness [17].

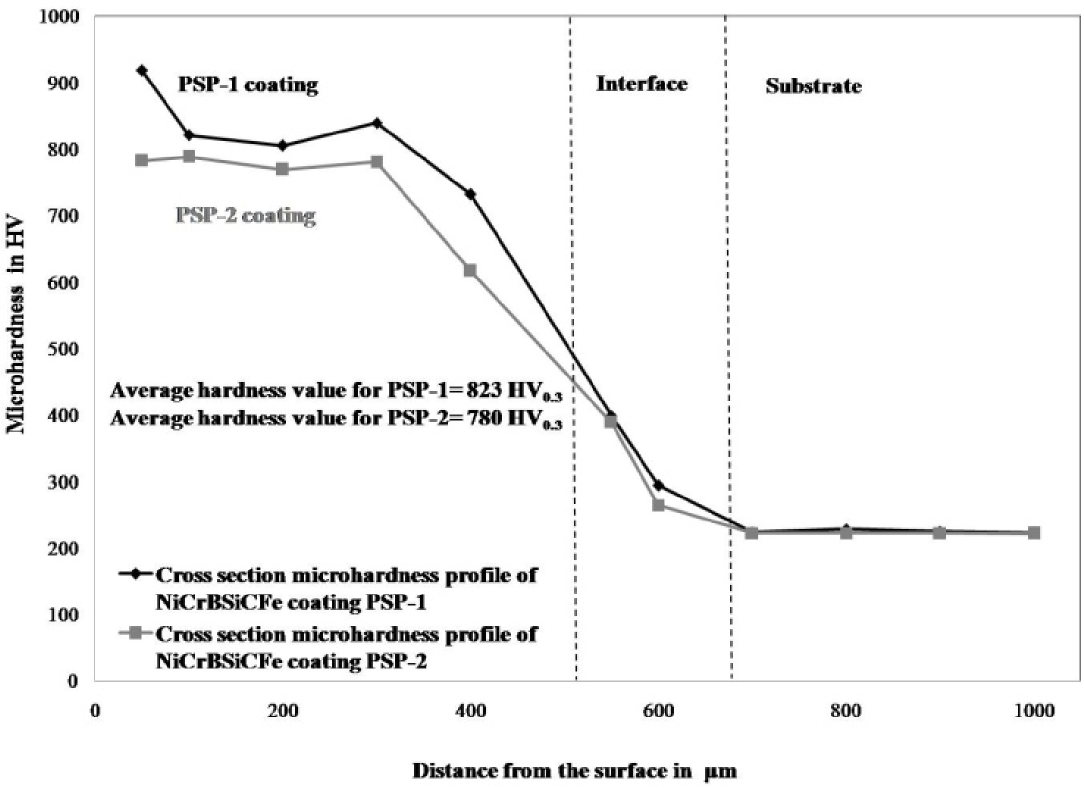

Figure 2. Microhardness variation of PSP-1 and PSP-2 as a function of the distance from the surface

3.3. Characterisation of Wear at Different Temperatures

The wear of the uncoated, PSP-1 and PSP-2 samples at room temperature with 20 N load at sliding velocity 1m/s is shown on Figure 3(a). It is observed that the plasma sprayed samples possess good wear resistance when compared with the uncoated samples. The uncoated samples worn at sliding velocity of 1m/s showed greater wear of 1000 µm. The superior wear resistance of NiCrBSiCFe coated samples was due to the presence of hard intermetallics like Ni_3B and Fe_3B formed during spraying. Compared to PSP-2, PSP-1exhibits higher wear resistance. This may be attributed to the higher hardness of PSP-1 samples. The wear rate of the uncoated, PSP-1 and PSP-2 samples was slightly higher at 150°C than at room temperature for all tested samples which is shown on Figure 3 (b). At 250°C, the wear rate observed to be higher compared to the other test conditions (Figure 4 (a)). At 1 m/s sliding velocity, material softening might have taken place which promotes three body abrasive wear with seizure. Sliding at this temperature might have led to high local pressure between contacting asperities resulting in plastic deformation, adhesion and the consequent formation of local junctions.

The more plastic deformation associated with the wear is responsible for the higher wear rate in this temperature. The worn debris during sliding at 350°C turn in to oxides which further behaves like a protective and lubricative film eliminating the chances of severe material loss. The improved wear resistance of both PSP-1 and PSP-2 samples are justified by the oxide formations and is shown on Figure 4(b). The samples worn at sliding velocity 2m/s at room temperature, 150°C, 250°C and 350°C showed relatively lesser wear with respect to time (Figure 5(a) and (b)) and (Figure 6(a) and (b)). The reason for the comparatively lesser wear is due to the slipping that occurs at higher velocity (2m/s). Slipping excludes the chances of severe wear and improves the wear resistance.

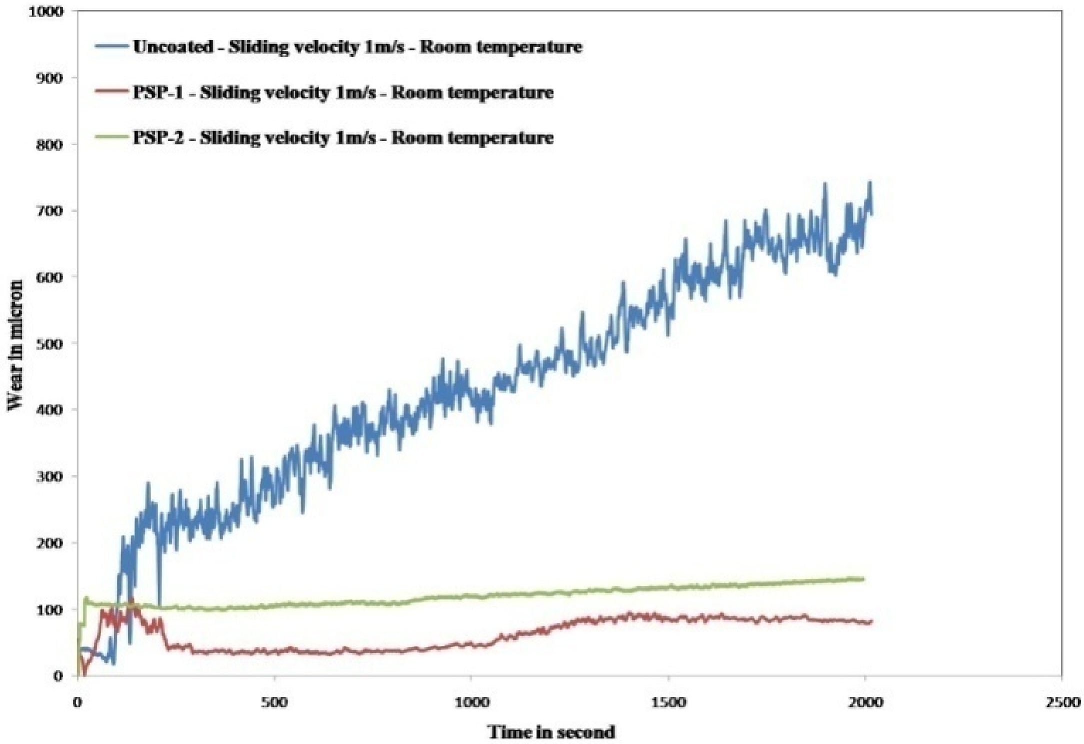

(a)

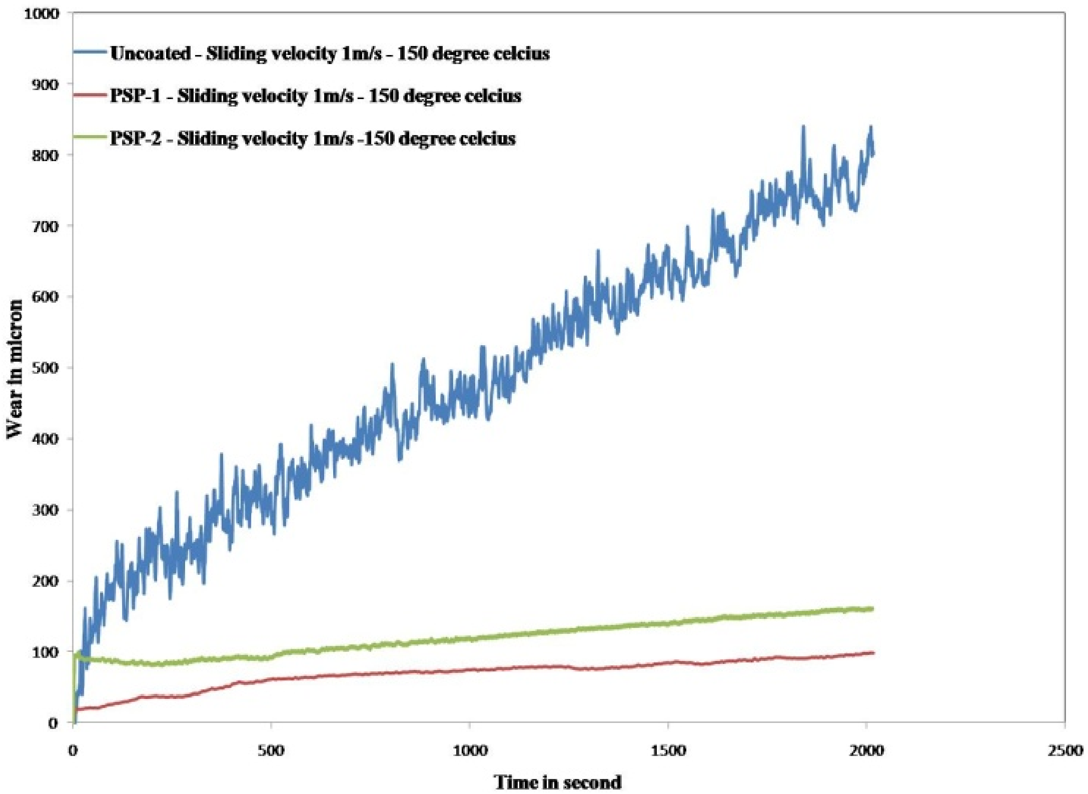

(b)

Figure 3. Variation of wear with respect to time at sliding velocity 1m/s: (a) room temperature; (b) 150°C

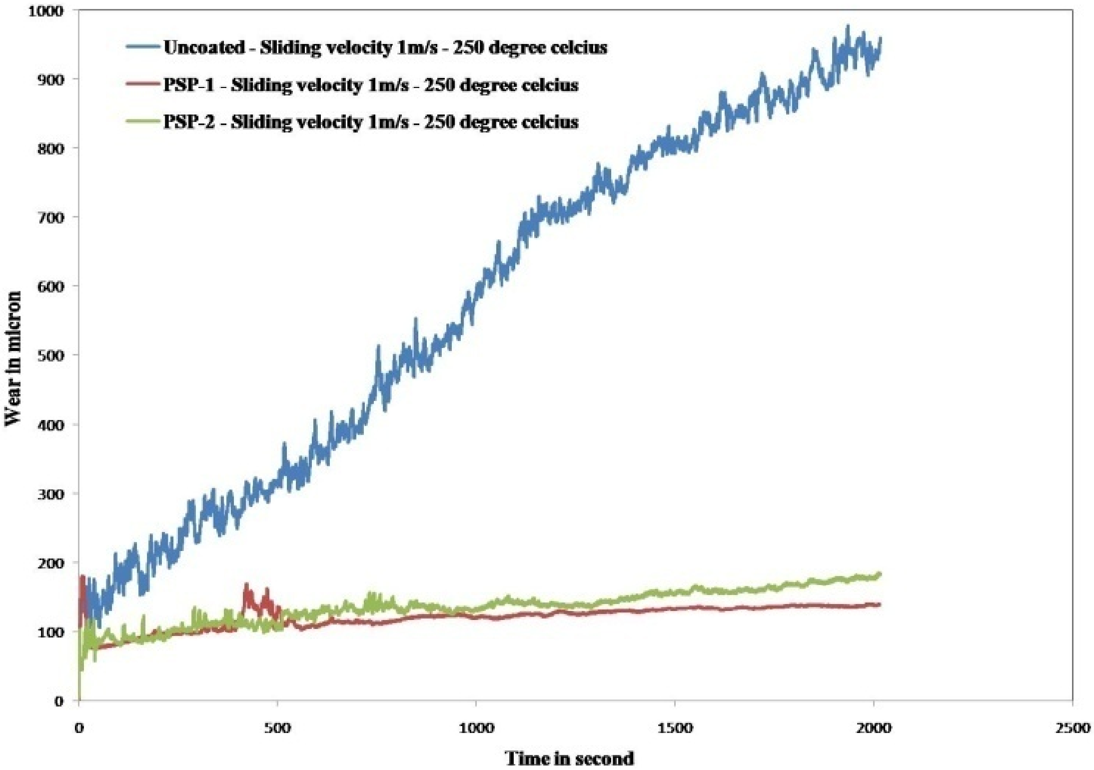

(a)

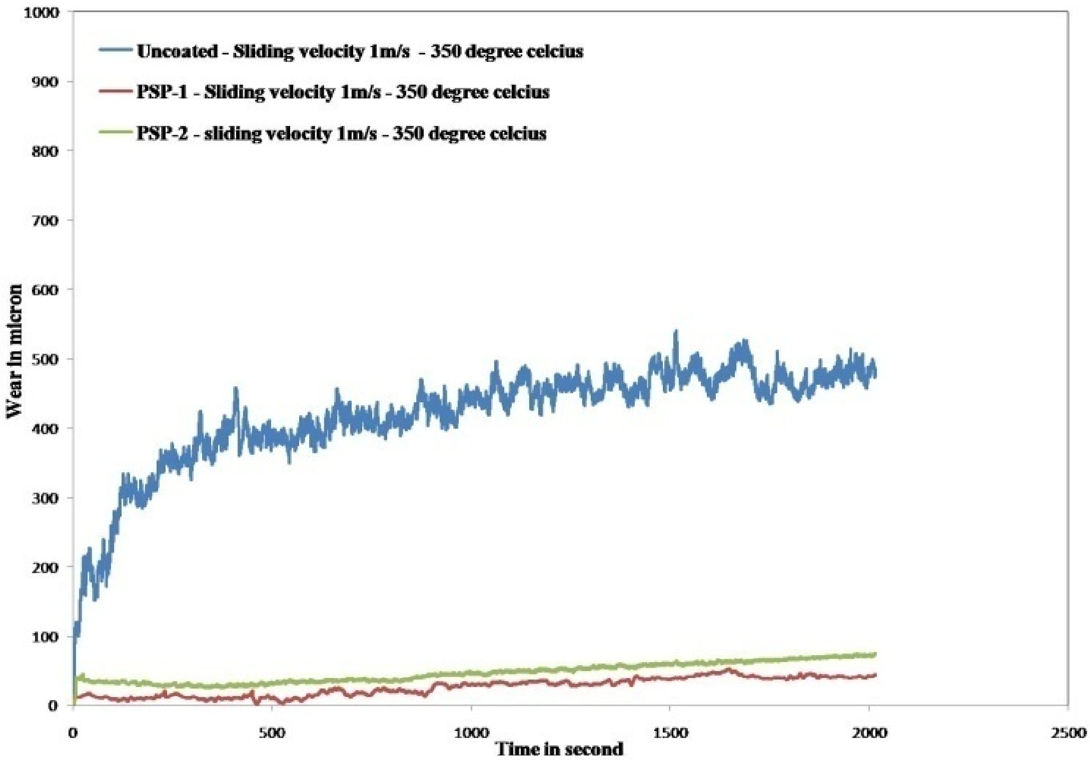

(b)

Figure 4. Variation of wear with respect to time at sliding velocity 1m/s: (a) 250°C; (b) 350°C

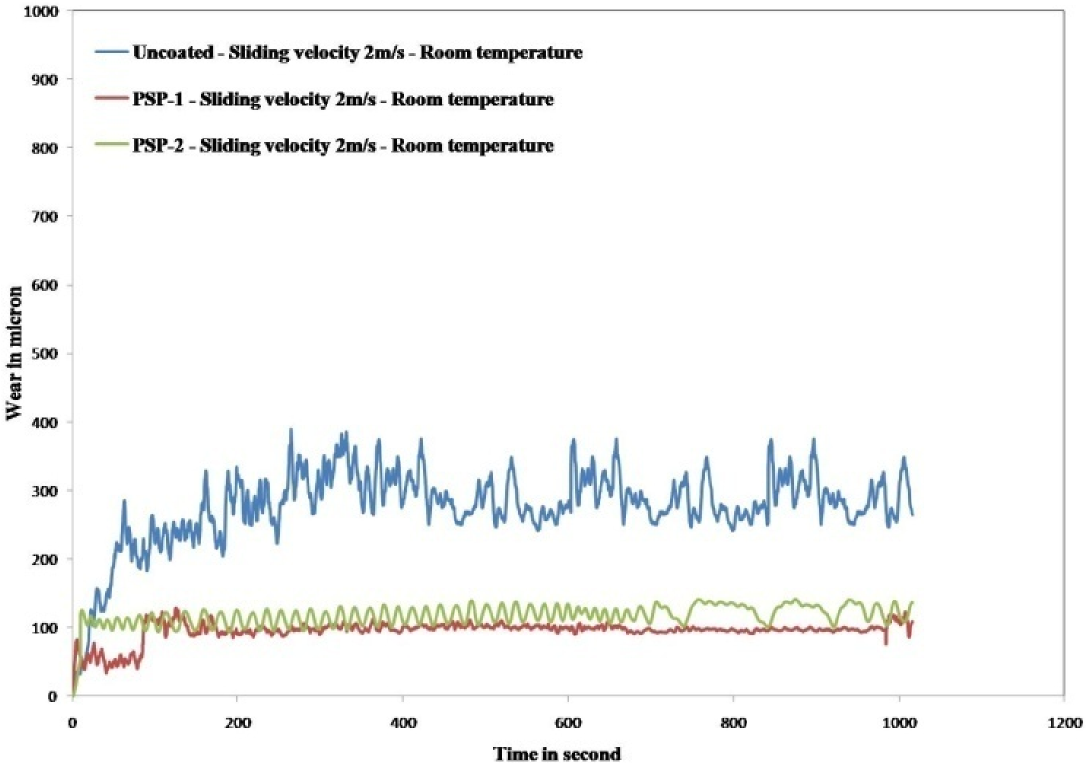

(a)

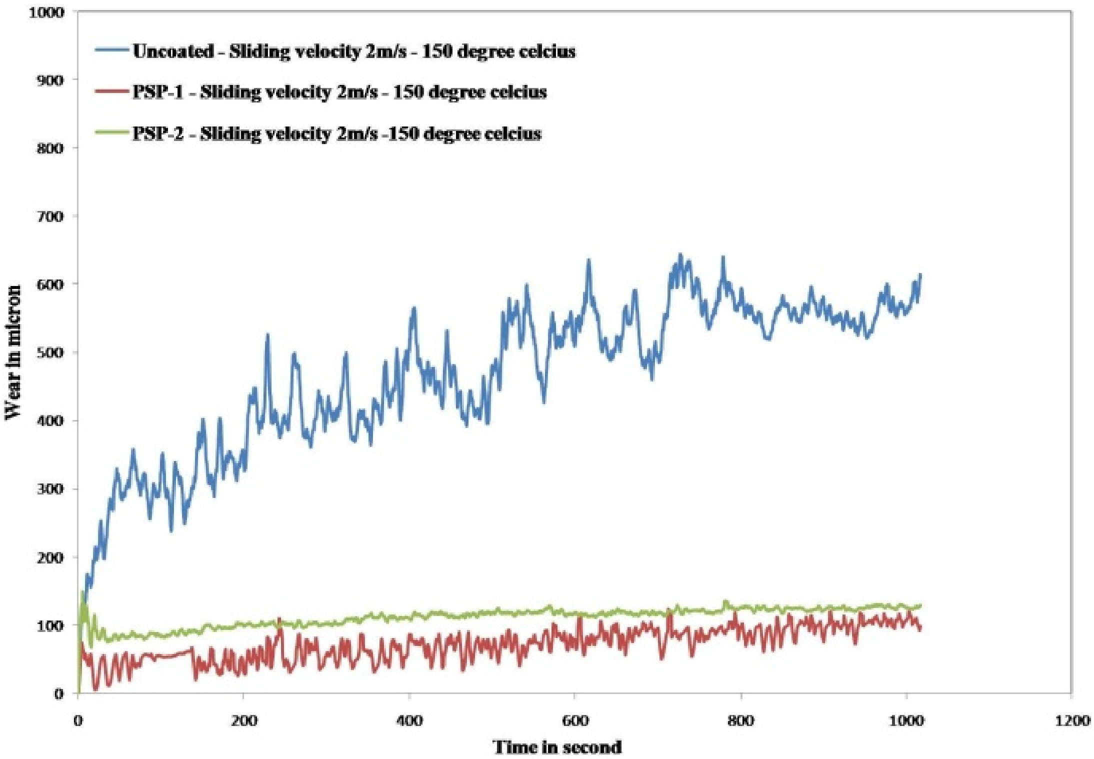

(b)

Figure 5. Variation of wear with respect to time at sliding velocity 2m/s: (a) room temperature; (b) 150°C

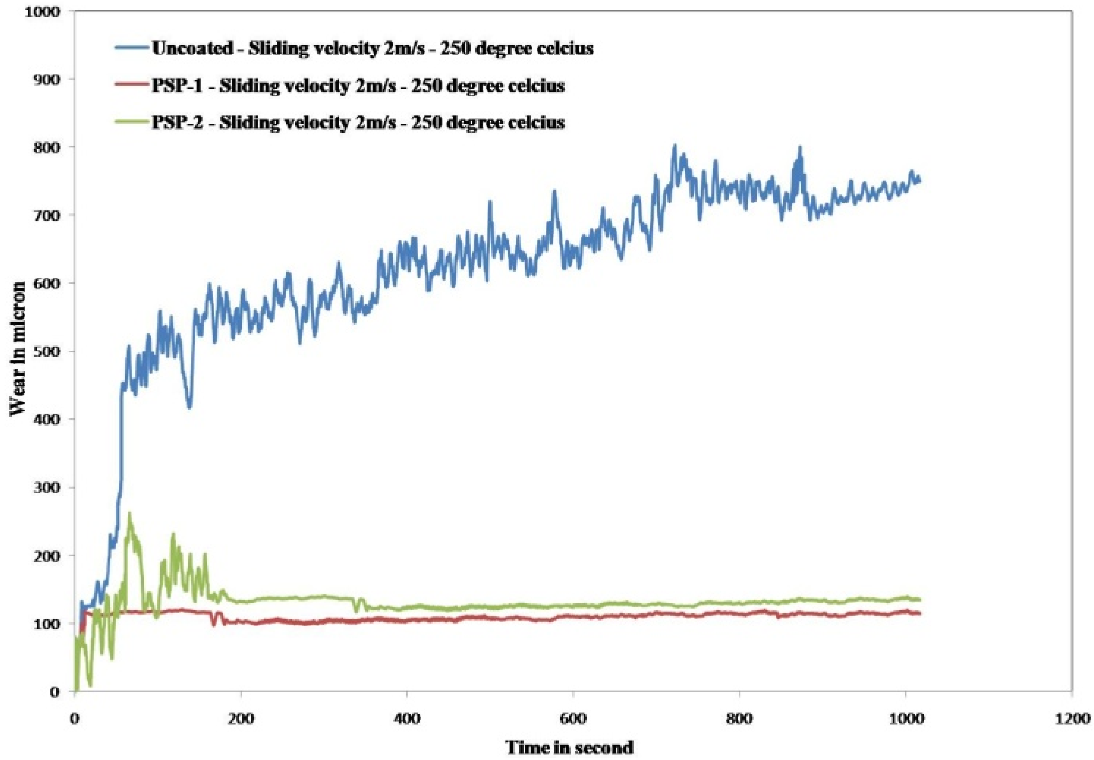

(a)

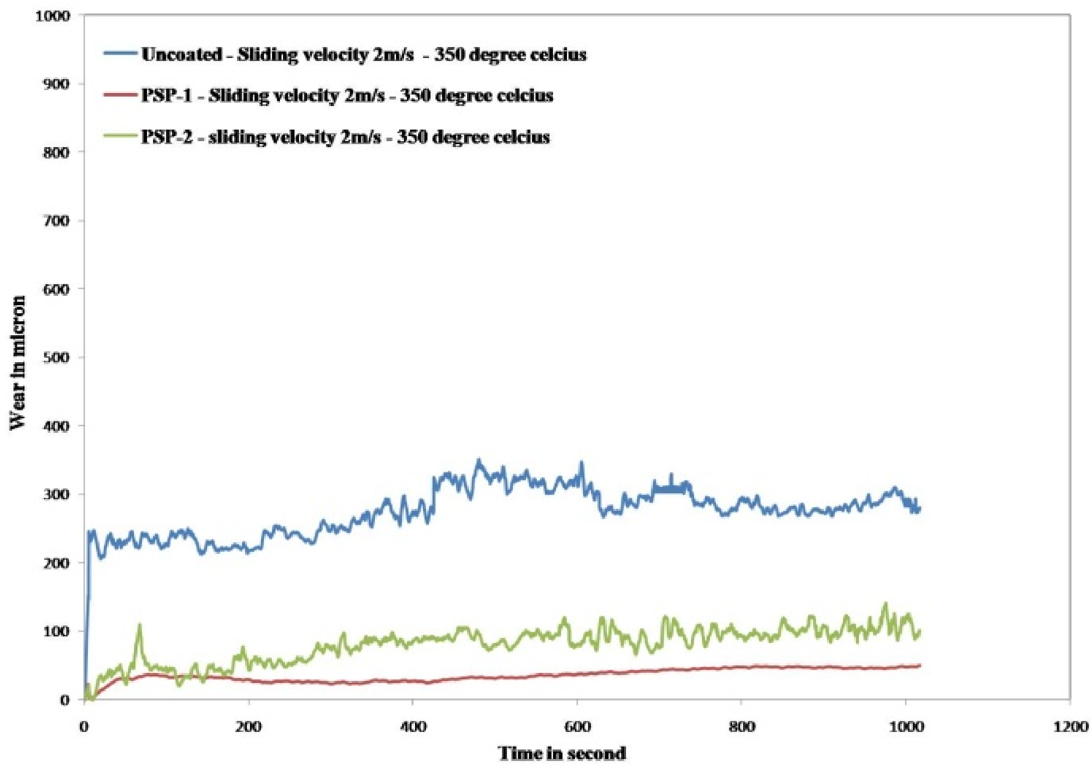

(b)

Figure 6. Variation of wear with respect to time at sliding velocity 2m/s: (a) 250°C; (b) 350°C

The wear resistances were calculated at sliding velocities at 1 m/s and 2 m/s for different temperatures with an applied load of 20 N are shown on Figure 7 (a) and (b). The higher wear resistance values were obtained for samples worn at 350°C in both the spraying parameters. When the plasma sprayed parameters are compared, the average wear resistance of PSP-1 samples are marginally higher (501 m/mm^3) than PSP-2 (456 m/mm^3) at 1m/s sliding velocity. Similarly, the average wear resistance of PSP-1 samples are marginally higher (575 m/mm^3) than PSP-2 (481 m/mm^3) at 2m/s sliding velocity. At sliding velocity 2m/s the wear resistances of samples were found to be greater than the samples worn at 1 m/s sliding velocity.

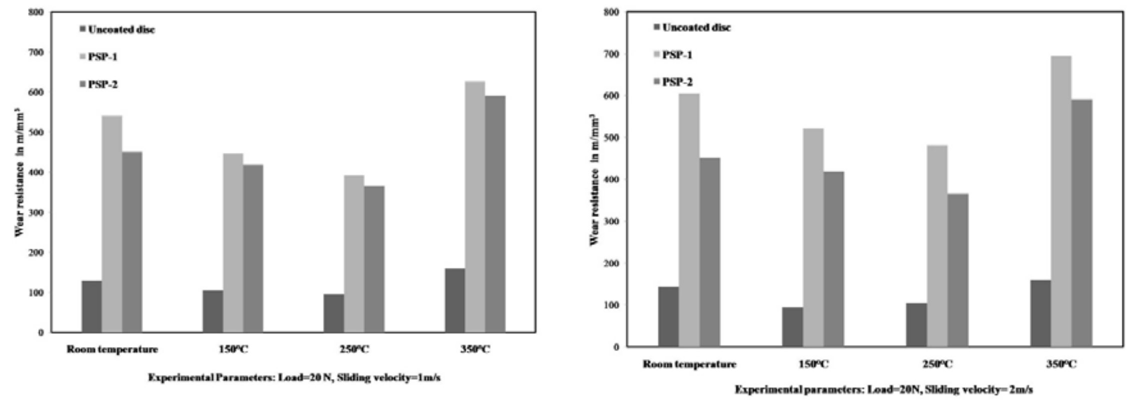

(a) (b)

Figure 7. Wear resistance of uncoated, PSP-1 and PSP-2 samples: (a) sliding velocity 1m/s; (b) sliding velocity 2m/s

3.4. Worn Surface Characterisation by SEM

Figure 8(a)-(b) shows the wear tracks of sample worn with 20 N load and at different temperatures at sliding velocity 1m/s and 2m/s of PSP-1 samples. Coated samples sled with 1m/s velocity in room temperature, the worn surface of the sample is characterised by delamination of layers. Debris is sparsely seen on Figure 8(a). In contrast samples worn at 2m/s sliding velocity show shallow grooves parallel to the sliding direction. The sliding resulted with minimal amount of plastic deformation due to slipping (Figure 8(b)). At 150°C, samples worn at sliding velocity of 1m/s the surface is characterised by flaking and exfoliation.

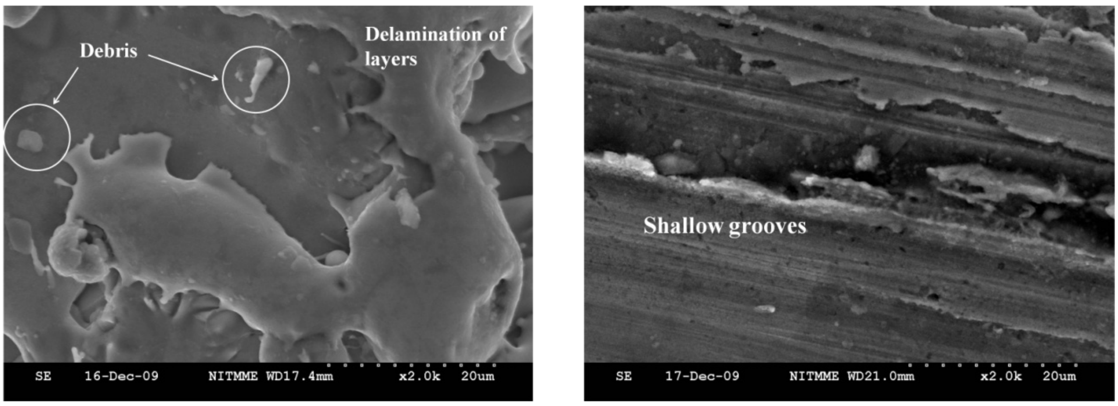

(a) (b)

Figure 8. Worn surface of sample at room temperature: (a) sliding velocity 1m/s; (b) sliding velocity 2m/s

Further subsurface cracking is visible due to the adhesive wear at lower sliding velocity and is shown on Figure 9(a). The samples worn at sliding velocity 2m/s showed shallow prow formation, which run parallel to the sliding direction (Figure 9(b)).

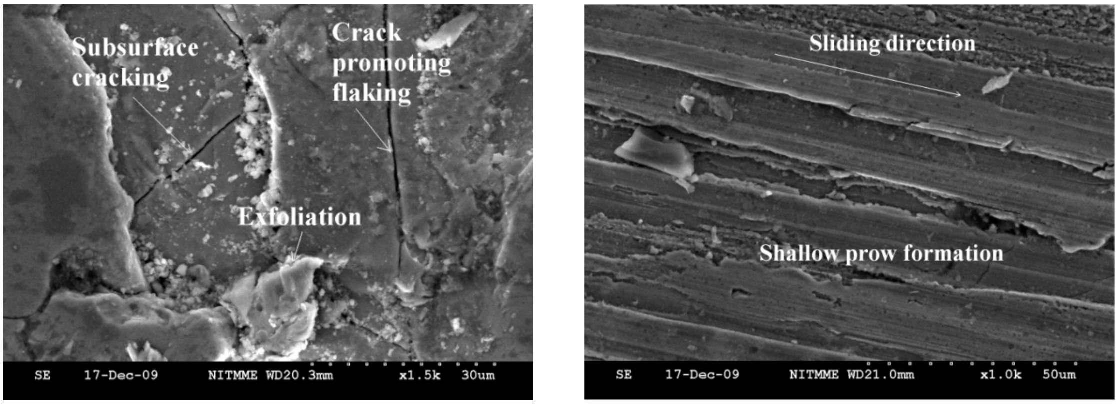

(a) (b)

Figure 9. Worn surface of sample at 150°C: (a) sliding velocity 1m/s; (b) sliding velocity 2m/s

This mode of wear promotes minimal material loss. At 250°C, samples worn at 1m/s sliding velocity, the surface is characterised by ploughing and prow formations. Both these modes promote more material loss which is shown on Figure 10(a). The samples worn at sliding velocity of 2m/s shows ploughings with lesser depth and featureless plateaus conclude that lesser wear has taken place (Figure 10(b)).

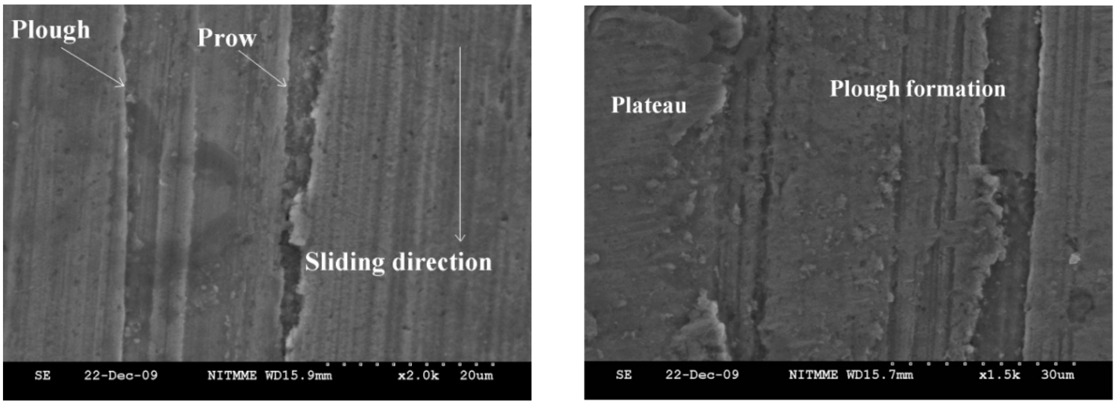

(a) (b)

Figure 10. Worn surface of sample at 250°C: (a) sliding velocity 1m/s; (b) sliding velocity 2m/s

The worn surface of the samples sled with 1m/s at 350°C shows oxide layer formation with microcracks as it is shown on Figure 11(a). The oxides formed were peeled off from the surface and promotes further wear. These oxides promote cracking. The cracks encourage more material loss at lower velocity. The samples worn at 2m/s sliding velocity showed the presence of oxide layer formation. The oxide layers are stable with no visible microcracks (Figure 11(b)).

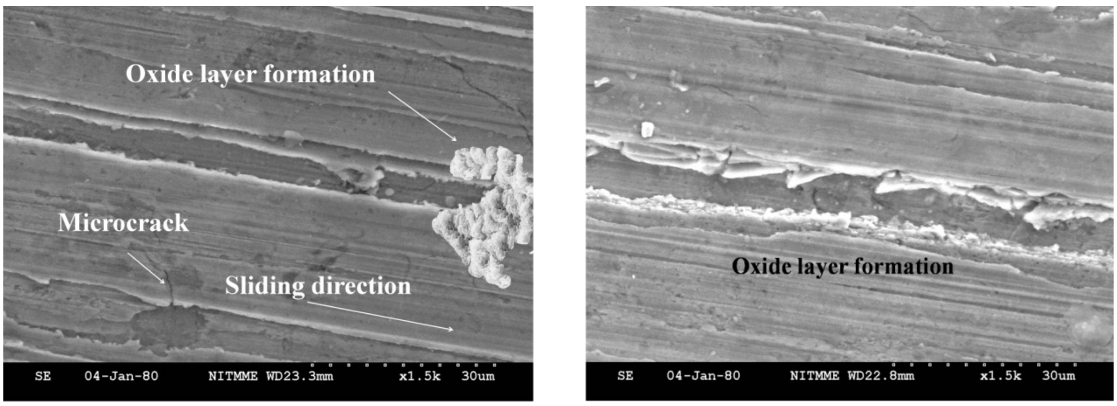

(a) (b)

Figure 11. Worn surface of sample at 250°C: (a) sliding velocity 1m/s; (b) sliding velocity 2m/s

Lateral spreading of the material on consecutive runs turn in to oxide layers which act as a protective and lubricative layer thereby preventing more material loss.

Conclusions

From the high temperature dry sliding wear experiments conducted on uncoated and AISI 316 ASS substrates plasma sprayed under PSP-1 and PSP-2 parameters at various operating temperatures, the following conclusions can be drawn.

- The NiCrBSiCFe was plasma sprayed in two parameters (PSP-1and PSP-2) on AISI 316 ASS to a thickness of up to 500 μm. The coatings exhibited metallurgically good bond strength to the substrate and free from any defects.
- PSP-1 with a stand-off distance of 125 mm showed fine lamellar microstructure with evenly dispersed phases of NiCrBSiCFe on the coating and PSP-2 shows sparse presence of unmelted powders included with pores at the interface.
- The microhardness of PSP-1 and PSP-2 was improved to 823 $HV_{0.3}$ and 780 $HV_{0.3}$, respectively. This improvement in hardness primarily responsible for higher wear resistance of the coated samples.
- The average wear resistance value of PSP-1 at sliding velocity 1 and 2 m/s are 501 and 575 m/mm^3, respectively. The average wear resistance value of PSP-2 at sliding velocity 1 and 2 m/s are 456 and 481 m/mm^3, respectively.
- The effect of sliding velocity is very significant at different operating temperatures. Wear rate was found to be inversely proportional with the sliding velocity as it shows increased wear resistance at 2m/s when compared to 1m/s, irrespective of the spraying parameters.
- At 250°C, material softening might promote three body abrasive wear and subsequently lead to severe adhesive wear upon further sliding with no visible oxide layers in 1m/s sliding velocity.
- The samples worn at 2m/s sliding velocity showed shallow grooves, ploughing and prow formations due to the slipping. This may be attributed to the reason for superior wear resistance when compared with lower sliding velocity (1m/s).
- The samples worn at 1m/s sliding velocity showed exfoliation mode of wear mechanism with deeper prow formation as a result of abrasive wear is responsible for the higher wear rate and poor wear resistance.
- The oxide layers formed at 350°C on consecutive sliding, acted as a protective and lubricative layer more prominently at 2m/s sliding velocity rather than at 1m/s sliding velocity.

References

1. Chivers, T. C. Tribological design and assessment-the nuclear industry, *Tribology Series,* Vol. 14, 1989, pp. 383–388.
2. Hutchings, I. M. *Tribology: Friction and Wear of Engineering Materials.* UK: Edward Arnold, 1992.
3. Otsubo, F., Kishitake, K., Akiyama, T., Terasaki, T. Characterization of blasted austenitic stainless steel and its corrosion resistance, *Journal of Thermal Spray Technology,* Vol. 12, No 4, 2003, pp. 555–559.
4. Rodriguez, J., Martin, A., Fernandez, R., Fernandez, J. E. An experimental study of the wear performance of NiCrBSi thermal spray coatings, *Wear,* Vol. 255, 2003, pp. 950–955.
5. Roumiana S. Petrova, Naruemon Suwattananont. Surface Modification of Ferrous Alloys with Boron, *Journal of Electronic Materials,* Vol. 34 (5), 2005, pp. 575–582.
6. Umanskii, A. P., Konoval, V. P., Panasyuk, A. D., Podchernyaeva, I, A., Malyshkin, V. V., Kralya, V. A., *Powder Metallurgy and Metal Ceramics,* Vol. 46, Nos. 3–4, 2007, pp. 133–138.
7. Farias, M. C. M., Souza, R. M., Sinatora, A., Tanaka, D. K. The influence of applied load, sliding velocity and martensitic transformation on the unlubricated sliding wear of austenitic stainless steels, *Wear,* Vol. 263, 2007, pp. 773–781.
8. Harsha, S., Dwivedi, D. K., Agarwal, A., Performance of flame sprayed Ni-WC coating under abrasive wear conditions, *Journal Materials Engineering and Performance,* Vol. 17, 2008, pp. 104–110.

9. Harsha, S., Dwivedi, D. K., Agarwal, A. *International Journal of Advanced Manufacturing Technology*, 2008, Vol. 38, pp. 93–101.
10. Hashemi, S. M., Enayati, M. H., Fathi, M. H. Plasma Spray Coatings of Ni-Al-SiC Composite, *Journal of Thermal Spray Technology*, Vol. 18(2) , 2009, pp. 284–291.
11. Bolelli, G., Gualtieri, E., Lusvarghi, L., Pighetti Mantini, F., Pitacco, F., Valeri, S., Volz, H. Microstructural and tribological comparison of HVOF-sprayed and post-treated M–Mo–Cr–Si (M = Co, Ni) alloy coatings, *Journal of Thermal Spray Technology,* Vol. 18(2), 2009, pp. 231–242.
12. Nascimento, F. C., Lepienski, C. M., Foerster, C. E., Assmann, A., da Silva, S. L. R., Siqueira, C. J de M., Chinelatto, A. L., *Journal of Material Science,* Vol. 44, 2009, pp. 1045–1053.
13. Serres, N., Hlawka, F., Costil, S., Langlade, C., Machi, F., Cornet, A., Dry coatings and ecodesign, part. 2: tribological performances, *Surface and Coating Technology*, Vol. 204, 2009, pp. 187–196.
14. Liu, Sh., Zheng, X., Geng, G. Dry sliding wear behaviour and corrosion resistance of NiCrBSi coating deposited by activated combustion-high velocity air fuel spray process, *Materials and Design*, Vol. 31, 2010, pp. 913–917.
15. Tucker, R. *Surface Engineering ASM: Handbook, 5* (ASM International) 1994, p. 497.
16. ASTM G99-95, ASTM G99-95a (re-approved 2000): *Standard test method for wear testing with a pin on disk apparatus*. 1995.
17. Mrdak, M., Vencl, A., Ćosić, M. Microstructure and mechanical properties of the Mo-NiCrBSi coating deposited by atmospheric plasma spraying, *FME Transactions*, Vol. 37, 2009, pp. 27–32.

Received on the 21st of April, 2010

Computer Modelling and New Technologies, 2010, Vol.14, No.3, 30–40
Transport and Telecommunication Institute, Lomonosova 1, LV-1019, Riga, Latvia

INFLUENCE OF TEMPERATURE ON THE WEAR BEHAVIOUR OF WC-CO PLASMA SPRAYED AISI 304 AUSTENITIC STAINLESS STEEL

***G. M. Balamurugan*[1], *M. Duraiselvam*[2*]**

[1]Department of Mechanical Engineering
Jayaram College of Engineering and Technology, Pagalavady
Tiruchirappalli–620 104, Tamil Nadu, India

[2] Department of Production Engineering, National Institute of Technology
Tiruchirappalli– 620 015, Tamil Nadu, India
[*]Corresponding author, Phone: +91 431 2503509. Fax: +91 431 2500133
E-mail: durai@nitt.edu

The study presented in this paper concerns the influence of the temperature on the wear behaviour of plasma sprayed WC-Co coated AISI 304 austenitic stainless steel (ASS) substrate. With higher hardness and the good adhesion with the substrate, the sprayed coating exhibits a better wear resistance. The deposit was characterized by hardness measurements, micro structural examination, coating density and sliding wear assessment.

Wear experiments were carried out by dry sliding contact of EN-24 medium carbon steel pin as counterpart in a pin-on-disc machine at various condition like room temperature, 100°C, 200°C, 300°C under the load of 30N at 2m/s sliding velocity. The wear rate was dependent on the interaction between applied load and tangential velocity. Compared to the uncoated substrate, the WC-Co coated specimens exhibited improved wear resistance up to 5 times. The study revealed significant weight loss at room temperature and abrupt decrease at high temperatures. From X-ray diffraction analysis (XRD), the wear behaviour at high temperature has been attributed to the formation of a protective oxide layer at the surface during sliding. The worn surfaces, plastic deformation and wear debris were analysed through scanning electron microscopy (SEM) and XRD.

Keywords*:* sliding wear, austenitic stainless steel, WC-Co, plasma spraying

1. Introduction

Austenitic stainless steels have excellent corrosion resistance and mechanical properties in many environments and have been extensively used in nuclear reactors, biomedical implants as well as in components for chemical and food industries. However, they exhibit a relatively low hardness and poor tribological properties. When in contact with themselves or other materials, austenitic stainless steels frequently suffer from severe metallic wear, due to the formation of strong adhesion junctions between the contact surfaces and severe surface /subsurface plastic deformation [1]. Among austenitic stainless steels, AISI 304 stainless steels have shown the lowest wear resistance both in dry sliding and under lubricated conditions have severe adhesive and abrasive wear have been observed with significant mass losses [2]. The plasma-spraying process presents a widely employed method of applying surface coatings, due to the easiness, process speed and possibility to use in a wide range of coating materials on metallic, ceramic, or even polymeric substrates [3]. Their adherence on the surface is determined by the process parameters such as temperature, inflow velocity and nature of the coated material. The porosity of the plasma-sprayed coatings is understood as a sum of porosity originated from the entrapped gas, interstitial and solidification porosities [4]. The morphologies of the wear scars developed above the transition temperature are characterized by the formation of very smooth ‘glaze’ layers which is considered to be the main reason for the decreased wear rate and friction [5]. At lower sliding velocities, oxidation effects are absent and the sliding wear process is plasticity-dominated. Stott and co-workers demonstrated the influence of oxide debris in reducing wear, particularly at higher temperatures [6]. In certain conditions, the metallic debris can oxidize and the fragments can agglomerate to form protective scales [7]. This plasma process is seen as a technically and economically viable alternative to the commercial Kolsterising process which is currently being used for surface treatment of stainless steel components [8]. The resultant precipitation-free layer has a high hardness and excellent corrosion resistance. Thermal sprayed tungsten carbide-based cermet coatings have been widely used in various wear applications for its high toughness, high hardness and good bonding strength [9–12]. High porosity in the coating and the decarburization phenomenon of WC is occurring during the spraying limit of the technology application. A primary factor controlling the hardness in a thermal spray coating is porosity which is minimized by achieving dense splat microstructure with low porosity, which in turn requires that the particles reach sufficiently high temperatures to experience partial melting. Excessive temperatures of the particle experienced with combustion and air plasma spray processes tend to result in extensive decarburization of WC into brittle phases such as W_2C and $Co_x W_y C_z$ compounds, which has detrimental effects on the wear and corrosion of coatings and bulk parts [13]. The microstructure and tribological behaviour of WC-CoCr and WC-Co coatings deposited by HVOF and LENS processes have been studied. The wear performance of these coatings is also compared with the WC-Co bulk material produced by SPS technique [14]. The thermal spray process, such as high velocity oxygen fuel (HVOF), is probably the most frequently applied coating process for producing WC-Co coatings. WC-Co powders tend to undergo decarburization and reaction between the WC, Co and O_2 during spraying resulting in the formation of brittle phases such as W_2C, W, WO_3, η-phases, etc. [15]. Deposition of pure metals, alloys and composites by the cold spray process is reported numerously. However, reports of cermet such as WC-Co [16, 17] and ceramic depositions by the cold spray process are limited due to the lack of ductile phase. WC-Co cermet has wide applications in machinery industries as a wear-resistance coating due to its high hardness and toughness. Zhu et al. [18] prepared nanostructures and conventional WC-12%Co coatings using vacuum plasma spraying and investigated the tribological properties of the coatings. The existing studies were not characterized the worn track and sliding wear operating condition. The present work was planned with the aim of studying the wear resistance properties of WC-Co coatings obtained by means of thermal plasma spraying technique on ASS 304 steel substrate at different temperature such as room temperature,100 °C, 200 °C, 300 °C. The coatings were tested using pin-on-disc tribometer in dry sliding conditions with hardened and stress relieved EN 24 steel pin as counterpart. In the present study, the friction and wear behaviour of the plasma sprayed WC-12%Co coatings on disc which is rotated under the sliding pin at normal and elevated temperatures were investigated.

2. Experimental Procedure

2.1. Materials

Materials used are commercially available pure Micro-melt® 88WC-12Co powder with a mesh size of – 325 supplied by Carpenter Powder Products Inc., USA. The particle size of the powder material ranges from 38–50 µm. The morphology of WC-Co particle was analysed by SEM. The discs were cut from AISI 304 ASS stainless steel plate to a size of 100mm diameter and 4mm thickness by electro-discharge machining. The counter face material EN24 medium carbon steel was prepared as pin with a size of 6mm diameter and 30 mm height. The chemical composition of powder, substrate and counterbody is shown in Table 1.

2.2. Plasma Spraying Process

The discs were grit blasted to a R_a value of 10 µm in order to improve the adherence. The spraying was conducted in open atmosphere by means of the plasma spray gun (sulzer Metco SsT-24) which was stationery and the specimen was mounted on a rotating table. The plasma gas was Ar+ 7 vol. % H_2. The coating feedstock material was injected vertically in to the plasma jet by argon (Ar) carrier gas for primary flow and hydrogen (H_2) for secondary flow. The plasma spraying was performed with a parameter combination shown in Table 2. The coating thickness of the sprayed specimens was controlled to 500 µm.

Table 1. The chemical composition (wt. %) of substrate, WC-Co powder and the counterbody

Element	AISI 304 Substrate	WC-Co Powder	EN 24 Counterbody
C	< 0.08		< 0.45
Cr	17.5–20	5.48	0.90–1.40
Mn	< 2		<0.70
Co		11.3	
Ni	8–11		1.3–1.8
Fe	Bal.	< 0.02	Bal.
W		Bal.	
S	< 0.03		
P	< 0.045		
Si	< 1		< 0.35
Mo			0.20–0.35

Table 2. Thermal spraying process parameters

Parameter		Value
Substrate		AISI 304 ASS
D.C. Current (A)		500
D.C. Volts (V)		70
Primary gas flow rate (SLPM)	Argon	110
Primary gas flow rate (SLPM)	Hydrogen	18
Feed stock carrier gas flow rate (SLPM)	Argon	37
Powder flow rate (g/min)		60
Standoff spray distance (mm)		75
Scanning velocity (mm/sec)		6
Coating thickness (μm)		500

2.3. Tribology Test

A high-temperature pin-on-disk tribometer is used for evaluating the dry sliding wear resistance at different temperatures. The load cell to sense the tangential force and the linear variable differential transducer (LVDT) probe in the tribometer was positioned on the weights to measure the displacement. Plasma sprayed steel disc was kept on the specimen which was slightly deviated from ASTM G99-05 standard [19]. The load used in this experiment was 30 N and the sliding velocity was kept constant at 2 m/s. The wear tests were performed at sliding distance of 2000 m. The specimens were tested at three different temperatures viz., room temperature, 100°C, 200°C and 300°C. The plasma coated samples were flattened by surface grinding to attain surface roughness value $R_a \sim 1$ μm. Wear resistance was determined by measuring the weight loss of the specimen after each test. All tests were repeated once to ensure reasonable reproducibility. Before and after each experiment, the specimen was ultrasonic cleaned and dried and the weight loss was measured using an electronic analytical balance to an accuracy of 0.1 mg. The depth of wear and the frictional force were recorded with respect to time.

Volume loss was calculated using the mass loss data as shown in Eq. (1), wear rate and wear resistance was calculated using Eqs. (2) and (3), CoF was computed from the acquired frictional force using Eq. (4):

$$Volume\ loss(mm^3) = \left(\frac{Mass\ loss}{\rho}\right) \times 100\ , \tag{1}$$

$$Wear\ rate(mm^3/m) = \left(\frac{Volume\ loss}{Sliding\ distance}\right)\ , \tag{2}$$

$$Wear\ resistance(m/mm^3) = \left(\frac{Sliding\ distance}{Volume\ loss}\right), \tag{3}$$

$$Coefficient\ of\ \ friction, \mu = \frac{F}{N}\ , \tag{4}$$

where F is the frictional force in Newton and N is the normal applied load in Newton

$$Coating\ density\ (\rho) = \rho_1\left(\frac{m_2}{m_2 - m_1}\right). \tag{5}$$

2.4. Material Characterization

The following tests were used to characterize the materials.

2.4.1. Structural, hardness, density and X-ray diffraction characterization

Cross sectional microstructure of samples was analysed using SEM. The cut specimens were polished and buffed with alumina slurry solution (1, 0.3 and 0.05 µm) to get mirror finished surface and finally etched with Nital solution. Along with this, micrograph of EN24 pin was also analysed. For wear mechanisms and material loss determination, the worn tracks were analysed by SEM. Morphology of the uncoated specimen and WC-Co coated disc worn debris were characterized by SEM (HITACHI S 3000H). Small pieces from as-sprayed coatings were cut for phase identification by XRD. The phase composition of the coatings and the powder was determined by XRD (D/MAX ULTIMA III, Rigaku Corporation, Japan) using filtered CuKα radiation (λ = 0.15418 nm) operated at 30 mA and 40 mA. The used exposure time was 20 min and the analysed spectra taken for a speed of 2°/min with a scanning range 20°–80°. The micro hardness measurements were conducted using Zwick MHT on the sections of the coatings using the Vickers Micro indentor with the loads of 300g applied for 20 seconds. To determine the actual density of WC-Co, the coating was peeled off from the substrate and the actual density was determined using Archimedes principle as per the equation 5. Average actual density of the coating was 14.82 g/cm^3。 Theoretical density of the WC-Co plasma sprayed coating was found out by using the molecular formula 14.86 g/cm^3。

3. Results and Discussions

3.1. Powder Characterisation

Initially the powders which are mainly composed of WC phase and no phase was found related to W_2C. During plasma spraying, WC decomposes to W_2C due to higher intensity of power. This may be attributed to the improved hardness. Appearing of W_2C phase in the coatings indicates an increase in the plasma enthalpy which causes a rapid heat transfer from the plasma to the flight particles. At high arc voltage of 70 V, a corresponding percentage of crystalline Co_3W_3C phase appeared due to the chemical reaction of melted Co and W with the carbon released from the decomposition of WC. [20]. It also shows the formation of W_2C in the boundaries of WC particles with cobalt which could be an indication of decarburization of the carbides during plasma spray process [21].

3.2. Microstructure of WC-12%Co Coatings

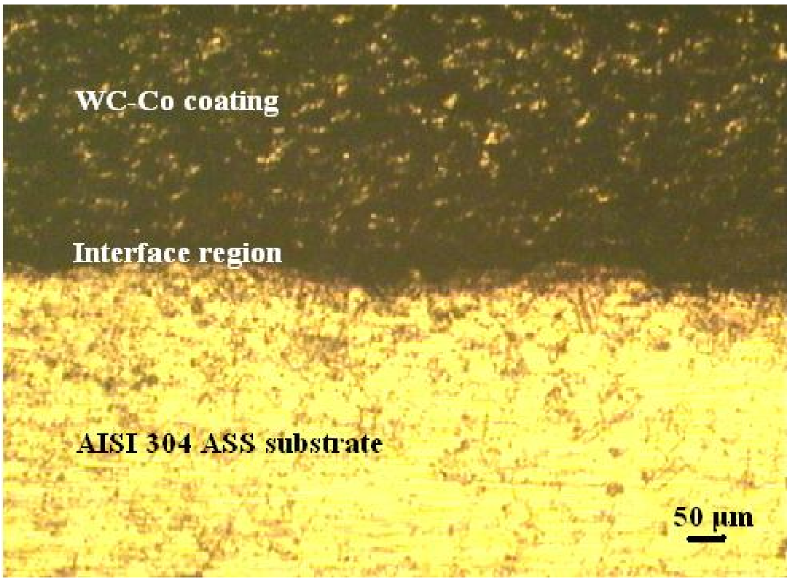

Figure 1. Cross-sectional micrograph of interface and coating

The cross sectional microstructure of the plasma sprayed coating is shown on Figure 1. The coating–substrate interface shows no gaps or cracks, and the reentrant valleys at the substrate surface are all filled by the coating, which are characteristic feature of good adhesion between the coating and the substrate. The presence of frequent carbides in the microstructure was responsible for higher hardness. The absence of micro cracks showed that the processing parameters selected is an optimum combination.

Owing to decarburization and dissolution of the WC in liquid cobalt at high temperatures during spraying [22], as well as thermal and kinetic history of melted particles, the phases present in the coatings differ from those in the powder.

3.3. Microhardness Characterization

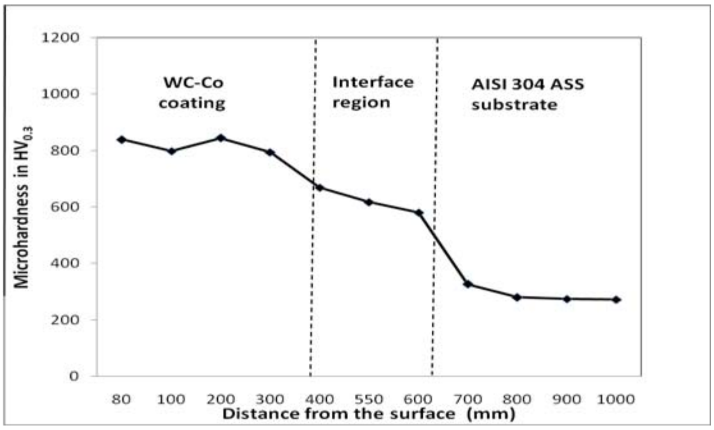

Figure 2. Microhardness variation of the WC-Co coatings

The Vickers hardness of AISI 304 ASS substrate and EN-24 medium carbon steel counter body was 303 $HV_{0.3}$ and 440 $HV_{0.3}$, respectively. Three distinct regions of the coated specimen profile namely plasma sprayed coating, interface and substrate are observed as shown on Figure 2. The micro hardness of the WC-Co plasma coating cross section is found to vary with the distance from the coating-substrate interface. Micro hardness of the coating values were found to be in the range of 795–840 $HV_{0.3.}$ The top of the coating has the maximum hardness value of about 840 $HV_{0.3}$. The interface region showed an intermediate hardness values ranging from 580–670 $HV_{0.3}$. The average micro hardness value is 817 $HV_{0.3}$.

3.4. Friction and Wear Behaviour of WC-12%Co Coatings

The wear of the uncoated and coated specimen at different temperatures is shown on Figure 3.

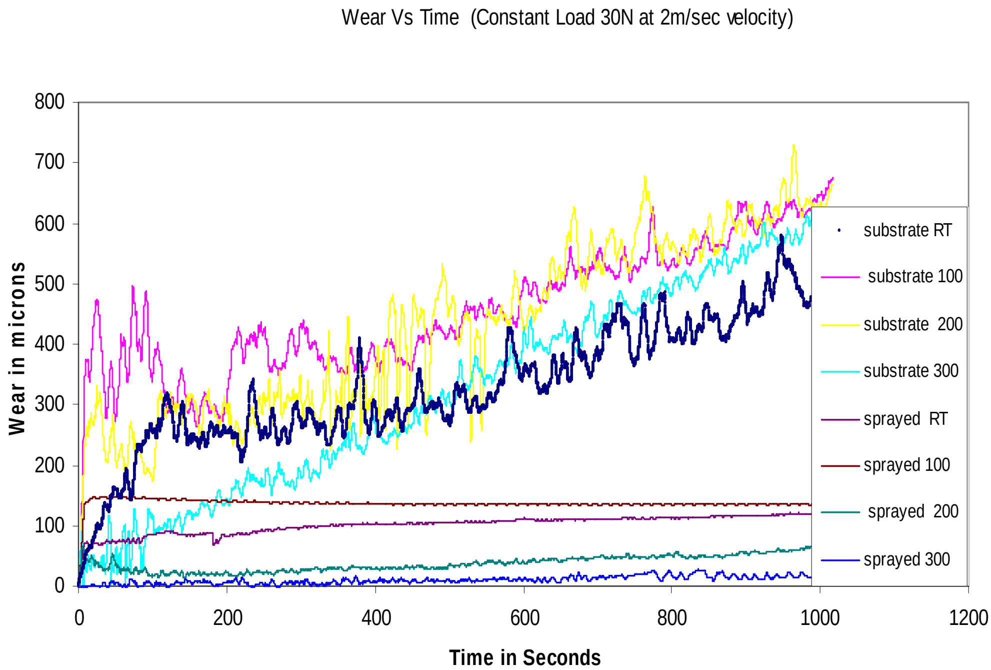

Figure 3. Variation of wear with respect to time and temperature

In uncoated AISI 304 ASS substrate, it was inferred that the wear at 200°C was higher than that of the rest of temperatures. In 100°C, wear rate was initially found to be higher, but as time proceeds it reduces because of the formation of oxide layer. The oxide layers might have induced slipping in sliding wear. Except in 300°C, the uncoated AISI 304 ASS showed severe wear in all operating temperatures. In contrast, the WC-Co coated samples showed very less wear in all operating temperatures. Relative sliding between the contacting surfaces leads to the rupture of these junctions and subsequent material transfer from one surface to the other, in addition to the formation of debris and material loss. The presence of a lubricating oxide film reduces the tendency for adhesive wear occurrence [23].

Coefficient of friction for the uncoated AISI 304 ASS disc in all temperatures varies between 0.45 and 0.62 as shown on Figure 4. In WC-Co coated discs, the CoF was found to be relatively lesser and was ranging from 0.12 to 0.34 in all temperatures. In coated samples worn at 300°C, the CoF was in the range from 0.12 to 0.15. This optimum lower range might be due to the oxide formations like WO_3 and CoO_2 at 300°C.

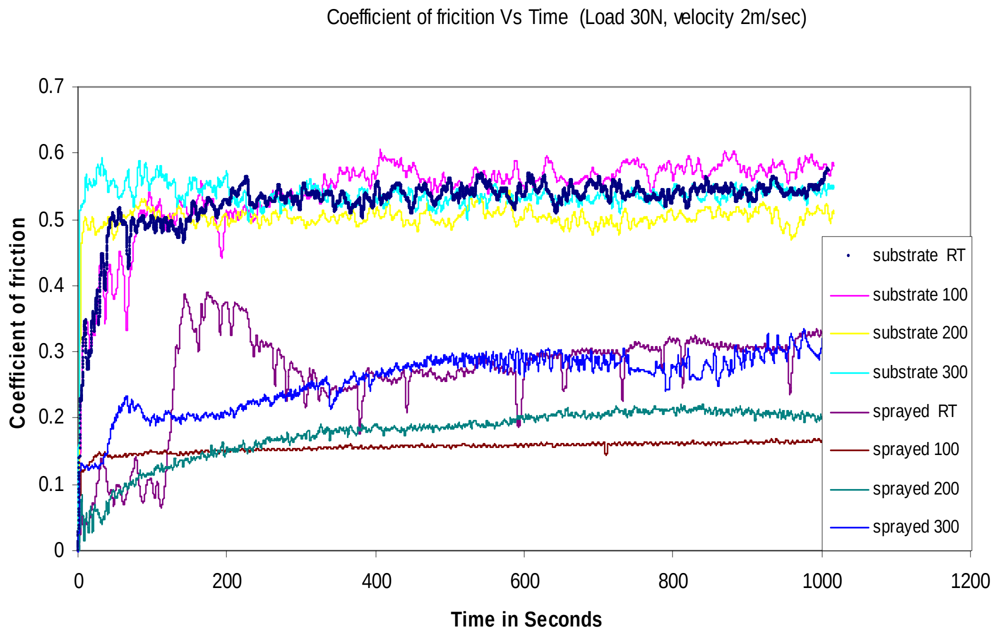

Figure 4. Variation of coefficient of friction with respect to time and temperature

Figure 5 shows the mass loss of the disc in all temperature at coated and uncoated condition, it reveals that in both the condition the mass loss was gradually increased up to 100°C. Then the loss was decreased due to the formation of oxides at elevated temperatures. Wear resistance of the coated and uncoated specimen is compared on Figure 6, which shows the wear resistance was increased normally from 200°C.

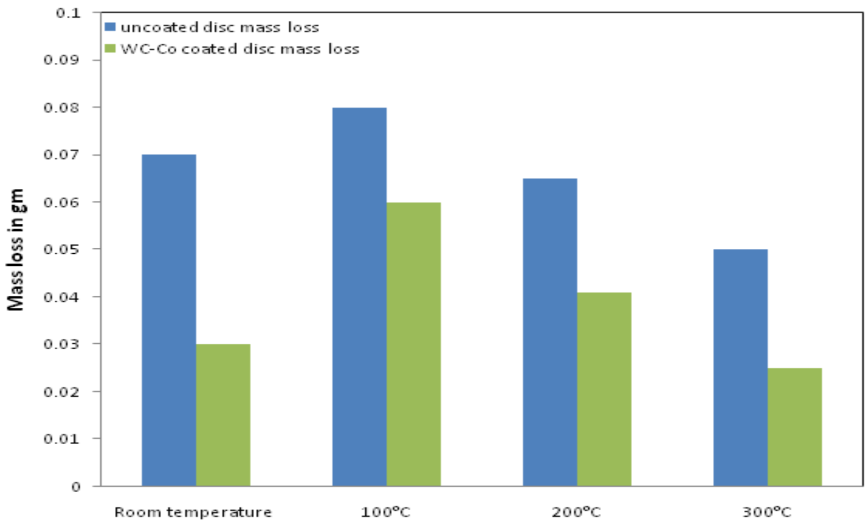

Figure 5. Comparison of mass loss of uncoated and WC-Co coated specimen

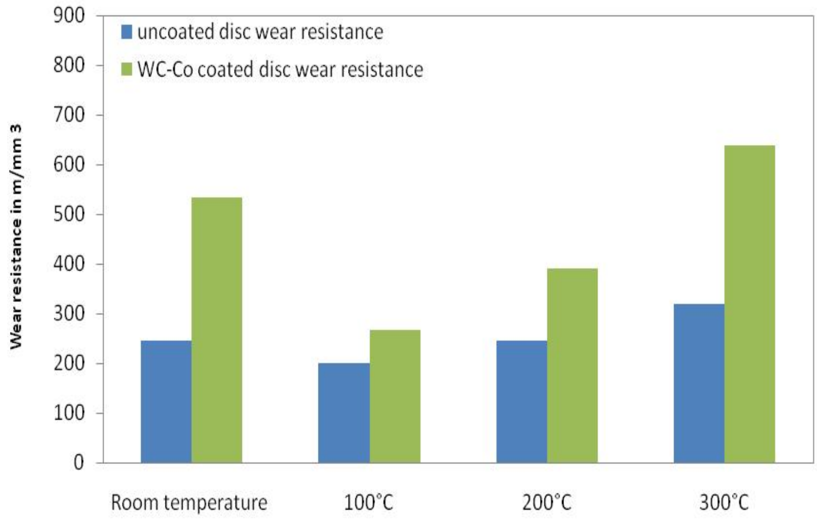

Figure 6. Comparison of wear resistances of uncoated and WC-Co coated specimen

3.5. Phase Composition OF WC-12%Co Powders and coatings

The XRD patterns of the uncoated AISI 304 ASS were shown on Figure 7. It shows the peaks having the phases of γ-Iron (fcc) in all operating temperatures. The XRD patterns of the as-sprayed WC-Co plasma coated surface and the worn tracks of the plasma coated substrates are shown on Figure 8. Notably at 300°C, the wear rate was marginally lesser than the rest of the temperatures due to the initiation of oxide layers, which was observed in XRD analysis. The decarburization, accompanied by the formation of W2C or W during thermal spraying of WC-Co, also results in decreased mechanical properties [24]. The as-sprayed coating which contains both WC and W_2C.At 300°C, the XRD showed the WO_3 phase. The formation of W_2C, W and Co_3W_3C phase can be well explained by the mutual behaviours among the components during the high-temperature plasma spraying. Such phase would improve the bonding among splats [25]. It has been observed that the hardness of the coatings are relatively high and are far higher than expected for cermets with the volume fractions of carbides that are actually observed in the coatings.

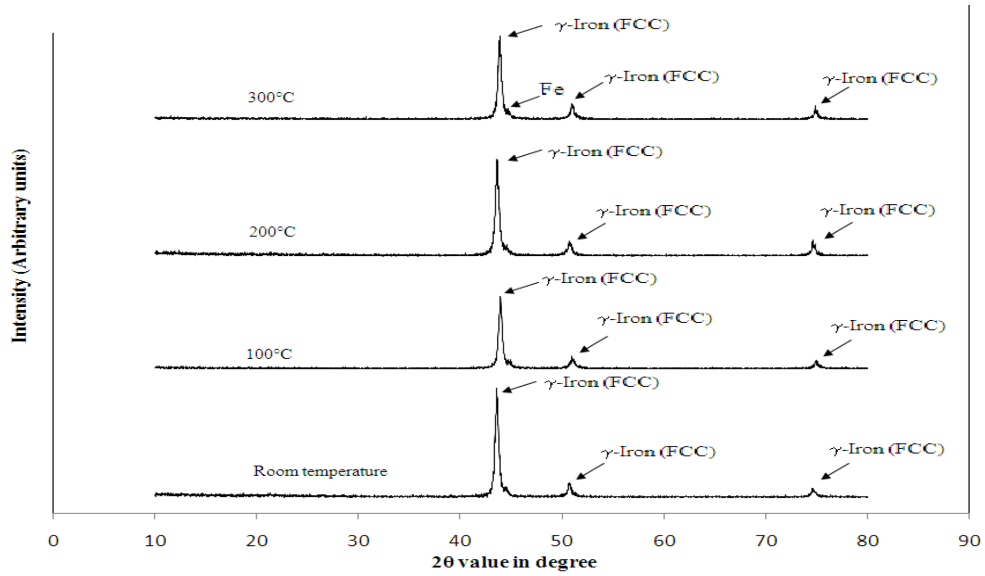

Figure 7. XRD pattern showing phases in worn track of uncoated AISI 304 ASS substrates

Co_3W_3C and Co peaks were also present in smaller intensities. It is also clear that there are no new phases formed in the coating during the thermal spray process. The major intermetallic found in the coated surface was $WC_{1.88}Co_{12}$ in all operating temperatures. In worn track at 300°C, the presence of oxides such asWO_3 and Co O_2 was evident to justify the lesser wear.

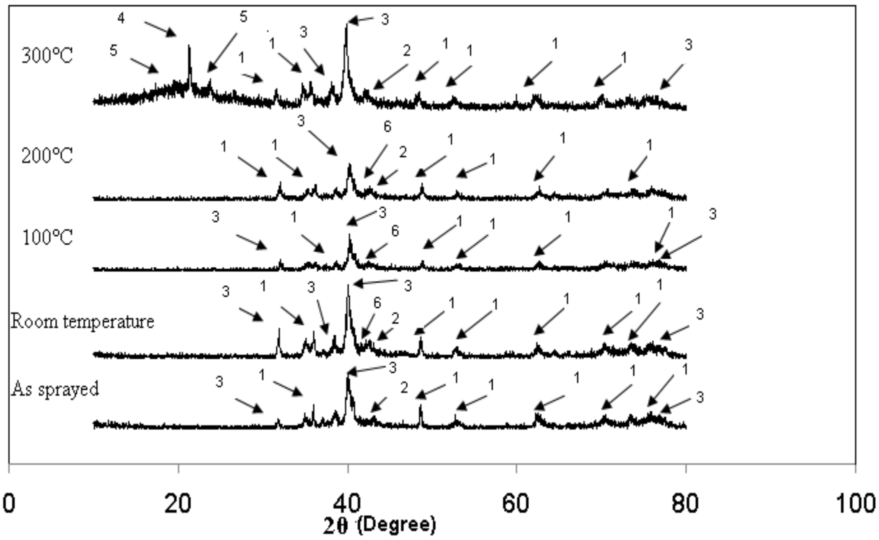

Figure 8. XRD pattern showing phases in the as-sprayed WC-Co coating and worn tracks of the coated samples at various temperatures:1 – WC; 2 – Co; 3 – W_2C; 4 – CoO_2; 5 – WO_3; 6 – CO_3W_3C

3.6. SEM Characterisation of Worn Surfaces

The as-sprayed WC-Co plasma coated surface is shown on Figure 9. The as-sprayed surface also showed the sparsely distributed unmelted spherical particles. These unmelted spherical tungsten powder particles were visible due to the high flight in velocity of the particle.

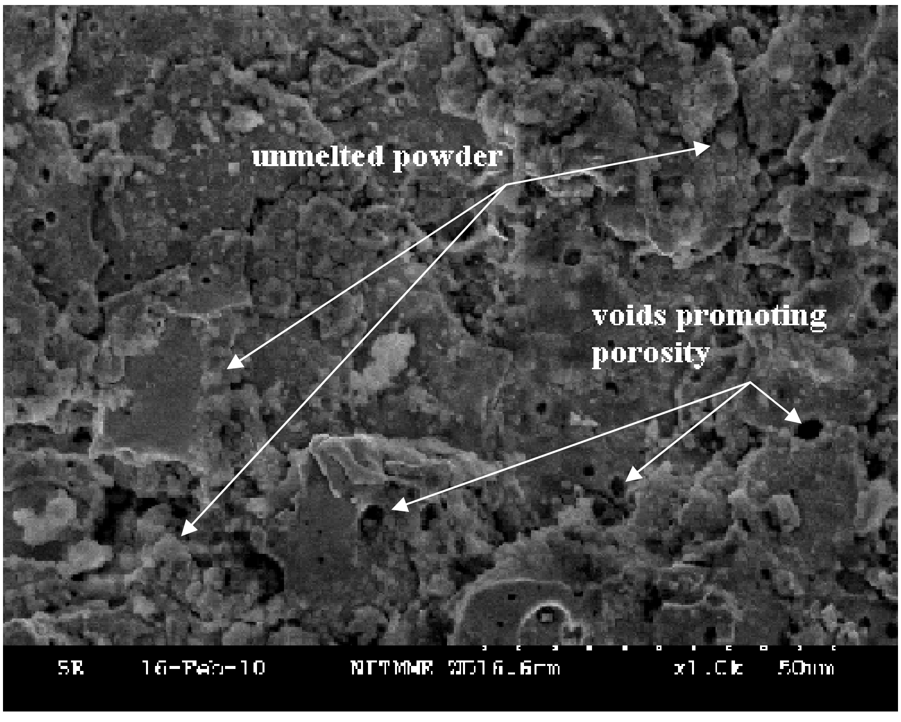

Figure 9. SEM picture of the as-sprayed WC-Co plasma coated surface

The surface morphology of WC-Co coated specimen worn at room temperature is shown on Figure 10 (a). The worn track exhibited delaminated layer with small amount of scabs and debris. As the time progresses, the delaminated layer may peel off and lead to considerable material loss. The wear track formed by sliding wear had a very smooth and shiny appearance. The worn surface morphology of the WC-Co coated sample at 100°C is shown on Figure 10 (b).

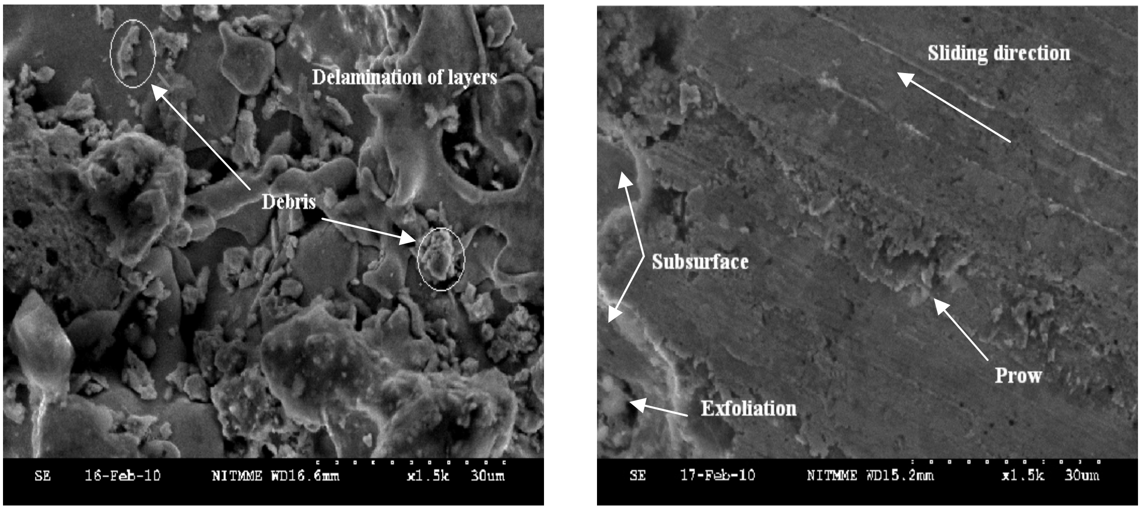

(a) (b)

Figure 10. SEM picture of the WC-Co coated surfaces: (a) worn surface at room temperature; (b) worn surface at 100°C

The mode of wear was found to be exfoliation. Normally exfoliation mode is comparatively severe than delaminated type of material removal. Exfoliation of thick flakes was generally aided by crack formation. The entrapment of debris and asperities between the sliding contact surfaces would obviously increase wear rate of AISI304 ASS substrates by the mechanisms of three-body abrasion, where the entrapped particles serve as an abrasive. The wear resistance at 100°C was found to be lesser than that of the room temperature. The mode of material removal at 200°C was ploughing. These ploughing marks normally starts with the score lines parallel to the sliding direction and later on these lines capitalize to form plough markings. The consequence of this mode of material removal was sub surface cracking which in turn leads to the removal of subsequent layers.

The advanced stage in plough mode of material removal is prow formations. The prow formations were the end result of frequent ploughing on the same instance. This mode leads to more material loss which is shown on Figure 11(a). Dry sliding leads to high local pressure between contacting asperities, which results in plastic deformation, adhesion and the consequent formation of local junctions. The worn surface morphology of WC-Co coated sample at 300°C is shown on Figure 11(b). The mode of material removal is shallow ploughing.

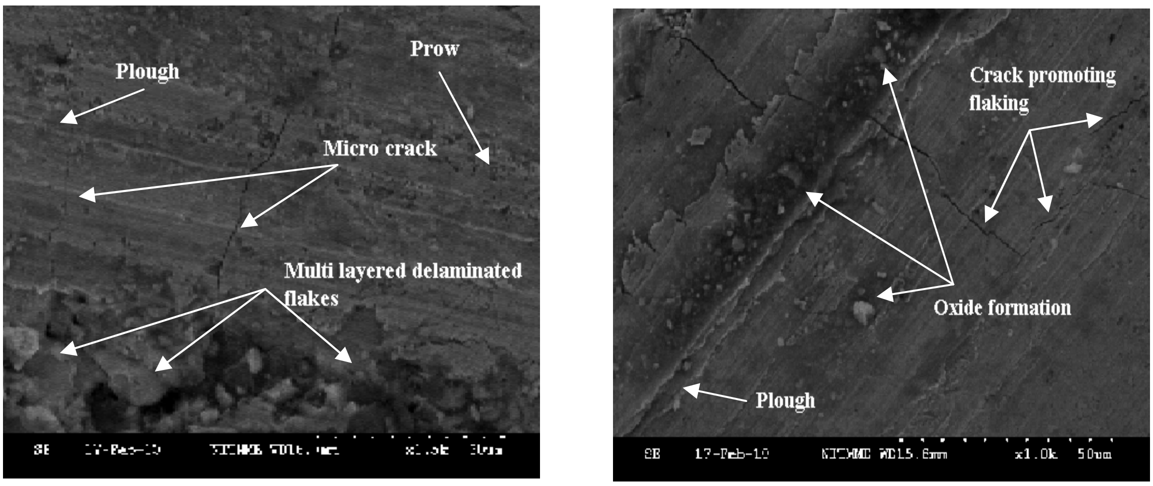

(a) (b)

Figure 11. SEM picture of the WC-Co coated surfaces: (a) worn surface at 200°C; (b) worn surface at 300°C

The score lines, which run always parallel to the sliding direction, were explicitly seen. The interesting phenomenon happened in the interface of the counter body and the coated substrate is oxide formation. The oxide formation is visible in SEM. These oxide layers could be of WO_3 and Co O_2, which was confirmed by XRD analysis (Fig. 4). The Oxide films formed during sliding act as a protective layer, eliminating the chances of excessive material loss. Dry sliding wear leads to the removal of material from the surface by the formation of chips, shavings and fragments. The geometry of the worn surface and a groove formed depends on the size and shape of the worn debris (abrasive particle) [23].

Conclusions

The following conclusions were drawn from the conducted experiments on uncoated and WC-Co plasma sprayed AISI 304 ASS at various operating temperatures.

- The coating up to a thickness of 500 µm was successfully sprayed onto substrate without crystallization, alloying or oxidation.
- A combination of superior bond strength and high hardness was achieved by the plasma spraying.
- The plasma sprayed WC-Co coating exhibited up to five times increase in wear resistance compared to the uncoated AISI 304 ASS substrate.
- The CoF was found to be lower for coated substrate when compared with uncoated at various operating temperatures.
- The wear resistance of the uncoated and WC-Co coated disc was found to be gradually increasing with the increase in test temperature.
- At 100°C, exfoliation found to be dominant wear mechanism. This was converted in to ploughing mode of material removal at 200°C.
- At 300°C, the coated substrate was found to have minimum amount of wear compared with other operating temperatures.
- Oxide layers such as WO_3 and CoO_2 were only formed when the test temperature was around 300°C, which shows the reduced severity of material loss.

References

1. Hsu, K. L., Ahn, T. M., Rigney, D. A. Friction, wear and microstructure of unlubricated austenitic stainless steels, *Wear*, Vol. 60, 1980, p. 13
2. Brin, C., Rivi`ere, Ey., Villain, J.-P. Structural characterization of wear debris produced during friction between two austenitic stainless steel antagonists, *Tribol. Lett.,* Vol. 11 (2), 2001, pp. 127–132.
3. Berndt, C. C., Adhes, J. *Sci. Technol.,* Vol. 7 (12), 1993, p. 1235.
4. Cai, W. D., Lavernia, E. J. *Material Science Engineering A,* No 8, 1997, pp. 226–228.
5. Smith, A. F. *Tribol. Int.,* Vol. 19, 1986 , pp. 65–71.
6. Stott, F. H. Jordan, M. P. The effects of load and substrate hardness on the development and maintenance of wear-protective layers during sliding at elevated temperatures, *Wear,* Vol. 250, 2001, pp. 391–400.
7. Stott, F. H. *Tribol. Int.*, Vol. 31, 1998, pp. 61–71.
8. Gillham, M., van der Jagt, R., Kolster, B. New case hardening process for austenitic stainless Steels, *Mater. World,* Vol. 12, 1996, p. 460.
9. Chen, H., Hutchings, I. M. *Surf. Coat. Technol.,* Vol. 107, 1998, p. 106.
10. Zhao, X. Q., Zhou, H. D., Chen, J. M. Struct. Mater.: Prop. Microstruct. Process, *Mater. Sci. Eng., A* Vol. 431, 2006, p. 290.
11. Qiao, Y., Liu, Y. R., Fischer, T. *J. Therm. Spray Technol.,* Vol. 10, 2001, p. 118.
12. Liao, H., Normand, B., Coddet, C. *Surf. Coat. Technol.,* Vol. 124, 2000, p. 235.
13. Allibert, CH. Sintering features of cemented carbides WC-Co processed from fine powders, *Inter J. Refract. Met. Hard Mater,* Vol. 19, 2001, pp. 53–61.
14. Picas, J. A., Xiong, Y., Punset, M., Ajdelsztajn, L., Forn, A., Schoenung, J. M. Microstructure and wear resistance of WC-Co by three consolidation processing techniques, *Int. J Refract. Met Hard Mater,* Vol. 27, 2009, pp. 344–349.
15. De Villiers Lovelock, H. L. *J. Therm. Spray Technol.,* Vol. 7, 1998, pp. 357–373.
16. Lima, R. S., Karthikeyan, J., Kay, J., Lindemann, C. M., Berndt, C. C. *Thin Solid Films,,* Vol. 416, 2002, pp. 129–135.

17. Vlcek, J., Gimeno, L., Huber, H., Lugscheider, E. A systematic approach to material eligibility for the cold spray process. In: *Thermal Spray: Advancing the Science and Applying the Technology / B. R. Marple, C. Moreau (Eds.).* USA: ASM Inter, 2003, pp. 37–44.
18. Zhu, Y. C., Ding, C. X. ,Yukimura, K., Xiao, T. D., Struttd, P. R. *Ceram. Int*., Vol. 27, 2001, pp. 669–674.
19. *ASTM G99-95*, 1995. *ASTM G99-95a*: standard test method for wear testing with a pin on disk apparatus. Reapproved 2000.
20. Morks, M. F. et al. Microstructure and hardness properties of cermet coating sprayed by low power plasma, *Int. Materials Letters,* Vol. 60, 2006, pp. 1049–1053.
21. Nerz, J,, Kushner, B,, Rotolico, A. Microstructure evaluation of tungsten carbide – cobalt coatings, *Journal of Thermal Spray Technology,* 1992, pp. 1147–52.
22. Nestler, M, Prenzel, C. G., and Seitz, T. HVOF spraying vs. hard chrome plating coating characteristics and aircraft applications. In: *Proceedings of the 15th International Thermal Spray Conference, ASM International,* 1998, pp. 116–125.
23. Hutchings, I. M. *Tribology, Friction and wear of engineering materials,* Butterwort-Heinemann, 1992.
24. Qiao, Y., Fischer, T. E., Dent, A. *Surf. Coat. Technol.,* 2003, pp. 172–174.
25. Lia, H., Khor, K. A., Yu, L. G., Cheang, P. Microstructure modifications and phase transformation in plasma-sprayed WC-Co coatings following post-spray spark plasmasintering, *Surface & Coatings Technology,* Vol. 194, 2005, pp. 96–102.

Received on the 7th of June, 2010

Computer Modelling and New Technologies, 2010, Vol.14, No.3, 41–47
Transport and Telecommunication Institute, Lomonosova 1, LV-1019, Riga, Latvia

UNSTEADY FREE CONVECTION IN A FLUID PAST AN INCLINED PLATE IMMERSED IN A POROUS MEDIUM

***Z. Uddin*[1], *M. Kumar*[2]**

[1]*Department of Applied Sciences and Humanities, ITM University, Sector 23A, Gurgaon-122017, India*
[2]*Department of Mathematics, Statistics and Computer Science*
G. B. Pant University of Agriculture and Technology, Pantnagar –263 145, Uttarkhand, India
E-mail: ziya_dd@rediffmail.com[1]*, mnj_kumar2004@yahoo.com*[2]

Unsteady free convection in a fluid past an infinite inclined plate immersed in a porous medium has been considered for viscous dissipative heat. The problem is governed by a coupled system of non-linear partial differential equations given by Darcy-Brinkman-Forchheimer model. The velocity profile and temperature distributions have been studied using a finite difference scheme. Boundary layer and Boussinesq approximations have been considered. The effect of different parameters entering in the problem, on velocity profile, temperature distribution, local friction factor and local Nusselt number have been computed and studied with the help of graphs. It is observed that as the angle of the plate from vertical direction increases, the value of friction factor and heat transfer coefficients decreases. This problem is interesting for the researchers belonging to chemical and related industry.

Keywords: *viscous dissipation, unsteady free convection, inclined plate, porous medium, non-linear partial differential equations, explicit finite-difference scheme*

1. Introduction

In the past, modelling of viscous dissipation due to flow in a fluid past a porous medium was considered by several authors. An experimental and analytic investigation was carried out by Fand et al. [9] to study the free convection heat transfer from a horizontal cylinder embedded in porous medium consisting of randomly packed glass spheres and the medium is saturated by water or silicon oil. Modelling of viscous dissipation effects on the flow of a fluid in porous medium, which corresponds to Darcy's law, was agreed by several authors [3, 7, 8, 10, 11, 18].

Murthy and Singh [12] have modified the viscous dissipation effect on the flow of an incompressible fluid in a saturated porous medium. They applied the Forchheimer-Darcy model for momentum equation. Neild [15] suggested a modified formula to model viscous dissipation in non-Darcy porous medium. He concluded that modelling of viscous dissipation is related with local drag modelling. Pop and Herwig [17] studied the transient development of the concentration boundary layer with impulsive mass diffusion from a heated vertical surface. The problem of unsteady free convection adjacent to an impulsively heated circular cylinder in porous medium was studied by Bradean et al. [4]. Angirasa et al. [2] investigated combined heat and mass transfer by natural convection with opposing buoyancy effects in a fluid through porous medium. Al-Hadhrami et al. [1] discussed a new model for viscous dissipation in a porous medium across a range of permeability values, and then Neild [16] gave a comment on the paper by [16]. El-Amin et al. [6] studied the effects of viscous dissipation on unsteady free convection in a fluid past a vertical plate immersed in a porous medium. Recently Elgazery, [13], numerically analysed the heat and mass transfer by natural convection in power law fluid past a vertical plate immersed in a porous medium.

In the present investigation, the problem of viscous dissipation effect on unsteady free convection from an inclined plate immersed in porous medium is studied. The Darcy-Brinkman-Forchheimer model is employed to formulate the problem. The dimensionless non-linear partial differential equations are solved numerically using an explicit finite difference scheme. The values of friction factor, heat transfer coefficients, velocity profile and temperature distribution have been determined and studied graphically for steady and unsteady free convection.

2. Formulation

In this problem, the unsteady free convection in a fluid past an inclined flat plate immersed in a porous medium is considered. Initially, the temperature of the fluid and the plate are assumed to be same. At $t' > 0$, the temperature of the plate is raised to T_w' which is then maintained constant.

The temperature of the fluid far away from the plate is T_{∞}'. Physical model and coordinate system are shown in the figure. The Brinkman-Forchheimer model is used to describe the flow in porous media as given by [14] with large porosity and permeability. Under the Boussinesq and boundary layer approximations, the governing mass, momentum and energy conservation equations are:

$$\frac{\partial u'}{\partial x'} + \frac{\partial v'}{\partial y'} = 0, \tag{1}$$

$$\frac{\partial u'}{\partial t'} + u'\frac{\partial u'}{\partial x'} + v'\frac{\partial u'}{\partial y'} = g\beta\cos\theta(T' - T_{\infty}') + \frac{\mu}{\rho}\frac{\partial^2 u'}{\partial y'^2} - \frac{\mu\varepsilon}{\rho K}u' - \frac{F\varepsilon^2}{K^{1/2}}|u'|u', \tag{2}$$

$$\frac{\partial T'}{\partial t'} + u'\frac{\partial T'}{\partial x'} + v'\frac{\partial T'}{\partial y'} = \alpha\frac{\partial^2 T'}{\partial y'^2} + \frac{u'}{C_p}\left[\frac{\mu\varepsilon}{\rho K}u' + \frac{F\varepsilon^2}{K^{1/2}}u'|u'| - \frac{\mu}{\rho}\frac{\partial^2 u'}{\partial y'^2}\right], \tag{3}$$

here, u' and v' are the velocity components along the x' and y' axes. T_w' is the temperature of the plate, while T' is the temperature inside the boundary layer. ρ, α, β, ε, F, μ, K, C_p, θ and g are the density, the thermal diffusivity, the volumetric coefficient of thermal expansion, the porosity, the empirical constant, the fluid viscosity, the permeability, the fluid specific heat, angle of plate from vertical direction and the acceleration due to gravity, respectively.

The initial and boundary conditions are:

$$t' \le 0: \quad u'=0,\ v'=0; \quad T' = T_{\infty}' \quad \text{for all } x' \text{ and } y',$$

$$t' > 0: \begin{cases} u'=0,\ v'=0; \ T'=T_{\infty}' & \text{at } x' = 0. \\ u'=0,\ v'=0; \ T'=T_w' & \text{at } y'=0, \quad x'>0, \\ u'=0, \qquad T'=T_{\infty}' & \text{at } y' \to \infty \quad x'>0. \end{cases} \tag{4}$$

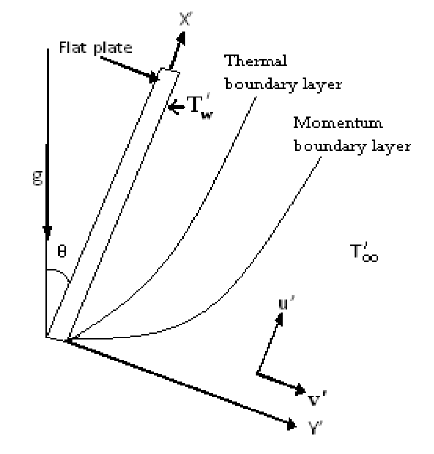

Physical model and coordinate system

The following non-dimensional quantities are introduced:

$$x = x'/L, \quad y = y'/L, \quad u = u'/U, \quad v = v'/U,$$

$$T = (T' - T_{\infty}')/(T_w' - T_{\infty}') \text{ and } t = Ut'/L, \tag{5}$$

here U is the reference velocity L is reference length scale. Using (5), equations (1)–(3) reduce to:

$$\frac{\partial u}{\partial x} + \frac{\partial v}{\partial y} = 0, \tag{6}$$

$$\frac{\partial u}{\partial t} + u\frac{\partial u}{\partial x} + v\frac{\partial u}{\partial y} = Gr.T.\cos\theta + \frac{\partial^2 u}{\partial y^2} - \frac{1}{Da}u - \frac{Fr}{Da}|u|u, \tag{7}$$

$$\frac{\partial T}{\partial t} + u\frac{\partial T}{\partial x} + v\frac{\partial T}{\partial y} = \frac{1}{\mathrm{Pr.Re}}\frac{\partial^2 T}{\partial y^2} + Ec.u\left[\frac{1}{Da}u + \frac{Fr}{Da}u|u| - \frac{\partial^2 u}{\partial y^2}\right], \tag{8}$$

here $Gr = Lg\beta(T_w' - T_{\infty}')/U^2$ is the Grashof number, $Da = K/L^2\varepsilon$ is the Darcy number, $Fr = F\varepsilon K^{1/2}/L$ is the inertia coefficient, $Pr = \mu/\rho\alpha$ is the Prandtl number, $Re = \rho LU/\mu$ is the Reynolds number and $Ec = U^2/C_p(T_w' - T_{\infty}')$ is the Eckert number.

The initial and boundary conditions are now given by:

$$t \le 0: \quad u = v = T = 0, \quad \text{for all } x \text{ and } y,$$

$$t > 0: \begin{cases} u = v = T = 0, & \text{at } x = 0, \\ u = v = 0,\ T = 1 & \text{at } y = 0, \quad x > 0, \\ u = 0, \quad T = 0 & \text{at } y \to \infty, \quad x > 0. \end{cases} \tag{9}$$

The wall shear stress is given by:

$$\tau_w = \mu\left(\frac{\partial u'}{\partial y'}\right)_{y'=0} = \frac{\mu U}{L}\left(\frac{\partial u}{\partial y}\right)_{y=0}. \tag{10}$$

Therefore Local friction factor is given by:

$$C_f = \frac{2\tau_w}{\rho U^2} = 2\left(\frac{\partial u}{\partial y}\right)_{y=0}. \tag{11}$$

From the definition of the local surface heat flux,

$$q_w = -k_e\left(\frac{\partial T'}{\partial y'}\right)_{y'=0} = -k_e\frac{\left(T'_w - T'_\infty\right)}{L}\left(\frac{\partial T}{\partial y}\right)_{y=0}, \tag{12}$$

here k_e is the effective thermal conductivity of the saturated porous medium, together with the definition of local Nusselt number

$$Nu = \frac{q_w}{\left(T'_w - T'_\infty\right)k_e} = -\left(\frac{\partial T}{\partial y}\right)_{y=0}. \tag{13}$$

3. Method of Solution

The numerical integration was carried out using the time dependent form of non-linear partial differential equations (6)–(8) using the initial and boundary conditions (9). However, exact solution is not possible for this set of equations and hence these may be solved by explicit finite-difference method as explained by Carnahan et al. [5]. The equivalent finite-difference schemes of equations for (6) to (8) are as follows:

$$\left(u_{i,j}^{k+1} - u_{i-1,j}^{k+1}\right)/\Delta x + \left(v_{i,j}^{k+1} - v_{i-1,j}^{k+1}\right)/\Delta y = 0, \tag{14}$$

$$\begin{aligned}&\left(u_{i,j}^{k+1} - u_{i,j}^{k}\right)/\Delta t + u_{i,j}^{k}\left(u_{i,j}^{k} - u_{i-1,j}^{k}\right)/\Delta x + v_{i,j}^{k}\left(u_{i,j+1}^{k} - u_{i,j}^{k}\right)/\Delta y = \\ &GrT'\cos\theta + \left(u_{i,j+1}^{k} - 2u_{i,j}^{k} + u_{i,j-1}^{k}\right)/(\Delta y)^2 - (1/Da)u_{i,j}^{k} - (Fr/Da)\,|\,u_{i,j}^{k}\,|\,u_{i,j}^{k},\end{aligned} \tag{15}$$

$$\begin{aligned}&\left(T_{i,j}^{k+1} - T_{i,j}^{k}\right)/\Delta t + u_{i,j}^{k}\left(T_{i,j}^{k} - T_{i-1,j}^{k}\right)/\Delta x + v_{i,j}^{k}\left(T_{i,j+1}^{k} - T_{i,j}^{k}\right)/\Delta y \\ &= \left(T_{i,j+1}^{k} - 2T_{i,j}^{k} + T_{i,j-1}^{k}\right)/\Pr.\mathrm{Re}.(\Delta y)^2 + \\ &Ec.u_{i,j}^{k}\left\{(1/Da)u_{i,j}^{k} + (Fr/Da)\,|\,u_{i,j}^{k}\,|\,u_{i,j}^{k} - \left(u_{i,j+1}^{k} - 2u_{i,j}^{k} + u_{i,j-1}^{k}\right)/(\Delta y)^2\right\}.\end{aligned} \tag{16}$$

The index i refers to x, index j refers to y and index k refers to time. The mesh is divided by taking $\Delta x = 2.5$, $\Delta y = 2.5$ and $\Delta t = 0.1$. The space and time steps are selected such that the solutions are not dependent on it, i.e. it fulfils the subjective criteria of the method. During any one time step, the coefficient $u_{i,j}^{k}$ and $v_{i,j}^{k}$ appearing in equations (14)–(16) are treated as constants. Then at the end of any time step Δt, the new temperature T and new velocity components u and v at all interior grid points was determined by successive applications of equations (14)–(16). This process is repeated in time and, provided the time step is sufficiently small, u, v and T should eventually converges to values which approximate the steady state solution of the governing equations (14)–(16).

A selected set of values has been obtained covering the range $0.1 \le Da \le 10$, $0.0 \le Ec \le 0.2$, $0.0 \le Gr \le 5$, $0.0 \le Fr \le 2$, $Re = 10$, $Pr = 10$. The spatial domain under investigation was restricted to finite dimension, such that the length of the plate x_{max} was assumed to be 100 and the boundary layer thickness y_{max} was assumed to be 35.

4. Results and Discussion

To study the velocity profile and temperature distributions, these have been plotted on Figure 1 for different values of time. It is noticed that after time t = 250, there is no major change in velocity profile and temperature distribution i.e. the steady state is achieved at t = 250. The depiction of the graph shows that velocity first increases near the plate and approaches to zero as move away from the plate and temperature always decreases as move away from the plate. It also has been observed that the momentum boundary layers thickness ($\delta_x \approx 20$) is thicker than thermal boundary layer thickness ($\delta_t \leq 10$). Velocity profile for steady state has been drawn graphically on Figure 2. It is noted that at steady state the velocity increases with an increase of x.

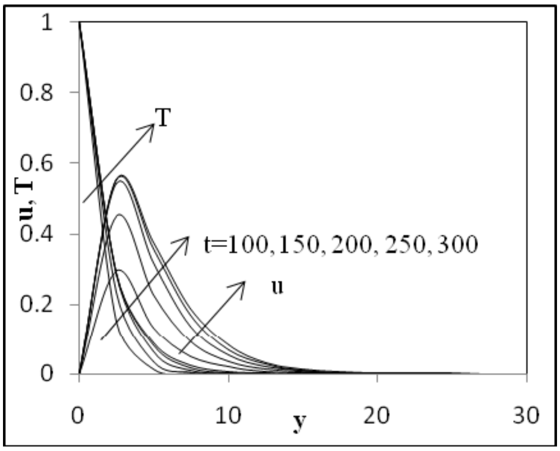

Figure 1. Unsteady velocity and Temperature profiles for various times at Da = 10, Ec = 0.01, Fr = 0.5, Gr = 1.0, Pr = Re = 10 and x = 53

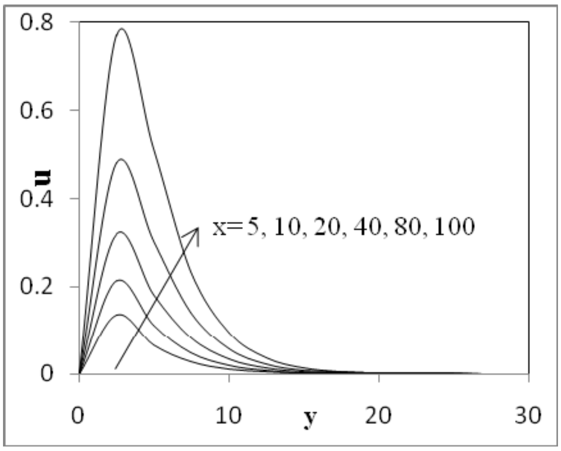

Figure 2. Unsteady velocity profile as a function of y for different positions x with Gr = 1, Fr = 0.5, Da = 10, Pr = Re = 10 and Ec = 0.01

On Figure 3 and 4 the velocity profile and temperature distribution for steady state as a function of y for different values of angle of inclination is showed. The velocity profile as well as the temperature distribution both decrease with the increase in angle of inclination from vertical direction as also shown in tabular form in Table 1 and Table 2.

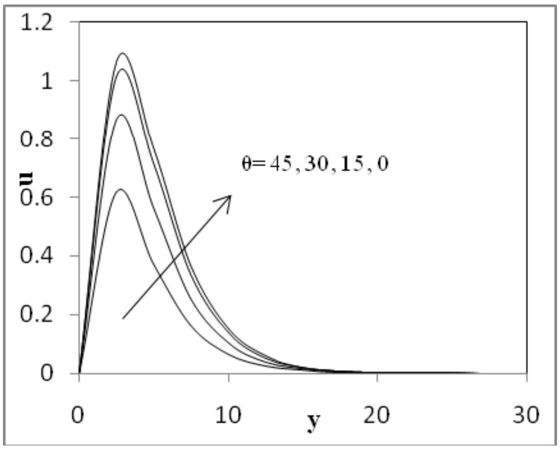

Figure 3. Velocity profile as a function of y for different angles with Gr = 1, Fr = 0.5, Da = 10, Pr = Re = 10 and Ec = 0.01

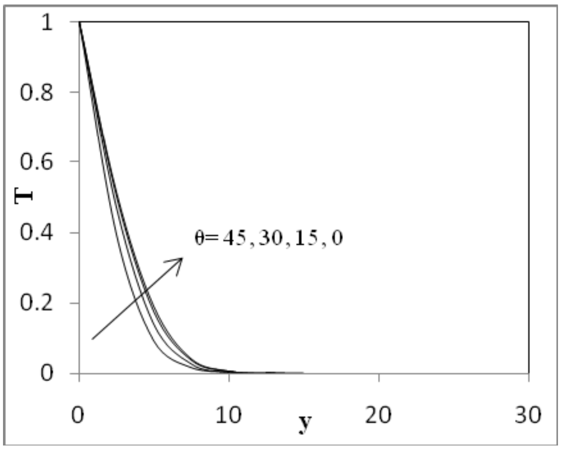

Figure 4. Temperature distribution as a function of y for different angles with Gr = 1, Fr = 0.5, Da = 10, Pr = Re = 10 and Ec = 0.01

The result for steady state local friction factor and local Nusselt number, as a function of x for various values of Darcy's number (*Da*) is displayed on Figures 5 and 6. From Figure 5, it is observed that as x increases, local friction factor increases. For small values of *Da*, the effect of position x on local friction factor is very small, but for large values of *Da*, opposite is true. On Figure 6 we noted that as *Da* increases heat transfer rate increases in the starting, but decreases later, and for small values of *Da*, the effect of position x on heat transfer rate is very small.

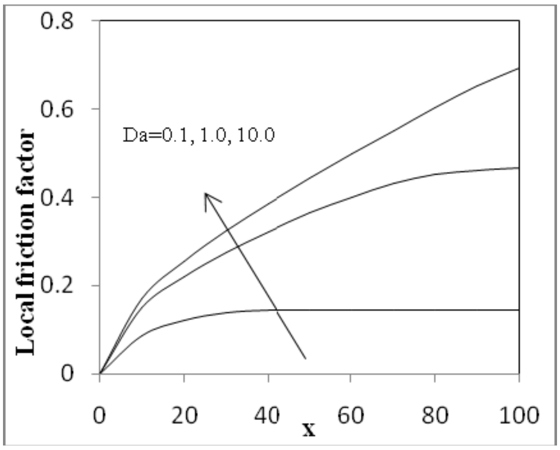

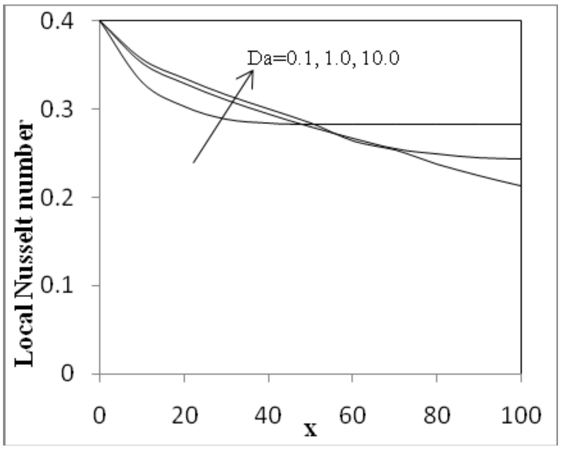

Figure 5. Steady local friction factor as a function of x, for various Da with Fr= 0.5, Gr = 1, Pr = Re = 10,c = 0.01 and $\theta = 30^0$

Figure 6. Steady local Nusselt number as a function of x, for various Da with Fr = 0.5, Gr = 1, Pr = Re = 10, Ec = 0.01 and $\theta = 30^0$

Steady state local friction factor and local Nusselt number are plotted as a function of x for angle of inclination $\theta = 30^o$ and for different values of *Ec* on Figures 7 and 8. Figure 7 shows that for small values of *Ec*, there is a small change in local friction factor with respect to x; while for large values of *Ec*, local friction factor increases very rapidly with the increase in x. From figure 8, it is clear that as *Ec* increases (inertial force increases) i.e. viscous dissipation increases, the rate of heat transfer decreases.

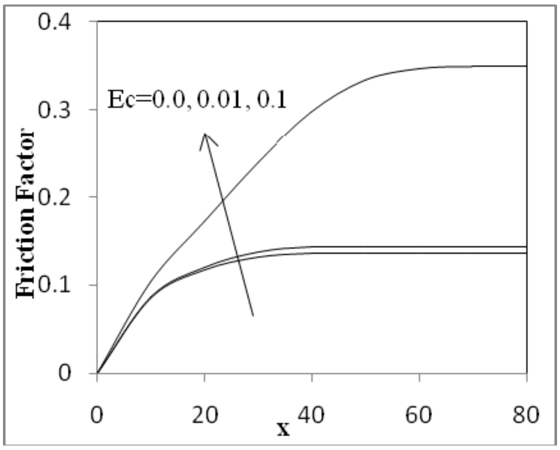

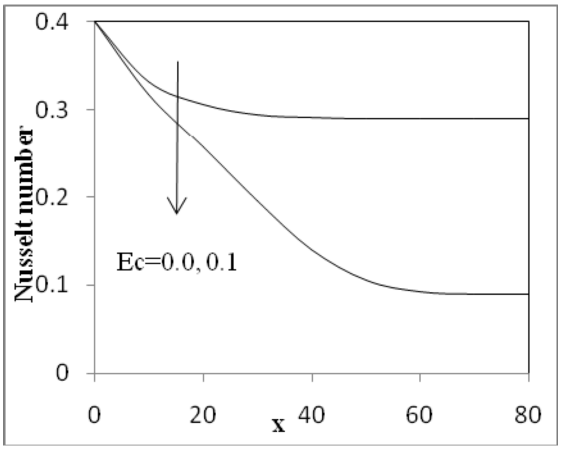

Figure 7. Steady friction factor as a function of x, for various Ec with Fr = 0.5, Gr = 1, Pr = Re = 10, Da = 1 and $\theta = 30^0$

Figure 8. Steady local Nusselt number as a function of x, for various Ec with Fr = 0.5, Gr = 1, Pr = Re = 10, Da = 1 and $\theta = 30^0$

The authors also studied the effect of inertial coefficient Fr on steady state local friction factor and local Nusselt number as a function of x and presented graphically through Figures 9 and 10. It is clear that, as *Fr* increases, local friction factor decreases, while it has a slight effect on local Nusselt number.

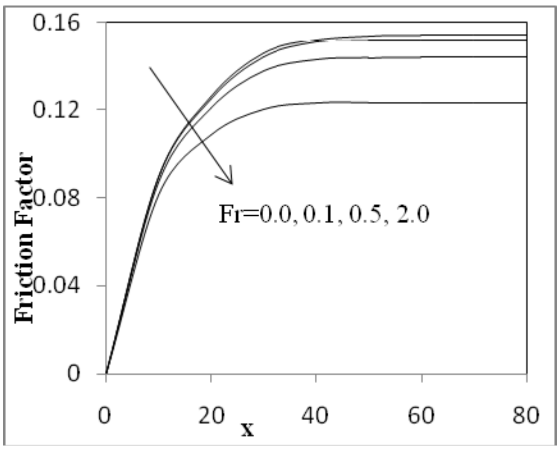

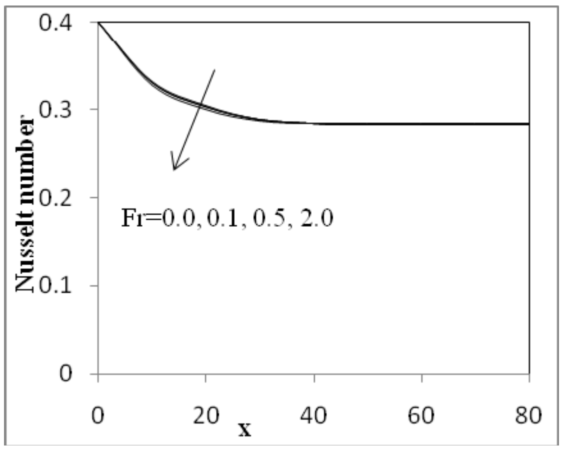

Figure 9. Steady friction factor as a function of x, for various Fr with Da = 1, Gr = 1, Pr = Re = 10, Ec = 0.01 and $\theta = 30^0$

Figure 10. Steady local Nusselt number as a function of x, for various Fr with Da = 1, Gr = 1, Pr = Re = 10, Ec = 0.01 and $\theta = 30^0$

The effect of Grashoff number on local friction factors and local Nussselt numbers are plotted as a function of x for $\theta = 30^o$ on Figures 11 and 12 respectively. As Groshoff number increases, i.e. buoyancy force dominates velocity the local friction factor increases, as shown on Figure 11. From Figure 12, it is clear that as *Gr* increases the value of local Nusselt number increases in the starting but later it decreases.

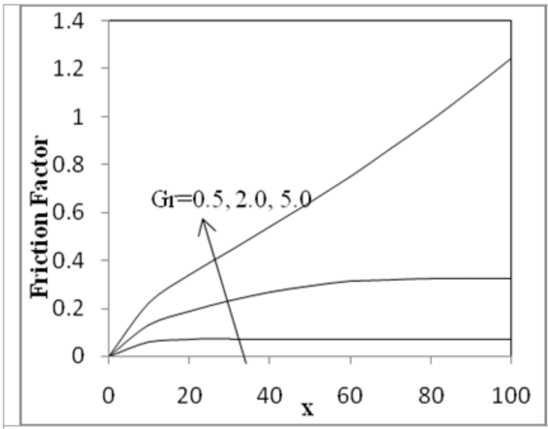

Figure 11. Steady local friction factor as a function of x, for various Gr with Fr=0.5, Da=1, Pr=Re=10, Ec=0.01 and $\theta=30^0$

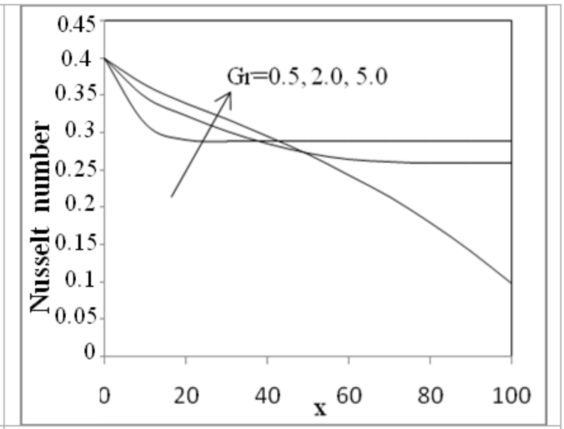

Figure 12. Steady local Nusselt number as a function of x, for various Gr with Fr=0.5, Da=1, Pr=Re=10, Ec=0.01 and $\theta=30^0$

On Figures 13 and 14 the effect of angle of inclination of plate from vertical on local friction factor and local Nusselt number is studied. The Figure 13 shows that the values of local friction factors decreases with the increase in angle of inclination, while Figure 14 indicates that local Nusselt number slightly effected by the change in angle of inclination.

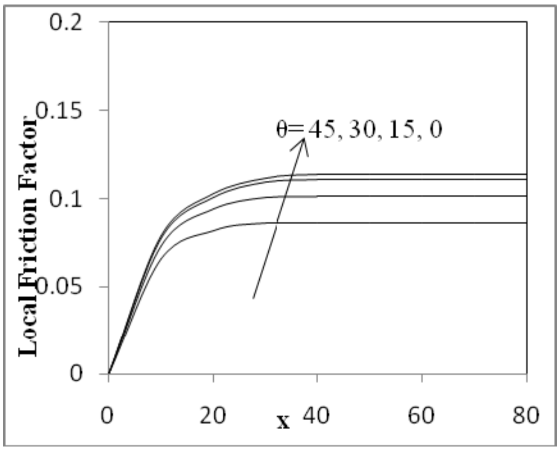

Figure 13. Local friction factor as a function of x for different angles with Gr=1, Fr=0.5, Da=10, Pr=Re=10 and Ec=0.01

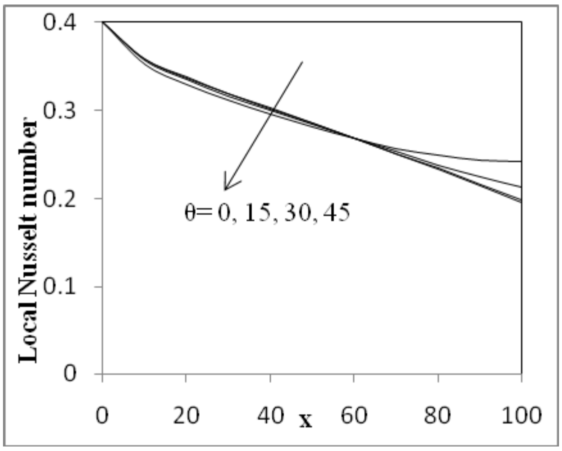

Figure 14. Local Nusselt number as a function of x for different angles with Gr=1, Fr=0.5, Da=10, Pr=Re=10 and Ec=0.01

Table 1. Velocity profile at different angles for different angles with Gr = 1, Fr = 0.5, Da = 10, Pr = Re = 10 and Ec = 0.01

y	Θ = 0	Θ = 15	Θ = 30	Θ = 45
0	0	0	0	0
2.5	1.0619	1.0137	0.8647	0.6148
5	0.7689	0.7152	0.5662	0.3715
7.5	0.3682	0.3367	0.256	0.1619
10	0.1503	0.1364	0.102	0.0639
12.5	0.0578	0.0523	0.0389	0.0241
15	0.0217	0.0197	0.0146	0.0091
17.5	0.0081	0.0073	0.0054	0.0034
20	0.003	0.0027	0.002	0.0013
22.5	0.0011	1.00E-03	8.00E-04	5.00E-04
25	4.00E-04	4.00E-04	3.00E-04	2.00E-04
27.5	2.00E-04	1.00E-04	1.00E-04	1.00E-04
30	1.00E-04	1.00E-04	0	0

Table 2. Temperature at different angles for different angles with Gr = 1, Fr = 0.5, Da = 10, Pr = Re = 10 and Ec = 0.01

y	Θ = 0	Θ = 15	Θ = 30	Θ = 45
0	1	1	1	1
2.5	0.5126	0.5033	0.4692	0.3954
5	0.1904	0.1765	0.1384	0.0945
7.5	0.0419	0.0371	0.0259	0.0157
10	0.0068	0.0059	0.0039	0.0022
12.5	1.00E-03	8.00E-04	5.00E-04	3.00E-04
15	1.00E-04	1.00E-04	1.00E-04	0
17.5	0	0	0	0

References

1. Al-Hadhrami, A. K., Elliott, L. and Ingham, D. B. A new model for viscous dissipation in a porous medium across a range of permeability values, *Transport in Porous Media,* Vol. 53, 2003, pp. 117–122.
2. Angirasa, D., Peterson, G. P. and Pop, I. Combined heat and mass transfer by natural convection with opposing buoyancy effects in a fluid saturated porous medium, *Int. J. Heat Mass Transfer,* Vol. 40, 1997, pp. 2755–2773.
3. Bejan, A. *Convection Heat Transfer, 2nd ed*. New York: Wiley, 1995, pp. 523–527.
4. Bradean, R., Ingham, D. B., Heggs, P. J. and Pop, I. Unsteady free convection adjacent to an impulsively heated horizontal circular cylinder in porous media, *Num. Heat Transfer Part A*, Vol. 31, 1997, pp. 325–346.
5. Carnahan, B., Luther, H. A. and Wilkes, J. O. *Applied Numerical Methods*. New York: Wiley, 1969, pp. 474–481.
6. El-Amin, M. F. and Ebrahiem, N. A., Effect of viscous dissipation on unsteady free convection in a fluid past a vertical plate immersed in a porous medium, *Transport in Porous Media,* Vol. 64, 2006, pp. 1–14.
7. El-Amin, M. F., El-Hakiem, M. A. and Mansour, M. A. Effect of viscous dissipation on a power law fluid over plate embedded in porous medium, *Heat Mass Transfer,* Vol. 39, 2003, pp. 807–813.
8. El-Amin, M. F. Combined effect of magnetic field and viscous dissipation on a power law fluid over plate with variable surface heat flux embedded in porous medium, *J. Magnetism Magnetic Materials*, Vol. 261, 2003, pp. 228–237.
9. Fand, R. M., Steinberger, T. E. and Cheng, P, Natural convection heat transfer from a horizontal cylinder embedded in a porous medium, *Int. J. Heat Mass Transfer,* Vol. 29, 1986, pp. 119–133.
10. Magyari, E. and Keller, B. The opposing effect of viscous dissipation allows for parallel free convection boundary layer flow along a cold vertical flat plate, *Transport in Porous Media*, Vol. 51, No a, 2003, pp. 227–230.
11. Magyari, E. and Keller, B. Buoyancy sustained by viscous dissipation, *Transport in Porous media,* Vol. 53, No b, 2003, pp. 105–115.
12. Murthy, P. V. S. N. and Singh, P. Effect of viscous dissipation on a non- Darcy natural convection regime, *Int. J. Heat Mass Transfer,* Vol. 40, 1997, pp. 1251–1260.
13. Naseer S. Elgazery. Transient analysis of heat and mass transfer by natural convection in power law fluid past a vertical plate immersed in a porous medium (numerical study), *Applications and Applied Mathematics*, Vol. 3, No 2, 2008, pp. 267–285.
14. Nield, D. A. and Bejan, A. C*onvection in Porous Media, 2nd ed.* New York: Springer-Verlag, 1999.
15. Nield, D. A. Resolution of a paradox involving viscous dissipation and non-linear drag in a porous medium, *Transport in porous media,* Vol. 41, 2000, pp. 349–357.
16. Nield, D. A. Comments on 'A new model for viscous dissipation in a porous medium across a range of permeability values' in Transport in Porous Media 53 (2003), 117–122, *Transport in Porous Media,* Vol. 55, 2004, pp. 253–254.
17. Pop, I. and Herwig, H. Transient mass transfer from an isothermal vertical flat plate embedded in a porous medium, *Int. Comm. Heat Mass Transfer,* Vol. 17, 1990, pp. 813–821.
18. Rees, D. A. S., Magyari, E. and Keller, B. The development of the asymptotic viscous dissipation profile in a vertical free convective boundary layer flow in a porous medium, *Transport in Porous Media,* Vol. 53, 2003, pp. 347–355.

Received on the 20th of April, 2010

Computer Modelling and New Technologies, 2010, Vol.14, No.3, 48–62
Transport and Telecommunication Institute, Lomonosova 1, LV-1019, Riga, Latvia

ANN BASED RIVER STAGE – DISCHARGE MODELLING FOR GODAVARI RIVER, INDIA

***D. C. S. Bisht*[1], *M. M. Raju*[2], *M. C. Joshi*[3]**

[1]Department of Mathematics, School of Basic Sciences, ITM, University, Gurgaon, India
E-mail: dcsbisht@gmail.com
[2]Research Associate (Soil and Water Engineering) A. P. Water Management Project, The Netherlands Assisted FAO Project, RARS Polasa, Jagtial – 505327, Karimnagar(Dt.), Andhra Pradesh, India
E-mail: mmraju.swce@gmail.com
[3]Department of Mathematics, Statistics and Computer Science, College of Basic Sciences and Humanities, G.B. Pant University of Agriculture and Technology
Pantnagar-263 145, Uttarakhand, India
E-mail: mcjoshi@69gmail.com

The present study was carried out to develop river stage discharge modelling using artificial neural network (ANN) and Linear Multiple Regression (LMR) methods. From the literature and the developed models, it is clear that ANN models for river stage-discharge are more efficient than the other traditional modelling methods. Twenty ANN models were developed in the study in which ten models were one hidden layer models and ten models with two hidden layers. The best five ANN models were selected in each one hidden layer methodology and two hidden layers methodology. Finally five best ANN models out of all the developed ANN models were selected.

The developed models were trained, tested & validated on the data of Godavari River at Rajahmundry, Dhawalaishwaram Barrage site in Andhra Pradesh. Comparing observed data and the estimated data through developed ANN models, it has been proved that the developed ANN models show good results and are better than the traditional models, like LMR.

Keywords: *artificial neural network, training, testing, validation, learning, stage-discharge*

1. Introduction

Management of water resources requires input from hydrological studies. This is mainly in the form of estimation or forecasting of the magnitude of a hydrological variable like rainfall and runoff using past experience. Such forecasts are useful in many ways. They provide a warning of the flood extremes or drought conditions and help to optimise the operation of systems like reservoirs and power plants.

A large number of hydrological analyses require mapping and modelling of non-linear systems data. Traditionally such mapping is performed with the help of conceptual models or statistical tools such as regression and curve fitting. However, when the underlying physical laws are unknown or not precisely known, it is rather difficult to model the phenomenon adequately. Attempts have been made to develop a technique that does not require algorithm or rule development and thus reduces the complexity of the software. One such technique is known as neurocomputing, and the networks laid out with many parallel processing elements to do this neurocomputing are called artificial neural networks. Flood forecasting is vital for reducing the damage and loss of life caused by river flooding; flood warning-evacuation systems are the most realistic way to cope with large floods (Davies and Hall, 1992).

Keeping the above scenario of real time flood forecasting, the present study was taken up in developing a neural network model for the river discharge using the past river stage and discharge as inputs for specified lag time. The feed forward multilayer neural network has been trained using back propagation algorithm for the present river stage-discharge modelling, because it is a good choice for implicit and complicated system modelling and is capable for solving a very large domain of learning problems (Webros, 1974; Rumelhart et al., 1986). ANN is the most widely accepted machine learning method and is widely used in various areas of water-related research such as rainfall-runoff modelling (Dawson and Wilby, 1998; Dibike and Solomatine, 2000), prediction of discharge (Muttiah et al., 1997). Three layered feed forward ANNs have been shown to be a powerful tool for input-output mapping and have been widely used in water resources engineering problems (ASCE Task Committee, 2000). ANNs were found to be very efficient in modelling stage-discharge relationship (Bhattacharya and Solomatine, 2000; Jain and Chalisgaonkar, 2000). Jain (2001) used the ANN approach to establish an integrated stage-discharge-sediment concentration relation for two sites on the Mississipi River and showed that the ANN results were much closer to the observed values than the conventional technique. Nagy et al. (2002) applied ANN technique to estimate the natural sediment discharge in rivers in terms of sediment concentration and addressed the importance of choosing an appropriate neural network structure and providing field data to that network for training purpose. ANN models perform better than the physically-based models for simulating sediment loads from different slopes and different rainfall intensities (Tayfur, 2002). ANN approach gives better results compared to several commonly used formulas of sediment discharge. (Cigizoglu, 2004; Kisi, 2004a; Lin and Namin, 2005; Tayfur and Guldal, 2006), ANN and fuzzy models were found to be considerably better than conventional rating curve method (Lohni et al., 2007). Kisi (2007) and Rai and Mathur (2008) investigated good application efficiency of ANNs in the sediment yield modelling and when compared with the conventional modelling techniques. The present study is aimed at developing a stage-discharge prediction model using ANN technique. The developed models were trained, tested and validated for the Godavari River system at Dhawalaishwaram barrage site (Rajahmundry) in Andhra Pradesh. The developed ANN models were also compared with Linear Multiple Regression (LMR) models for the same data. The study comprises of the following objectives:

i. ***Development of river stage-discharge artificial neural network models.***
ii. ***Validation of the formulated models.***
iii. ***Performance evaluation of the formulated models for the Godavari River system.***
iv. ***Comparison of ANN and LMR models.***

2. Artificial Neural Networks (ANNs)

An ANN is network of parallel, distributed information processing system that relates an input vector to an output vector. It consists of a number of information processing elements called neurons or nodes, which are grouped in layers. The neuron collects inputs from both a single and multiple sources and produces output in accordance with a predetermined non-linear function. An ANN model is created by interconnection of many of the neurons in a known configuration. The primary elements characterizing the neural network are the distributed representation of information, local operations and non-linear processing. Figure 1 shows the general structure of a Multilayer feed – forward artificial neural network configuration.

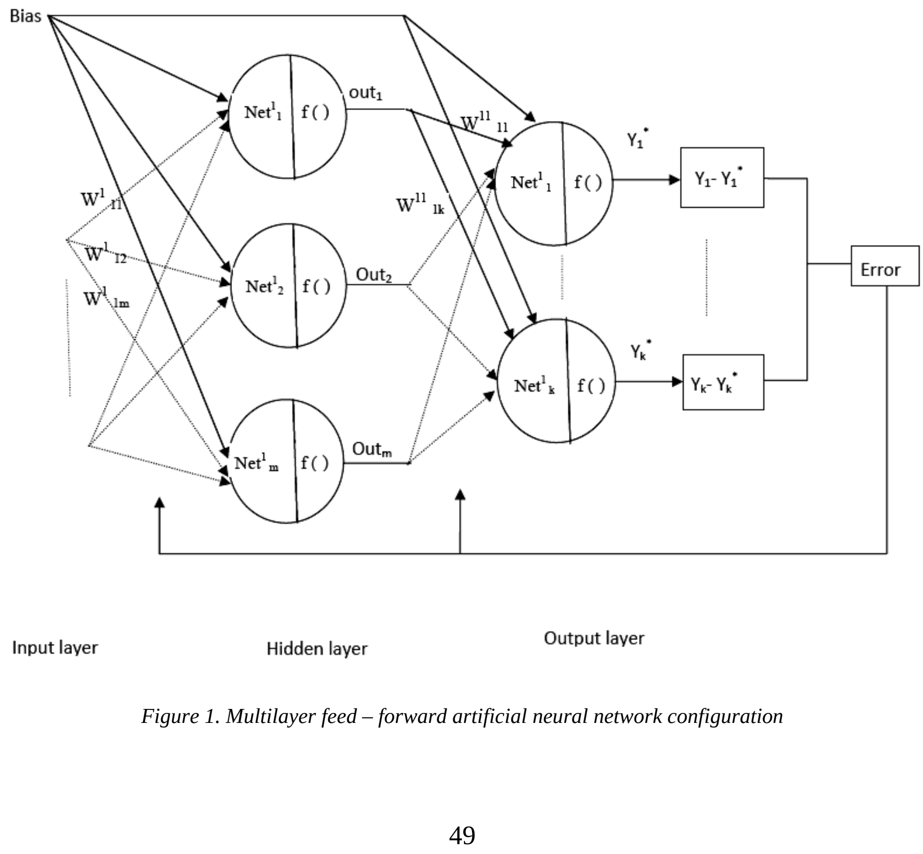

Figure 1. Multilayer feed – forward artificial neural network configuration

The theory of ANN has not been described here and can be found in many books such as Haykin (1994).

Study Area. In the present study the river stage-discharge modelling has been studied for *Godavari River* basin. The hydrological data observation station selected is Dhawalaishwaram Barrage site at Rajahmundry in Andhra Pradesh, India, where the flood prone effect will be seen as the flow contribution of all major tributaries almost completed with heavy inflows (Figure 2).

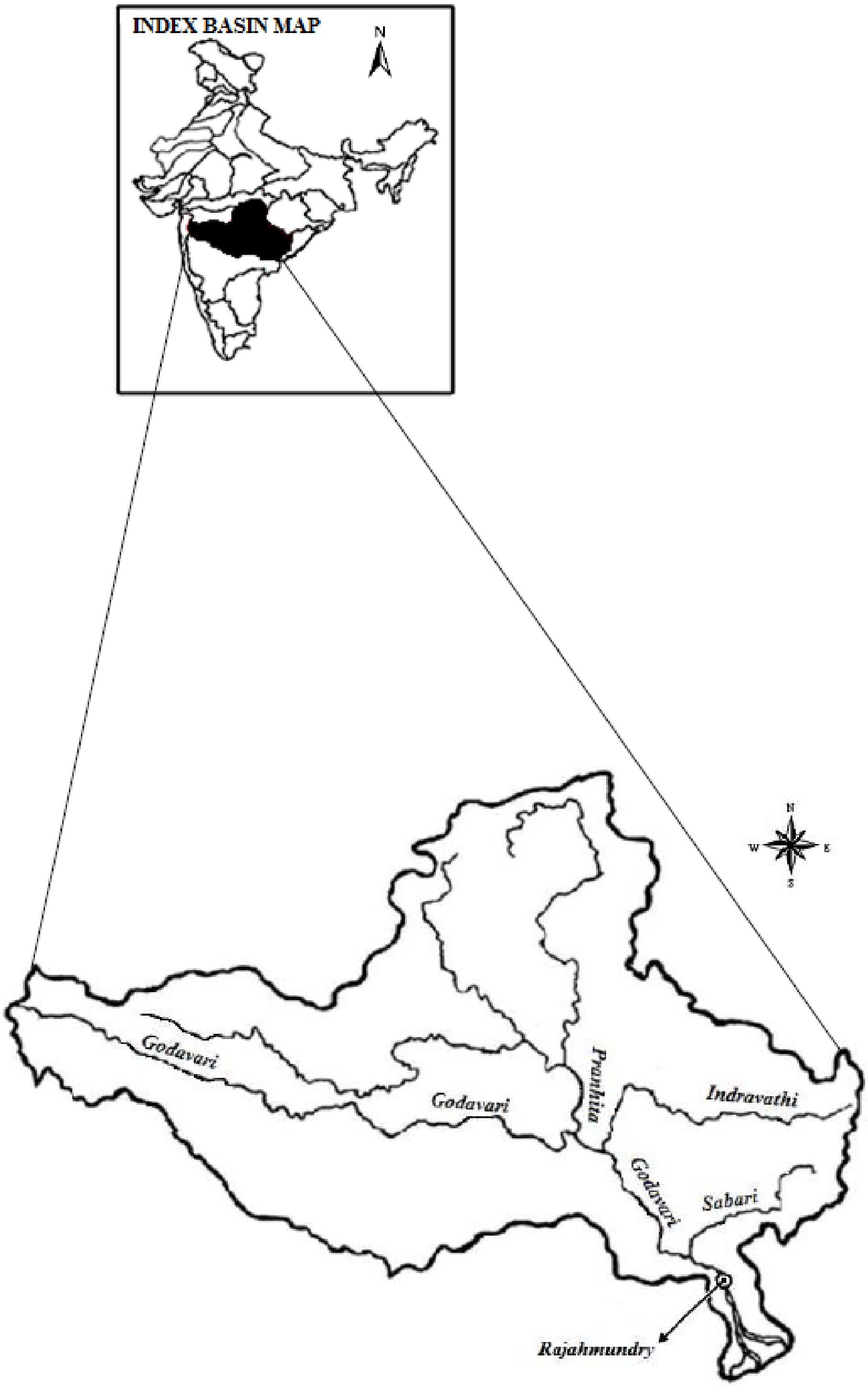

Figure 2. Hydrological study location Dhawalaishwaram Barrage site Rajahmundry, Andhra Pradesh, India

The hydrological data were collected from *Central Water Commission* (CWC), Govt. of India, Godavari circle at Hyderabad. The data consisted of river stage and discharge at Dhawalaishwaram Barrage site.

Methodology. NeuroIntelligence neural network software was used to apply neural networks to solve real-world forecasting, classification and function approximation problems.

Performance evaluation criteria. The statistical and hydrological evaluation criteria used in the present study are Mean Absolute Deviation (MAD), Root Mean Square Error (RMSE), Correlation Coefficient (R) and Coefficient of Efficiency (CE) or Coefficient of Determination (DC or R^2).

Mean Absolute Deviation (MAD). It is a measure of mean absolute deviation of the observed value from the estimated values. It has a unit and not a normalized criterion. It is expressed as, $MAD = \frac{\sum_{j=1}^{n} \left| Y_j - \hat{Y}_j \right|}{n}$, where, Y and $\hat{Y}$ are the observed and estimated values respectively and 'n' is the number of observations.

Root Mean Square Error (RMSE). It yields the residual error in terms of the mean square error expressed as $RMSE = \sqrt{\frac{residual\ variance}{n}} = \left(\sum_{j=1}^{n} (Y_j - \hat{Y}_j)^2 / n \right)^{1/2}$

Correlation Coefficient (R). It is expressed as $R = \frac{\sum_{j=1}^{n} \left\{ \left(Y_j - \overline{Y}\right)\left(\hat{Y}_j - \overline{\hat{Y}}\right) \right\}}{\left\{ \sum_{j=1}^{n} \left(Y_j - \overline{Y}\right)^2 \sum_{j=1}^{n} \left(\hat{Y}_j - \overline{\hat{Y}}\right)^2 \right\}^{1/2}}$,

where $\overline{Y}$ and $\overline{\hat{Y}}$ are mean of observed and estimated values.

Coefficient of Efficiency (R^2). Based on the standardization of residual variance with initial variance, the Coefficient of Efficiency can be used to compare the relative performance of the two approaches effectively (Nash and Sutcliffe, 1970). It is expressed as:

$$R^2 = \left\{ 1 - \frac{residual\ \ variance}{initial\ \ variance} \right\} = \left\{ 1 - \frac{\sum_{j=1}^{n} (Y_j - \hat{Y}_j)^2}{\sum_{j=1}^{n} (Y_j - \overline{Y})^2} \right\}.$$

The Coefficient of Efficiency is also commonly known as the Coefficient of Determination which may be written in a number of ways and represents the fraction of variance that is explained by regression. The closer this ratio is to unity, the better is the regression relation. It is possible to get a negative R-square for equations that do not contain a constant term. If R-square is defined as the proportion of variance explained by the fit, and if the fit is actually worse than just fitting a horizontal line, then R-square is negative. In this case, R-square cannot be interpreted as the square of a correlation.

While judging the acceptability of a model through above evolution criteria, the ability of each model must be properly understood. The mean absolute deviation and root mean square error are dimensional criteria reproducing an absolute error. The criteria can compare the performance of two models when the same data are used for their development. The correlation coefficient represents the degree of correlation between the observed and estimated values. Coefficient of efficiency compares the residual and initial variance and could vary depending upon the initial variance of observed data (Kachroo and Natale, 1992).

3. Development of Models

3.1. Ann River Stage-Discharge Models

The models are developed with river stage / river flow level (H) as input and river discharge (Q) as output for a major hydrological location on Godavari River at Rajahmundry (Dhawalaishwaram Barrage site) in Andhra Pradesh, India.

On the basis of correlation coefficient (R) and coefficient of efficiency (R^2) twenty models were selected for the training testing and validation. Out of which ten models selected for one hidden layer and remaining ten were for two hidden layers. The output discharge Q_t at time step t was mapped with river stage H_t with specified lag time i.e. H_{t-1}, H_{t-2}, H_{t-3} etc. and the previous discharge i.e. Q_{t-1}, Q_{t-2}, Q_{t-3} etc. Each model is trained tested and validated using the input data of the Godavari River. Five best models out of all the developed models were selected to represent the river-stage-discharge modelling of the study location with a view to predict and forecast the real time situation with a single parameter utilization possible.

Table1 describes the developed ANN models with input variables, output variable and number of hidden layers.

Table 1. Model Development of Various ANN River Stage-Discharge Models

Model	No. of hidden layers	Output	Input Variables
ANN – 1	One	Q_t	H_t
ANN – 2	One	Q_t	H_t, H_{t-1}
ANN – 3	One	Q_t	H_t, Qt-1
ANN – 4	One	Q_t	H_t, H_{t-1}, Q_{t-1}
ANN – 5	One	Q_t	H_t, H_{t-1}, H_{t-2}
ANN – 6	One	Q_t	H_t, H_{t-1}, H_{t-2},Q_{t-1}
ANN – 7	One	Q_t	H_t, H_{t-1}, H_{t-2},Q_{t-1},Q_{t-2}
ANN – 8	One	Q_t	H_t, H_{t-1}, H_{t-2},H_{t-3}
ANN – 9	One	Q_t	H_t, H_{t-1}, H_{t-2},H_{t-3}, Q_{t-1}, Q_{t-2}
ANN – 10	One	Q_t	H_t, H_{t-1}, H_{t-2}, H_{t-3}, Q_{t-1}, Q_{t-2}
ANN – 11	Two	Q_t	H_t
ANN – 12	Two	Q_t	H_t, H_{t-1}
ANN – 13	Two	Q_t	H_t, Qt-1
ANN – 14	Two	Q_t	H_t, H_{t-1}, Q_{t-1}
ANN – 15	Two	Q_t	H_t, H_{t-1}, H_{t-2}
ANN – 16	Two	Q_t	H_t, H_{t-1}, H_{t-2},Q_{t-1}
ANN – 17	Two	Q_t	H_t, H_{t-1}, H_{t-2},Q_{t-1},Q_{t-2}
ANN – 18	Two	Q_t	H_t, H_{t-1}, H_{t-2},H_{t-3}
ANN – 19	Two	Q_t	H_t, H_{t-1}, H_{t-2},H_{t-3}, Q_{t-1}, Q_{t-2}
ANN – 20	Two	Q_t	H_t, H_{t-1}, H_{t-2}, H_{t-3}, Q_{t-1}, Q_{t-2}

Note: Q = Discharge, H= River Stage

Table 2 describes the correlation coefficient, coefficient of efficiency for training, testing and validation of the data along with architecture and learning rate of different models.

Table 2. Best Stage-discharge ANN models for Dhawalaishwaram Barrage site, Godavari River (One hidden layer)

S. No.	Best Model	Architecture	Learning Rate	Training		Testing		Validation	
				R	R^2	R	R^2	R	R^2
1	ANN – 1	[1-6-1]	0.6	0.233	-24.705	0.214	-22.242	0.259	-17.187
2	ANN – 2	[2-1-1]	0.6	0.290	-11.130	0.250	-12.064	0.162	-17.650
3	ANN – 3	**[2-5-1]**	**0.6**	**0.924**	**0.810**	**0.950**	**0.881**	**0.920**	**0.822**
4	ANN – 4	**[3-4-1]**	**0.1**	**0.940**	**0.860**	**0.924**	**0.810**	**0.950**	**0.870**
5	ANN – 5	[3-3-1]	0.6	0.312	-18.051	0.280	-15.550	0.202	-19.056
6	ANN – 6	**[4-5-1]**	**0.6**	**0.940**	**0.854**	**0.930**	**0.820**	**0.932**	**0.856**
7	ANN – 7	**[5-11-1]**	**0.7**	**0.943**	**0.870**	**0.912**	**0.821**	**0.932**	**0.860**
8	ANN – 8	[4-1-1]	0.1	0.325	-9.950	0.222	-12.170	0.243	-11.470
9	**ANN – 9**	**[6-9-1]**	**0.6**	**0.940**	**0.861**	**0.925**	**0.834**	**0.960**	**0.900**
10	ANN – 10	[7-11-1]	0.1	0.937	0.855	0.933	0.834	0.910	0.821

Table 2 gives the tabulation of performance of the different models with one hidden layer. The performance indicators in throughout the study are Correlation Coefficient(R), Coefficient of Efficiency (R^2) and Root Mean Square Error (RMSE). Based on the Correlation Coefficient and Coefficient of Efficiency five models (i.e. models ANN-3, ANN-4, ANN-6, ANN-7 and ANN-9) are selected out of the ten models. Comparing R and R^2 of these models the model ANN-9 may be treated as the best model for one hidden layer.

Table 3 gives idea about the performance of the different framed models with two hidden layers. Out of ten developed models only six models (i.e. ANN-13, ANN-14, ANN-16, ANN-17, ANN-19 and ANN-20) have shown good generalization capability in respect of correlation coefficient and coefficient of efficiency. On the basis of higher values of correlation coefficient and coefficient of efficiency one best performing model i.e. model ANN-13 is selected for two hidden layers.

Table 3. Best Stage-discharge ANN models for Dhawalaishwaram Barrage site, Godavari River (Two hidden layer)

S. No.	Best Model	Architecture	Learning Rate	Training		Testing		Validation	
				R	R^2	R	R^2	R	R^2
1	ANN – 11	[1-8-3-1]	0.6	0.509	-2.234	0.501	-1.481	0.587	-2.202
2	ANN – 12	[2-2-8-1]	0.8	0.522	-1.788	0.469	-1.697	0.516	-3.282
3	**ANN – 13**	**[2-8-16-1]**	**0.6**	**0.946**	**0.881**	**0.936**	**0.869**	**0.959**	**0.907**
4	ANN – 14	**[3-8-12-1]**	**0.8**	**0.946**	**0.882**	**0.935**	**0.868**	**0.943**	**0.888**
5	ANN – 15	[3-6-11-1]	0.7	0.581	-1.044	0.314	-8.224	0.455	-7.140
6	**ANN – 16**	**[4-6-6-1]**	**0.8**	**0.946**	**0.881**	**0.921**	**0.823**	**0.948**	**0.879**
7	**ANN – 17**	**[5-5-5-1]**	**0.8**	**0.948**	**0.885**	**0.885**	**0.764**	**0.947**	**0.881**
8	ANN – 18	[4-4-4-1]	0.7	0.504	-3.746	0.537	-3.092	0.582	-3.655
9	ANN – 19	**[6-8-6-1]**	**0.6**	**0.949**	**0.888**	**0.940**	**0.848**	**0.939**	**0.838**
10	ANN – 20	[7-7-6-1]	0.6	0.943	0.870	0.927	0.850	0.921	0.836

According to RMSE, R and R^2 values of the best models for one hidden layer as well as for two hidden layers, only five best models having smaller RMSE values and greater values of R and R^2 are selected (see Table 4).

Table 4. Representative best Stage-discharge ANN models for Dhawalaishwaram Barrage site, Godavari River

S. No.	Best Model	Architecture	Learning Rate	Training			Testing		Validation	
				RMSE	R	R^2	R	R^2	R	R^2
1	ANN – 9	[6-9-1]	0.6	28657.820	0.940	0.861	0.925	0.834	0.960	0.900
2	ANN – 13	[2-8-16-1]	0.6	27147.410	0.946	0.881	0.936	0.869	0.959	0.907
3	ANN – 14	[3-8-12-1]	0.8	27816.083	0.946	0.882	0.935	0.868	0.943	0.888
4	ANN – 16	[4-6-6-1]	0.8	27661.600	0.946	0.881	0.921	0.823	0.948	0.879
5	ANN – 17	[5-5-5-1]	0.8	25770.627	0.948	0.885	0.885	0.764	0.947	0.881

For the selected best five models a comparative study has been done with graphical representation of observed and predicted data during training, testing and validation. For the same scattered plots are also drawn.

Figures from 3 to 7 present the details of the observed and estimated discharges and their corresponding scatter plots for the best fit ANN models to represent the stage-discharge modelling of the Godavari River during training, testing and validation.

Out of all the presented figures, Figures 4 (i.e. ANN-13) clearly give the information of the best fit modelling for the study location with Coefficient of Efficiency values 0.896, 0.877 and 0.919 during training, testing and validation respectively.

3.2. Development of Linear Multiple Regression Models

In developing Linear Multiple Regression (LMR) models, the River Discharge at time t, (Q_t), can be regressed against the River Stage and River Discharge in the past. The LMR models can be represented as follows $Q_t = \beta_0 + \beta_1 H_t + \beta_2 H_{t-1} + \beta_3 H_{t-2} + \beta_4 H_{t-3} + \beta_5 Q_{t-1} + \beta_6 Q_{t-2} + \beta_7 Q_{t-3}$,where β_i's represent the regression coefficients to be determined; H_i's represent the River Stage; Q_i's represent the Discharge; and t = index representing time.

The developed regression models description is as follows:

Model – LMR-1
$Q_t = 5468.10 + 632.871H_t + 0.847Q_{t-1}$;
Model – LMR-2
$Q_t = 6448.59 + 2988.57H_t – 2426.495H_{t-1} + 0.849Q_{t-1}$;
Model – LMR-3
$Q_t = 7152.94 + 3645.588H_t – 970.85H_{t-1} – 2159.02H_{t-2} + 0.849Q_{t-1}$;
Model – LMR-4
$Q_t = 5830.83 + 4016.82H_t – 835.42H_{t-1} – 2732.44H_{t-2} + 0.716Q_{t-1} + 0.157Q_{t-2}$;
Model – LMR-5
$Q_t = 6033.87 + 4090.09H_t – 604.17H_{t-1} – 2024.75H_{t-2} – 1123.0H_{t-3}+ 0.714Q_{t-1} + 0.158Q_{t-2}$.

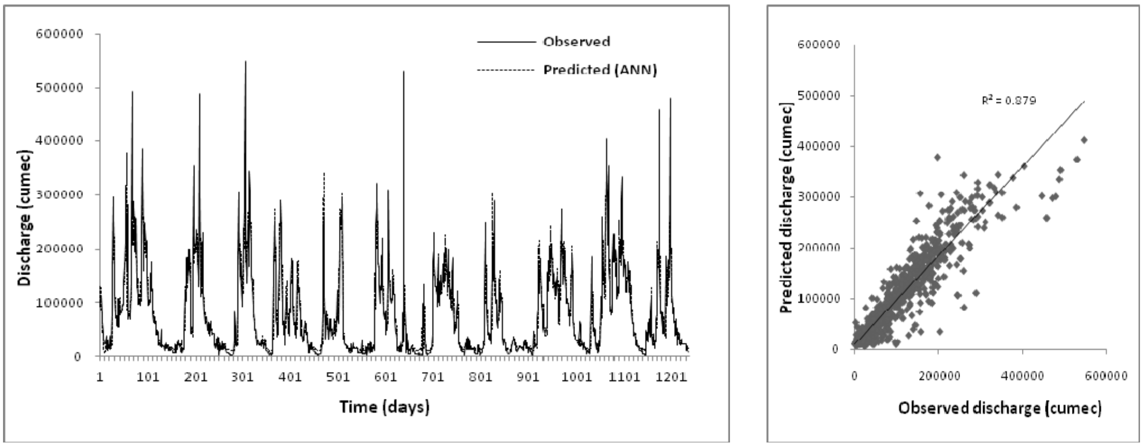

(a) Training

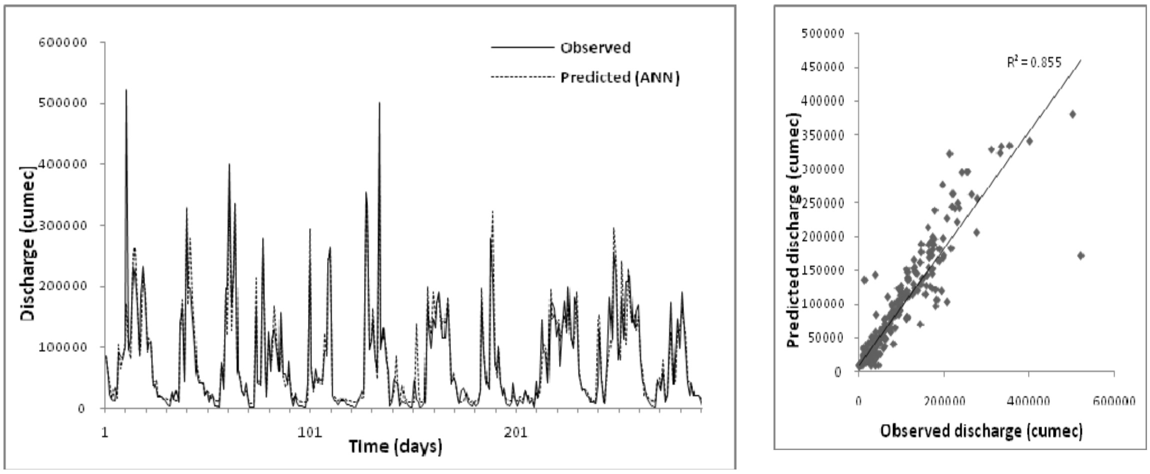

(b) Testing

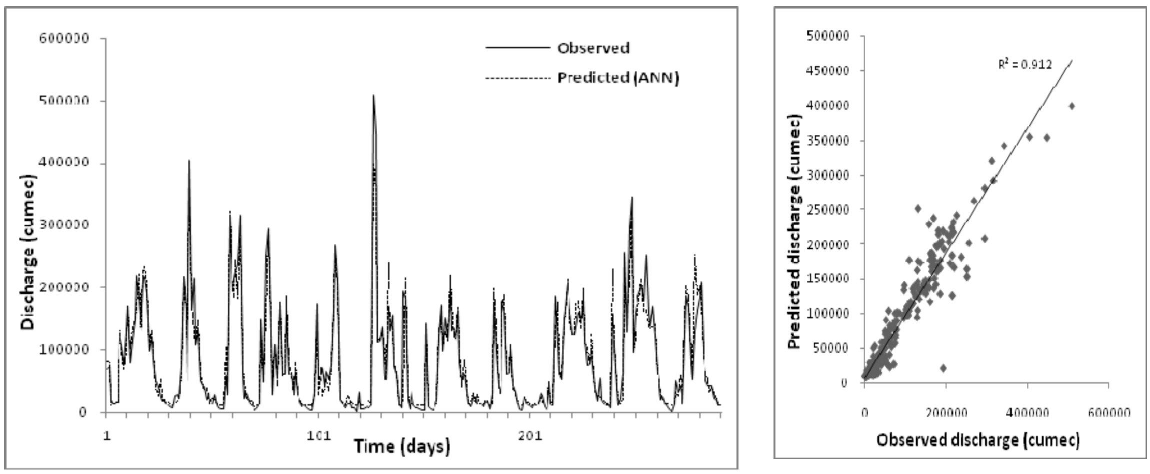

(c) Validation

Figure 3. Comparative plots of observed and predicted flows and their corresponding scatter plots for Dhawalaishwaram Barrage site, ANN-9

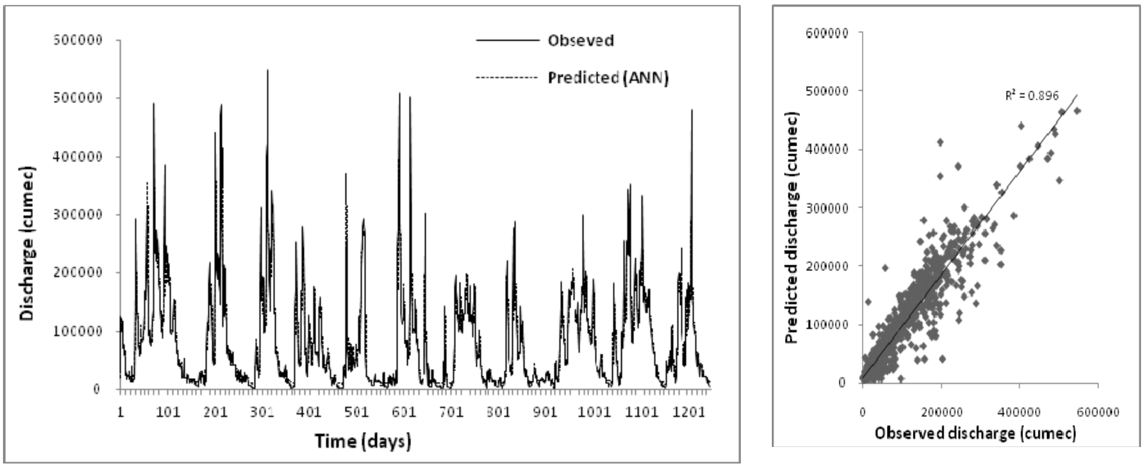

(a) Training

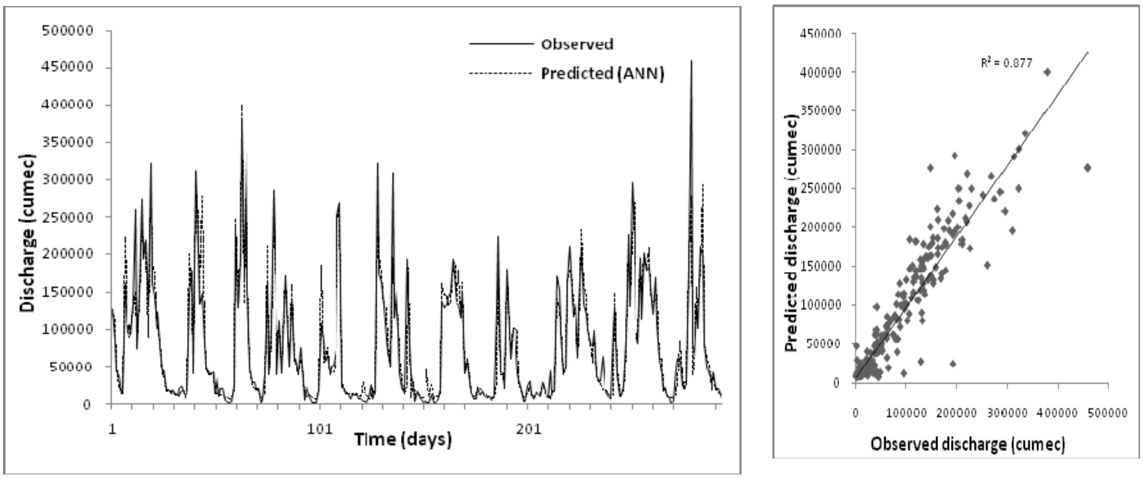

(b) Testing

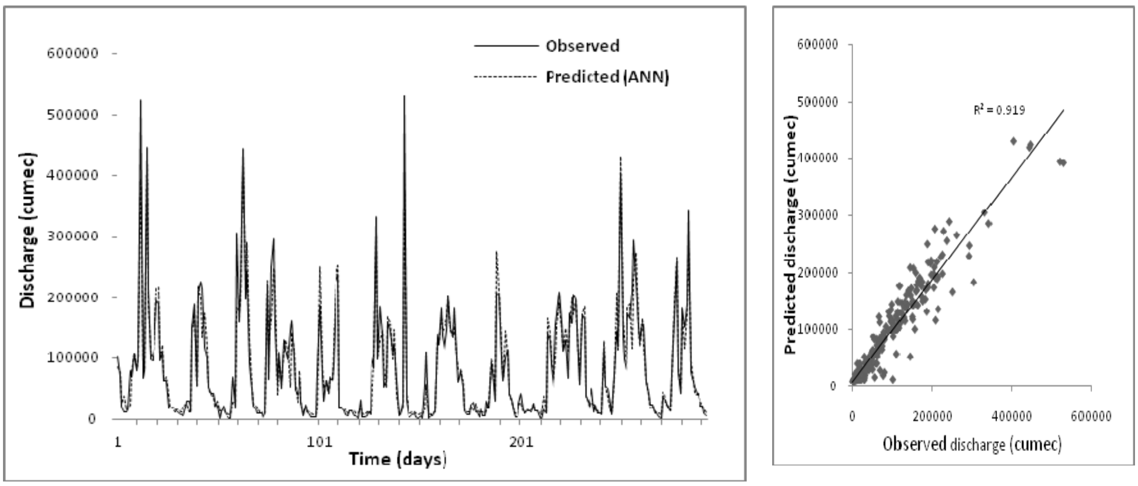

(c) Validation

Figure 4. Comparative plots of observed and predicted flows and their corresponding scatter plots for Dhawalaishwaram, model ANN-13

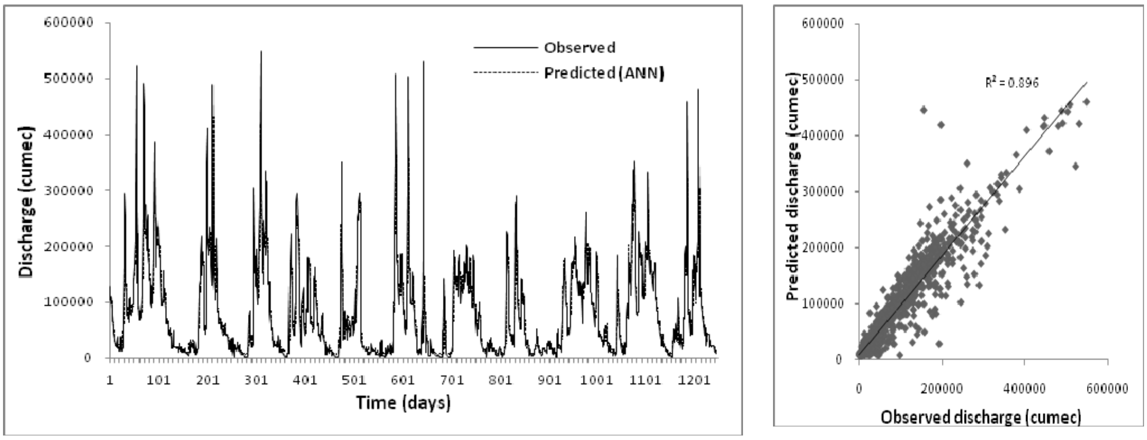

(a) Training

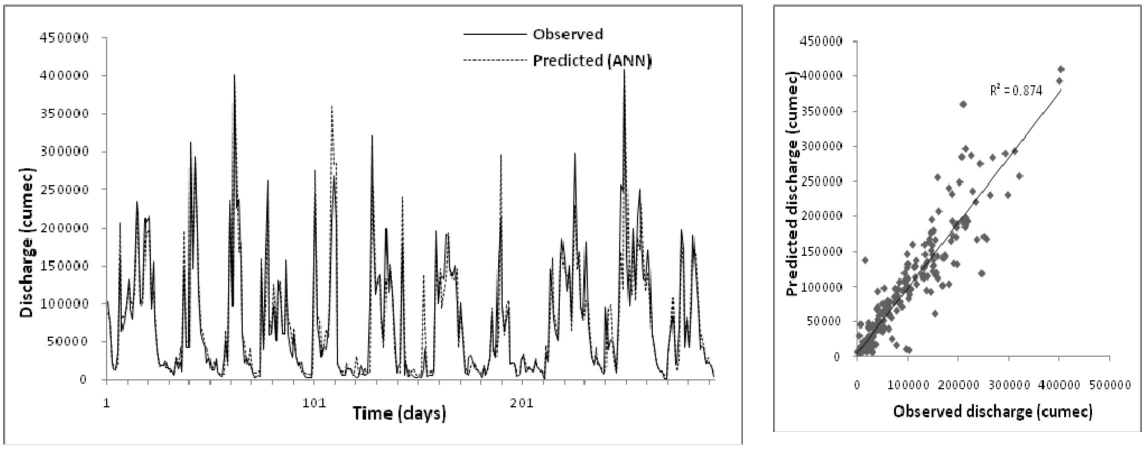

(b) Testing

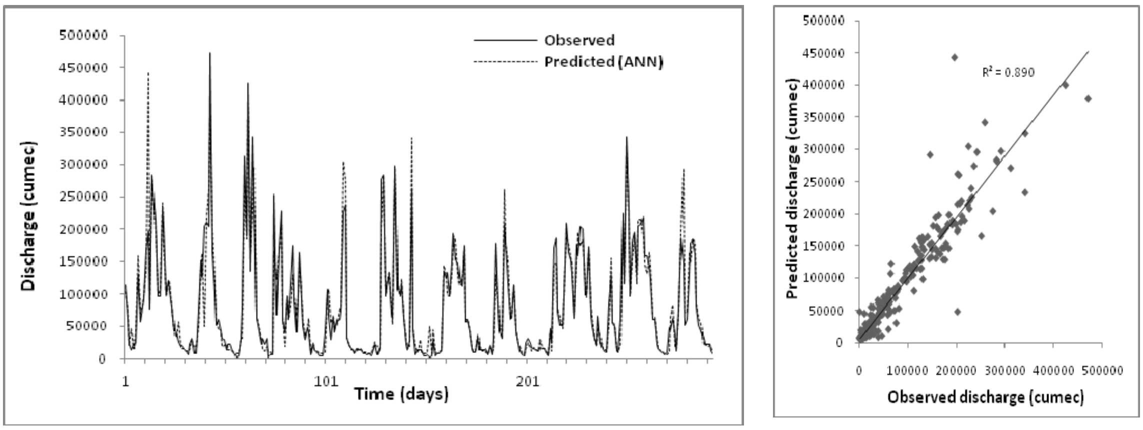

(c) Validation

Figure 5. Comparative plots of observed and predicted flows and their corresponding scatter plots for Dhawalaishwaram, model ANN-14

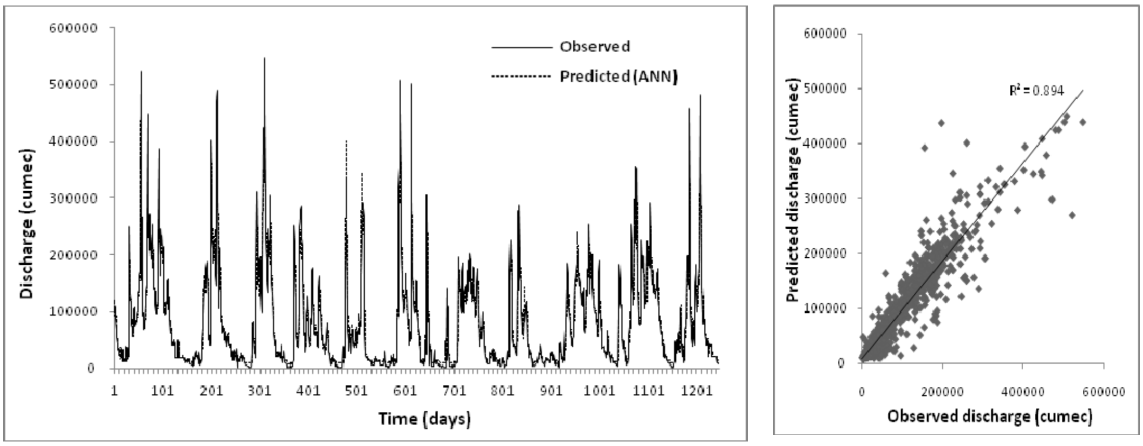

(a) Training

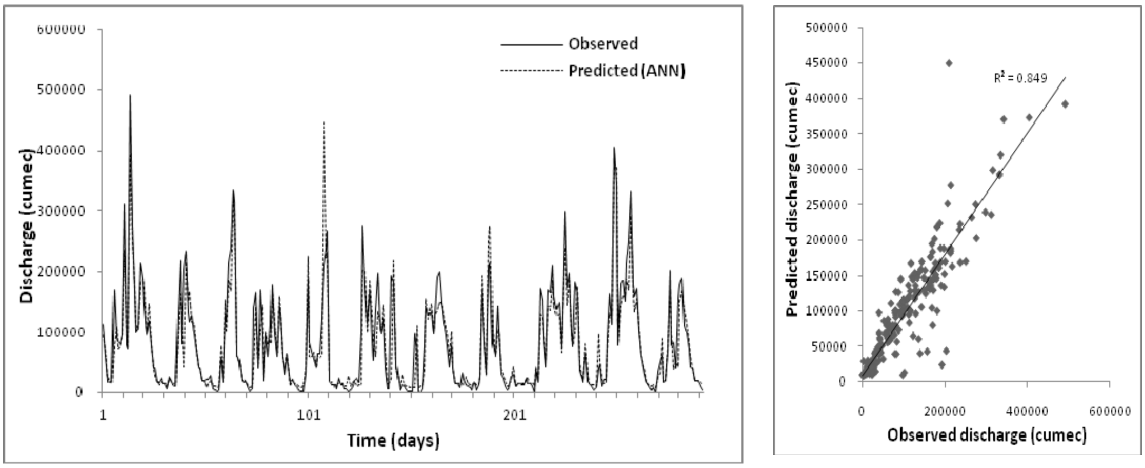

(b) Testing

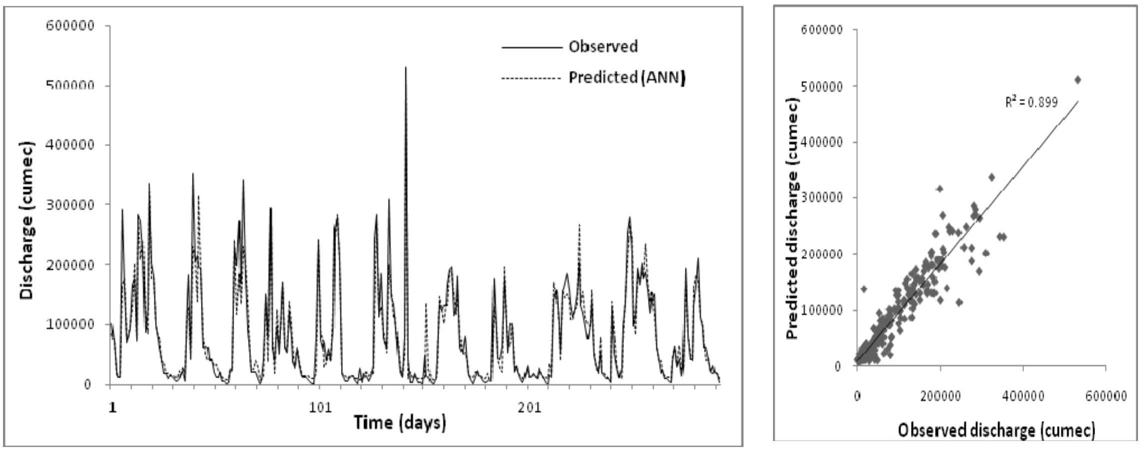

(c) Validation

Figure 6. Comparative plots of observed and predicted flows and their corresponding scatter plots for Dhawalaishwaram, model ANN-16

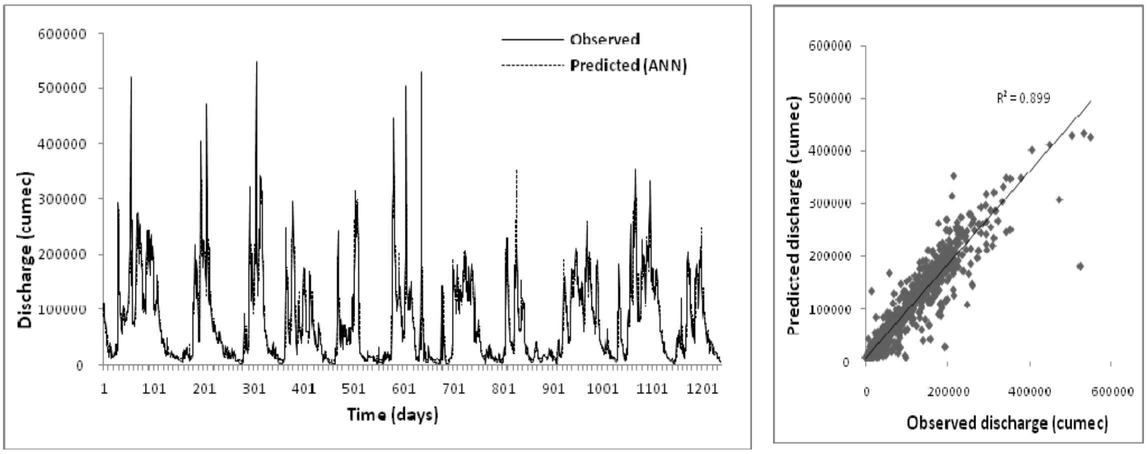

(a) Training

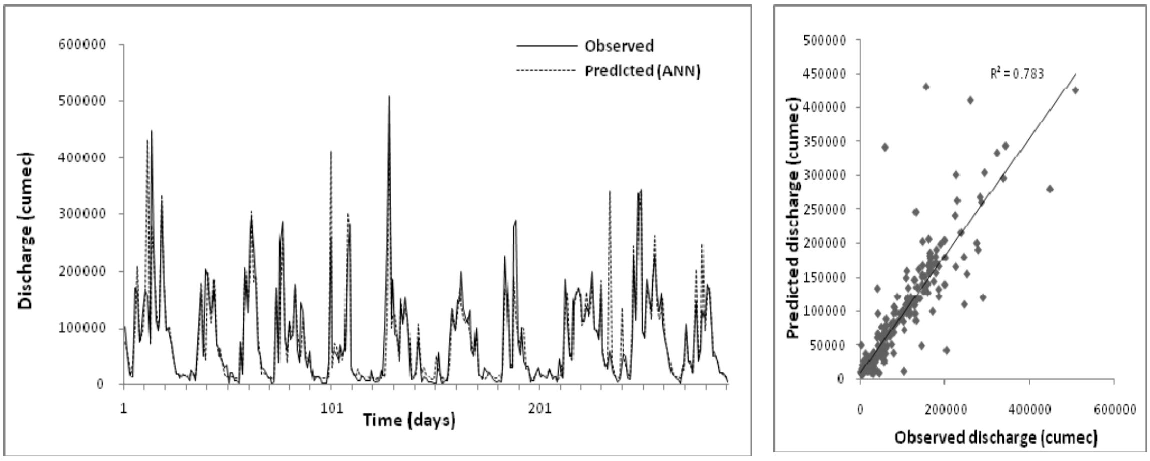

(b) Testing

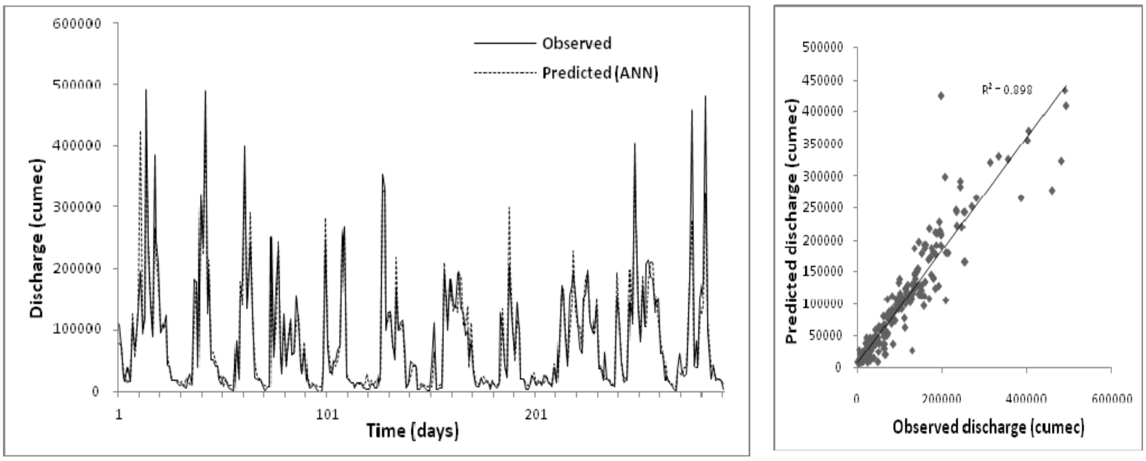

(c) Validation

Figure 7. Comparative plots of observed and predicted flows and their corresponding scatter plots for Dhawalaishwaram, model ANN-18

The graphical representation along with corresponding scattered plots of developed LMR models are shown on Figures 8 to 12.

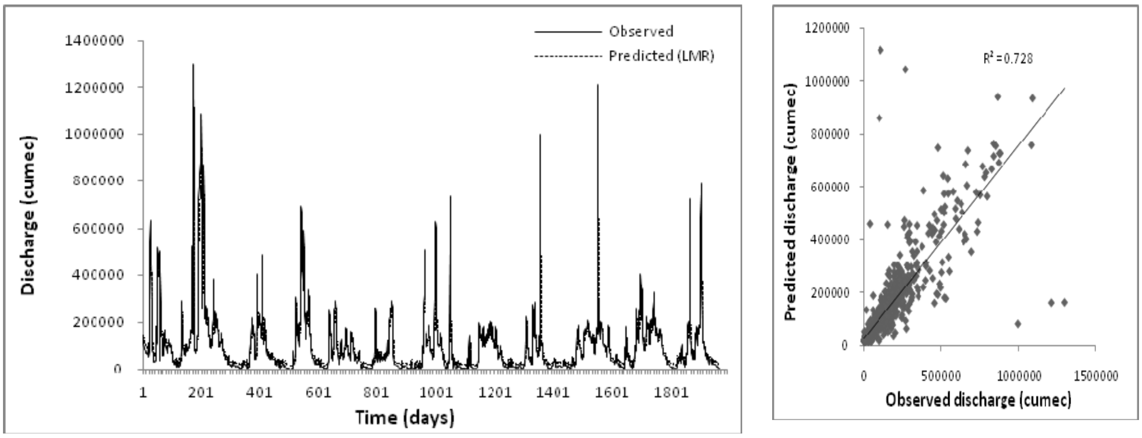

Figure 8. Comparative plots of observed and predicted flows and their corresponding scatter plots for Dhawalaishwaram, model LMR-1

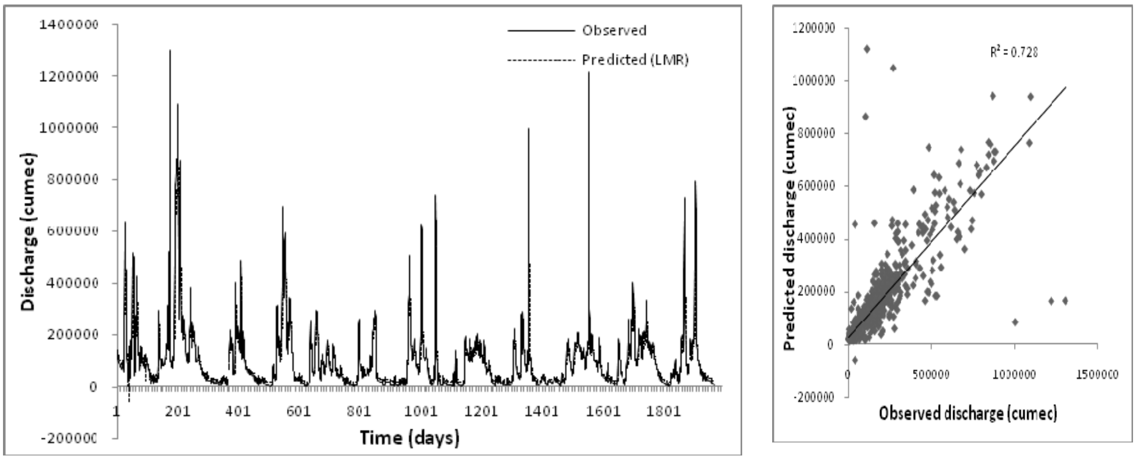

Figure 9. Comparative plots of observed and predicted flows and their corresponding scatter plots for Dhawalaishwaram, model LMR-2

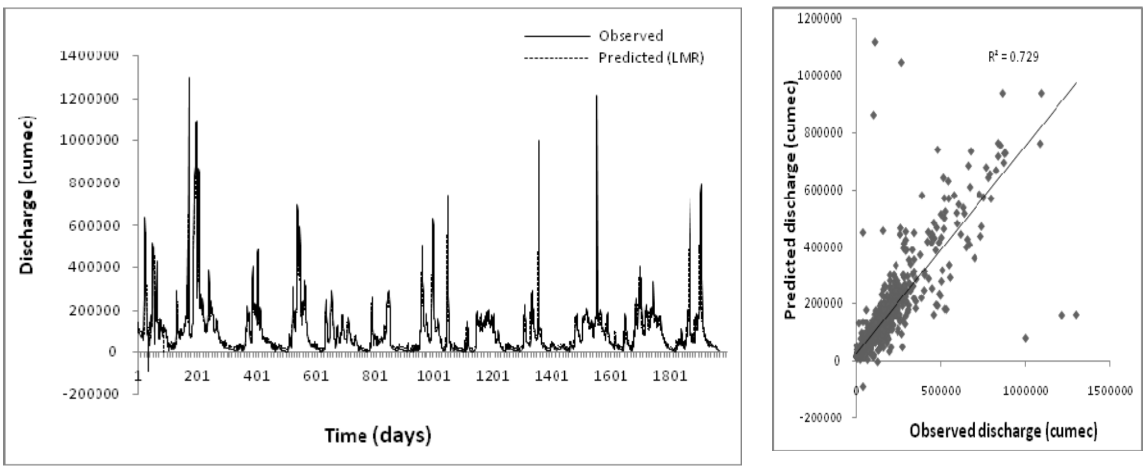

Figure 10. Comparative plots of observed and predicted flows and their corresponding scatter plots for Dhawalaishwaram, model LMR

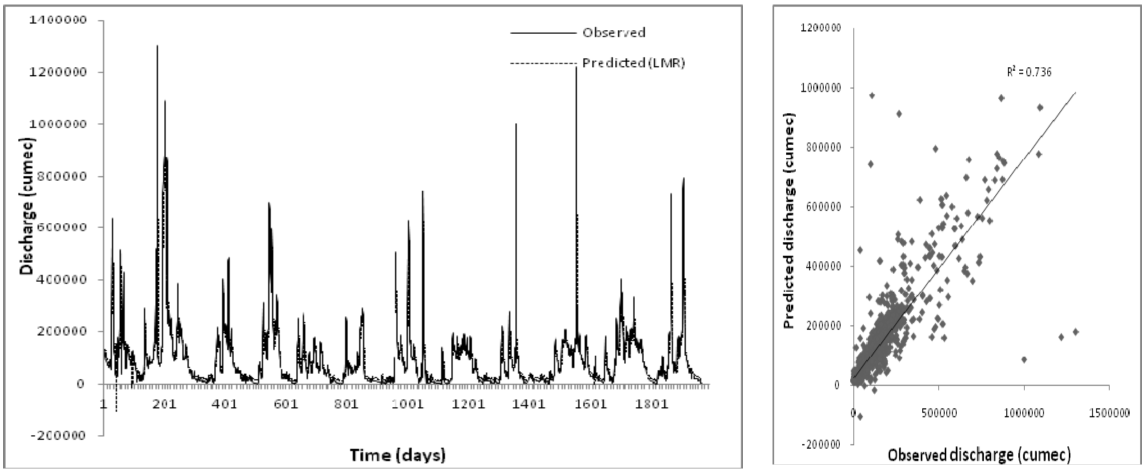

Figure 11. Comparative plots of observed and predicted flows and their corresponding scatter plots for Dhawalaishwaram, model LMR-4

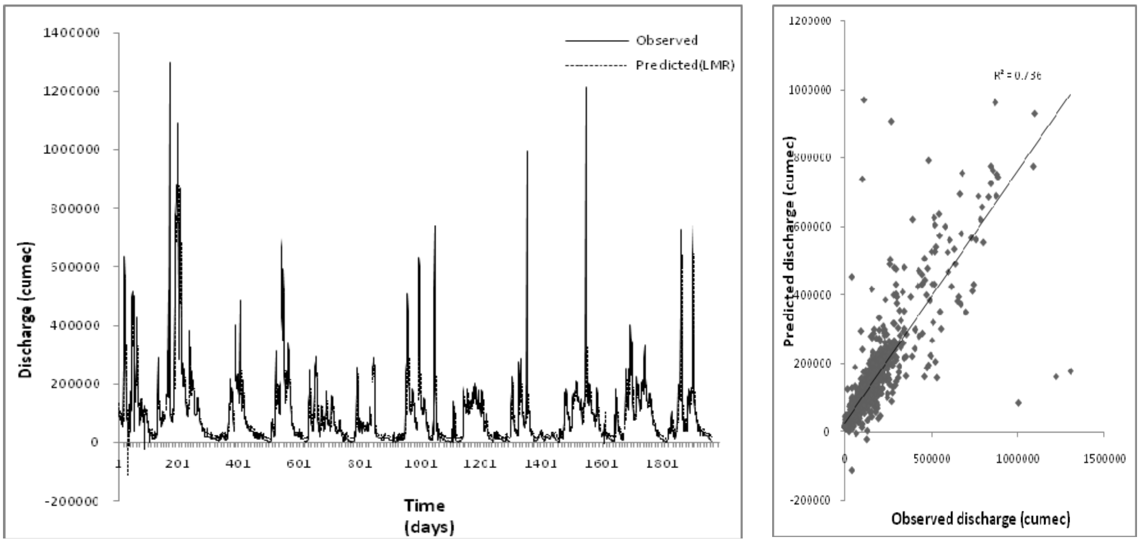

Figure 12. Comparative plots of observed and predicted flows and their corresponding scatter plots for Dhawalaishwaram, model LMR – 5

3.3. Comparison of Five Developed Best Stage-Discharge Ann Models with LMR Models

Table 5 gives comparison of performance of the best five ANN models with Linear Multiple Regression (LMR) models.

Table 5. Comparison of five best Stage-discharge ANN models with LMR models for Dhawalaishwaram Barrage site, Godavari River

S. No.	Model	MAD	R	R^2	RMSE
1	**ANN – 9**	15535.43	0.938	0.880	28674.17
2	**ANN – 13**	15097.49	0.947	0.897	27064.17
3	**ANN – 14**	15168.80	0.944	0.891	27819.76
4	**ANN – 16**	15579.27	0.942	0.890	28298.94
5	**ANN – 17**	14795.55	0.938	0.880	28821.87
6	**LMR – 1**	26694.78	0.853	0.728	69422.48
7	**LMR – 2**	26765.64	0.853	0.729	69311.67
8	**LMR – 3**	26801.61	0.854	0.730	69245.95
9	**LMR – 4**	27341.82	0.858	0.736	68389.09
10	**LMR – 5**	27407.36	0.858	0.736	68385.07

The performance indicators throughout the study are Mean Absolute Deviation (MAD) Correlation Coefficient(R), Coefficient of Efficiency (R^2) and Root Mean Square Error (RMSE). In the table 4.4 the Correlation Coefficient of ANN models varies from 93.8% to high as 94.7% for the mixed data (training, testing and validation), whereas Correlation Coefficient for LMR models varies 85.3% to as high as 85.8%. Coefficient of Efficiency for ANN models varies from 88% to as high as 89.7%, while the same for the LMR models varies from 72.8% to as high as 73.6%. Mean absolute deviation for the ANN models varies from 14795.55 to as high as 15579.27, whereas that for the LMR models varies from 26694.78 to as high as the 27407.36. Root mean square error for the five best ANN models varies from 27064.17 to as high as 28821.87, whereas that for the LMR models varies from 68385.07 to as high as 694522.48.

By the comparison made in Table 5 it is clear that performance of ANN models is better than LMR models for River Stage-Discharge.

Conclusions

With a clear idea of the above real time situation support, in the present study artificial neural network methodology was adopted to model the flow behaviour of the river system. The performance of the methodology was also evaluated to suggest readily available and accurate methodology for the simulation and forecasting of the problem. Neural Networks have shown better applicable performance and accuracy level for better system approach. The study suggests that Neural Network methodology is highly successful in the simulation and forecasting of the stage-discharge process.

Back-propagation algorithm is used in the design of ANN with learning rate range 0.6–0.8 and suggested best network architecture with the best parameter of the methodology. The statistical evolution criteria used in the development of ANN modelling was Correlation Coefficient (R), Coefficient of Efficiency (R^2). The results of the study have been found much closer to the observed process and the study shows the successful development of reliable relationship between the stage and discharge of river flow.

The study clearly reveals that the ANN models give better accuracy in prediction of discharge than the LMR models.

The study has explored only one application of the ANN approach in the hydrological modelling. Because of the flexibility and potential ANN methodology can also be successfully applied in the modelling of runoff, inflow forecasting, ground water fluctuation, evapotranspiration, sediment transportation, etc.

References

1. ASCE. Task Committee on Application of artificial neural networks in Hydrology. Artificial neural networks in Hydrology. II: Hydrologic Applications, *Journal of Hydrologic Engineering*, ASCE, Vol. 5 (2), 2000, pp. 124–137
2. Bhattacharya, B. and Solomatine, D. P. Application of artificial neural network in stage discharge relationship In: *Proceedings of the 4th Int. Conf. on Hydro-informatics.* Iowa, USA, 2000.
3. Cigizoglu, H. K. Estimation and forecasting of daily suspended sediment data by multilayer perceptrons, *Adv. Water Resour.*, Vol. 27, 2004, pp. 185–195.
4. Davies, T. R. and Hall, R. J. A realistic strategy for disaster prevention. In: *Proceedings of the Conference, Interpravent, Bern, Switzerland*, 1992, pp. 381–390.
5. Dawson, C. W. and Wilby, R. An artificial neural network approach to rainfall-runoff modelling, *Hydrological Sci. J*., Vol. 43 (1), 1998, pp. 47–66.
6. Dibike, Y. B. and Solomatine, D. P. River Flow Forecasting Using ANNs, *Journal of Physics and Chemistry of the Earth, Part B: Hydrology, Oceans and Atmosphere*, Vol. 26 (1), 2001, pp. 1–8.
7. Haykin, S. Neural Networks – a Comprehensive Foundation. New York: Macmillan, 1994.
8. Jain, S. K. Development of integrated sediment rating curves using ANNs. *Journal of Hydraulic Engineering,* ASCE, Vol. 127 (1), 2001, pp. 30–37.
9. Jain, S. K. and Chalisgaonkar, D. Setting up stage-discharge relations using ANN, *J. of Hydrologic Eng.*, ASCE, Vol. 5 (4), 2000, pp. 428–433.
10. Kachroo, R. K. and Natale, L. Non-linear modelling of the rainfall-runoff transformation, *Journal of Hydrology,* Vol. 135, 1992, pp. 341–369.
11. Kisi, O. Multi-layer perceptrons with Levenberg-Marquardt optimization algorithm for suspended sediment concentration prediction and estimation, *Hydrol. Sci. J.*, Vol. 49 (6), 2004, pp. 1025–1040.

12. Kisi, O. Development of streamflow-suspended sediment rating curve using a range dependent neural network, *International Journal of Science and Technology*, Vol. 2 (1), 2007, pp. 49–56.
13. Lin, B., and Namin, M. M. Modelling suspended sediment transport using an integrated numerical and ANNs model, *J. Hydraul. Res.*, Vol. 43 (3), 2005, pp. 302–310.
14. Lohani, A. K., Goel, N. K. and Bhatia, K. K. S. Deriving stage-discharge-sediment concentration relationships using fuzzy logic. *Hydrological Sciences Journal*, Vol. 52 (4), 2007, pp. 793–807.
15. Muttiah, R. S., Srinivasan, R., Allen, P. M. Prediction on two – year peak stream discharges using neural networks, *Journal of the American Water Resources Association*, Vol. 33 (3), 1997, pp. 625–630.
16. Nagy, H. M., Watanabe, B., Hirano, M. Prediction of sediment load concentration in rivers using artificial neural network model, *J. Hydraul. Engineering*, ASCE, Vol. 128 (6), 2002, pp. 588–595.
17. Nash, J. E. and Sutcliffe, J. V. River flow forecasting through conceptual models, *Journal of Hydrology*, Vol. 10 (3), 1970, pp. 282–290.
18. Rai, R. K. and Mathur, B. S. Event-based sediment yield modelling using artificial neural network, *Water Resources Management*, 22 (4), 2008, pp. 423–441.
19. Rumelhart, D. E., Hinton, G. E. and Williams, R. J. Learning internal representations by error propagation. In: *Parallel Distributed Processing. Vol. I.* Cambridge, Mass.: MIT Press, 1986, pp. 318–362.
20. Tayfur, G. Artificial neural networks for sheet sediment transport, *Hyrol. Sci. J.*, Vol. 47 (6), 2002, pp. 879–892.
21. Tayfur, G. and Guldal, V. Artificial neural networks for estimating daily total suspended sediment in natural streams, *Nordic Hydrol.*, Vol. 37 (1), 2006, pp. 69–79.
22. Webros, P. J. *Beyond Regression: new tools for prediction and analysis in behaviour sciences: PhD Thesis.* Harvard University, Cambridge, 1974.

Received on the 12th of May, 2010

Computer Modelling and New Technologies, 2010, Vol.14, No.3, 63–67
Transport and Telecommunication Institute, Lomonosova 1, LV-1019, Riga, Latvia

FINANCIAL TIME SERIES PREDICTION WITH THE TECHNOLOGY OF COMPLEX MARKOV CHAINS

V. Soloviev[1], V. Saptsin[2], D. Chabanenko[3]

[1, 3]Cherkassy National University, Cherkassy, Ukraine
[2]Kremenchuk State University, Kremenchuck, Ukraine
vnsoloviev@rambler.ru[1], saptsin@sat.poltava.ua[2], chdn6026@mail.ru[3]

In this research the technology of complex Markov chains, i.e. Markov chains with a memory is applied to forecast financial time-series. The main distinction of complex or high-order Markov chains [1] and simple first-order ones is the existing of after effect or memory. The high-order Markov chains can be simplified to first-order ones by generalizing the states in Markov chains. Considering the "generalized state" as the sequence of states makes a possibility to model high-order Markov chains like first-order ones. The adaptive method of defining the states is proposed, it is concerned with the statistic properties of price returns [2]. According to the fundamental principles of quantum measurement theories, the measurement procedure impacts not only on the result of the measurement, but also on the state of the measured system, and the behaviour of this system in the future remains undefined, despite of the precision of the measurement. This statement, in our opinion, is general and is true not only for physical systems, but to any complex systems [3].

Keywords: *high-order Markov chains, financial time-series*

1. Introduction

Nonlinear systems, in which future states depends on infinite past states are being analysed. The analysis of above-mentioned systems is possible only in discrete and finite representation, and results of it will be initially and principally approximate, i.e. it contains endogenous uncertainty, which inherits from current system according to the quantum postulates.

With the chosen time discretization, the memory-based model can be described in the following way:

$$x(n+1) = f\left(x(n); x(n-1); x(n-2)...\right). \quad (1)$$

It's necessary to mention, that with the continuing time definition the dynamical behaviour of the memory-based model is unable to be represented with some trajectory on the finite-dimensional phase space.

In order to quantify uncertainties in real complex socio-economical systems the probabilistic models are used. However, the usage of probabilistic models is based on the controversial hypotheses, so statistical interpretation of the results is not informative enough, and its results are not corresponding to the real systemic processes. In particular, the $1/f$-noise problem [4] is widely connected with the existence of long memory in complex systems. From the statistic's point of view it means the absence of the mean value in time series as a limit, when the time window approaches infinity, for any processes in complex systems. So such processes cannot be statistically explained [2].

2. Modern Conceptions in Complex System's Modelling

The new approaches in complex system's dynamics simulation and prediction are based on the usage of determined chaos and neural-networks technologies [5–7]. The exploration and realization became possible only with appearance of powerful modern computers. The common feature of these technologies is a usage of recurrent computational process:

$$x_{n+1} = f_n\left(f_{n-1}\left(...\left(f_1\left(x_1\right)...\right)\right)\right), \quad n = 1, 2, ..., \quad (2)$$

where $f_i(x_i)$ is nonlinear mapping for vector x_i, i is a discrete or real or modelled time. To identify the model (2) means to define parameters of nonlinear function $f_i(x_i)$, the distinctions between determined chaos and neural networks models connected with the type of the function and parameter estimation methods. Convergence of the process (2) in general is not required. In general case a function can take either single-moment vector component's values x_i, or dynamics it's changes in time.

It is possible to convert a particular model (1) to the type of more general model (2) with the help of lag variables addition into the model (1).

Both deterministic (described by integro-differential equations) and stochastic processes (complex Markov chains [1] belongs to it), can be reviewed as particular cases of the determined chaos models of type (2). With time discretization Δt approaches zero, if such a limit exists, the model converges to classical integro-differential equations. With finite Δt it is models with discrete time, which can generate future value's sets in corresponding phase space, also including lag variables. These sets can be either measurable (discrete or continuous) sets, that accept probabilistic interpretation, or immeasurable sets – fractals [8], for which such an interpretation is in principle unacceptable.

The prominent examples for determined chaos models, acceptable for probabilistic interpretation, are different pseudo random-number generators, which are widely used in simulation modelling. It's necessary to mention, that no exact procedures exist, which can differentiate "real" random sequence from pseudo-random one. Indeed, any finite "random" sequence definitionally is not random because of its finiteness, and any "non-random" finite sequence may be regarded as one of the possible, but very rare, subsets from real infinite random sequence.

Discrete Markov process $X(t)$ of order $r \geq 1$ with discrete time t, (the Complex Markov chain of order $r \geq 1$), is defined as conditional probability [1]:

$$p(x_s,t_s/x_{s-r};\ ..,x_{s-1},t_{s-1}) = p(x_s,t_s/x_1,t_1;..,\ x_{s-1},\ t_{s-1}). \qquad (3)$$

This condition should be fulfilled for any discrete moments of time $t_1 < t_2 < \ldots < t_r < t_s$. (the tuple (x_i,t_i) is considered as a state ($X(t_i) = x_i$). Both simple Markov chain ($r = 1$), and Complex Markov chain ($r > 1$) is defined by the distribution of transition probabilities $p(x_s,t_s/x_{s-r};\ ..,x_{s-1},t_{s-1})$ (the conditional probability). This distribution depends on r last states and the distribution of r-th state (unconditional probability):

$$p(x_{s-r}\ \ldots,x_{s-1},t_{s-1}) = P\{(X(t_{s-r}) = x_{s-r}),\ \ldots(X(t_{s-1}) = x_{s-1})\}, \qquad (4)$$

where time moments $t_1, t_2, \ldots t_s$ are regarded as discrete integer parameters.

The main distinction of complex high-order Markov chains from simply first order ones is the existence of the after-effect (memory), because the future state of the system (x_p, t_p) depends not only on the current state (x_q, t_q) (simple Markov chain), but also on sequence of $r - 1$ past states (x_{q-r+1}, t_{q-r+1};…x_{q-1}, t_{q-1}), $t_{q-r+1} < \ldots < t_{q-1} < t_q < t_p$ in the complex Markov chain. We can simplify the complex Markov chains of order r to simple ones (of order $r = 1$) by generalizing the state of the system. We consider the "general state" as the sequence of r past states [2].

The technology, which is proposed in the current work, is similar to neural-networks and is based on the following terms:

1. The process has an after-effect and is generated by some "hidden" model of determined chaos. Classical random and determined processes are regarded as partial cases of more general model.
2. Input data for a model of prediction is only the discrete points of researched value of the system. The time interval of the discretization is constant. This data definitionally is finite and therefore is restricted.
3. We use the quantized discrete relative differential of the input time series. This differentials are counted with certain time steps, that is congruous to the input time-series discretization time interval (The input discretization time interval is considers a unity time interval).
4. The conditional probabilities of the one-step transitions are counted, considering the Markov chain is stationary at the given time-series.
5. We take the difference with the maximum likelihood at the each step as a prediction, and at the next step we consider this probability equals to unity (process is considered as determined one).

6. The optimal choice of hierarchy of time discretization and the parameters for each discretization time interval (Markov chains order, or memory length, the number and the characteristics of states in the Markov chain) is evaluated with the genetic and learning approach, similarly to neural-networks technologies.

The terms 1–6 should be regarded as conditions, we can prove it only in the set of the experimental researches. Really this postulates a new procedure of indirect measurement, which is based on the current discretized input time-series, the result of this measurement is the prediction as the one of the possible scenarios of the system behaviour in the future (the sequence or the vector of predicted time series).

Conceptually this approach may be proved by some analogy with the properties and dynamic and behaviour of the quantum-mechanical systems.

3. The Prediction Algorithm

The prediction algorithm consists of the following steps.

1. Evaluation the set of time discretization intervals ($t_{\min} \leq t \leq t_{\max}$), relating to the hierarchy of time steps $\Delta t = 1, 2, 4, 8, 16, 32 \ldots \Delta t_{\max}$, $\Delta t_{\max} = 2^k$, or more complex hierarchies.
2. Chose the number of quantized levels s for the differences (i.e. the number of elementary states for Markov chains) and coding (discretizing) the differences for every Δt, optimising the distribution between the states to be uniform.
3. For every discretization time interval Δt and number of quantized states s we estimate the transition probabilities between the states for Markov chains of order $r = 1, 2, 3, 4, \ldots$ and evaluation of transition probability matrices.
4. Doing a prediction for triple ($\Delta t, r, s$) and for the last state t_{beg}, $t_{\text{beg}} \leq t_{max}$-$\Delta t$ using the state with maximum probability at each step.
5. Recurrent conjunction of prediction series of different discretization time intervals Δt in a single time-series.
6. Estimate the optimal parameter values s and r for every Δt.
7. Doing a final prediction using above-mentioned procedures and optimal parameters s and r, estimated at step 6.
8. Conjunction of resulting time-series with a zero order Markov chain series. We consider linear trend with sine as the zero-order series (the function $y = ax + b + \sum_{i=1}^{n} \left(c_i \sin(d_i x + e_i) \right)$). The coefficients of this function are estimated by nonlinear least squares method.

4. Experimental Results and Algorithm Testing

Based on above-mentioned algorithm, the computer program is created in Matlab environment. Parameters of Complex Markov chains were automatically estimated through experiments on learning data set. The discretization time step hierarchies $\{\Delta t_i\}$ of two types are used. The simple one is similar to discrete Fourier transform and is a set of $\Delta t_i = 2^i$ and the complex one is a natural number's powers productions $\Delta t_i = \prod_{i=1}^{n} p_i^{s_i}$ and has more wide net of time steps. The time discretizations hierarchy gives a possibility to review long-memory properties of the series without increasing the order of the Markov chains, to make prediction on the different frequencies of the series.

The algorithm was tested on the following time series:

1) on regular dependences of type:

$$x_n = a \sin(bn) \cdot \exp(-dn) + c; \quad n = 1, 2, \ldots , \tag{5}$$

(discrete sin oscillations with different frequencies, time discretizations, with exponential fade out and without it) (see Figures 1 and 2);

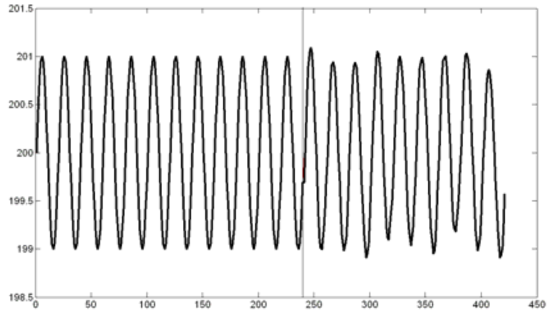

Figure 1. Prediction of a function $y = \sin\left(\frac{2\pi}{20}t\right)$ with parameters $k = 5, s = 9$

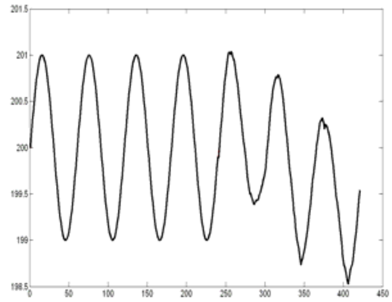

Figure 2. Prediction of a function $y = \sin\left(\frac{2\pi}{60}t\right)$ with parameters $k = 2$, $s = 9$

2) on time series, generated by discrete model "Predator-Prey":

$$\begin{cases} x_{n+1} = x_n\left(1+\alpha\left(1-x_n-y_n\right)\right); \\ y_{n+1} = y_n\left(1-\gamma+\beta x_n\right) \end{cases} \tag{6}$$

with parameter values $\alpha = 3{,}55$; $\beta = 2{,}1623$; $\gamma = 0{,}8$, which causes likely chaotic regime (see Figures 3 and 4);

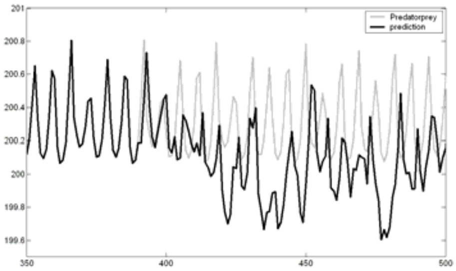

Figure 3. Prediction of the series from "Predator-Pray" model, $s = 5$

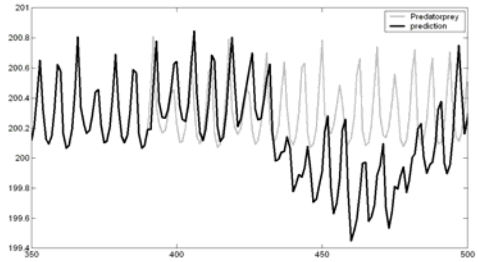

Figure 4. Prediction of the series from "Predator-Pray" model, $s = \sqrt{\Delta t}$

3) on real financial time series including EUR/USD Forex course, the World's stock's indices, including Dow Jones, S & P 500, DAX, FTSE, RTS, PFTS and others (see Figures 5 and 6).

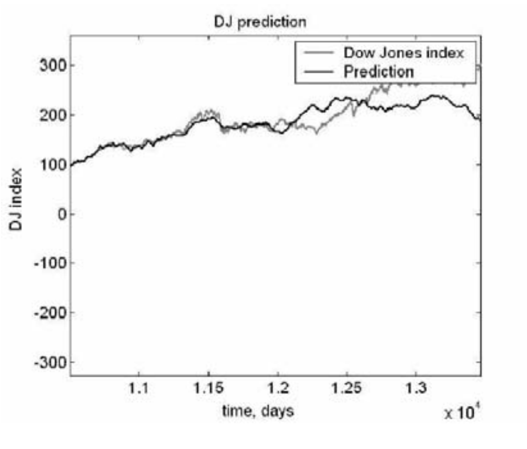

Figure 5. Prediction of Dow Jones index (1940–1953)

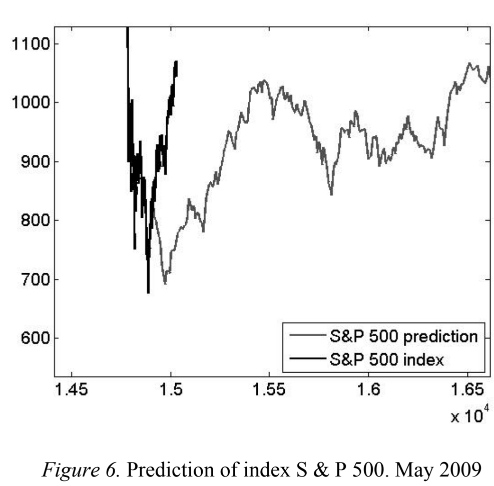

Figure 6. Prediction of index S & P 500. May 2009

Conclusions

The results of experiments and its analysis give possibilities to make the following conclusions.

1. Replacing the initial time series with its first value and a quantized differences sequence (straight procedure) causes losses in precision because of quantification errors and its cumulating while difference summarizing in inverse transformation procedure. However surplus data representation with time discretization hierarchy and inverse transform procedure can essentially reduce quantification errors. For sine (and all periodical) oscillations the reasons of errors are discretization time step's incoherence with oscillation periods Δt , which causes "pulsation" effects.
2. The prediction quality increases with Markov chain's order *r*, however while learning set's length is limited, the quality growth is also limited. It is probably caused:
   - by reducing the number of chains, for every transition probability and increasing a correlation between them (what is equivalent of it's number reducing because of averaging procedure);
   - by chain identification of error number increasing, because of definitely approximate character of state quantification and chain's identification.
3. It's possible to generate two or more possible scenarios, while probability distribution has two similar mode values. The corresponding fork points at the predicted curve can be regarded as possible process bifurcation points.
4. For "Predator-Prey" models a prediction with Markov chain's order $r=2$ causes better quality, than a prediction with $r = 3$, what can be explained by model's simplicity and absence of "long" memory (value of x_{n+1} is determined by the values x_n and x_{n-1}). In this case increasing of *r* does not cause prediction quality to increase, but it can cause the influence of negative factors, described in 2).

The new prediction technology, similar to neural-network ones is proposed for complex financial system's simulation. The algorithm and its program realization was developed and tested on artificial and real time series. The prediction results for stock indices S & P 500, DAX, FTSE are reviewed. The results demonstrate the algorithm's ability to predict financial time series and prospect of further researches in the proposed field.

References

1. Tikhonov, V. I., Mironov, V. A. *Markov processes.* Moscow: Soviet Radio, 1977. 488 p.
2. Saptsin, V. Experience of application genetically complex Markov chains for neural networks technology prediction*, Visnyk Krivoriz`kogo ekonomichnogo institutu KNEU, Kriviy Rig,* 2009, Vol. 2 (18), pp. 56–66.
3. Saptsin, V., Soloviev, V. Relativistic quantum econophysics – new paradigms in complex systems modeling, *arXiv: physics/0907.1142* [physics.soc-ph], 7 Jul 2009.
4. Bookinham, M. *Noises in electronic devices and systems.* Moscow: Mir, 1986.
5. Wasserman, P. D. *Neural computing: theory and practice*. New York: Van Nostrand Reinhold, 1989.
6. Surovcev, I. S., Klyukin, V. I., Pivovarova, R. P. *Neural networks*. Voronezh: VGU, 1994. (In Russian).
7. Ezhov, A. A., Shumskiy, S. A., *Neurocomputing and his applications in an economy and business*. Moscow: MIFI, 1998. (In Russian).
8. Mandelbrot, B. *The fractal geometry of nature.* San Francisco: Freeman, 1982.
9. Rabiner, R. L. A Tutorial on Hidden Markov Models and Selected Applications in Speech Recognition, *Proceedings of the IEEE*, Vol. 77 (2), 1989, pp. 257–286.
10. Weigend, A. S., Gershenfeld, N. A. *Time Series Prediction: Forecasting the Future and Understanding the Past.* Addison-Wesley, 1993.
11. Zhang, Y. Prediction of Financial Time Series with Hidden Markov Models. In: *School of Computer Science, Vol. Master of Applied Science.* Simon Fraser University, 2004
12. Soloviev, V., Saptsin, V., Chabanenko, D. *Prediction of financial time series with the technology of high-order Markov chains*. *Working Group on Physics of Socio-economic Systems (AGSOE).* Dresden, 2009. – URL – http://www.dpg-verhandlungen.de/2009/dresden/agsoe.pdf
   Appendix.

Received on the 1st of September, 2010

Computer Modelling and New Technologies, 2010, Vol.14, No.3, 68–72
Transport and Telecommunication Institute, Lomonosova 1, LV-1019, Riga, Latvia

PERFORMANCE ENHANCEMENT OF DSR PROTOCOL WITH CONGESTION AVOIDANCE MECHANISM FOR MOBILE AD HOC NETWORKS

***A. Valarmathi*[1], *R. M. Chandrasekaran*[2]**

[1]*Department of Computer Applications, Anna University Tiruchirappalli*
Tiruchirappalli-620 024, India

[2]*Department of Computer Science and Engineering, Anna University Tiruchirappalli*
Tiruchirappalli-620 024, India

[1]*valar1030@yahoo.com*, [2]*rmc@sify.com*

Streaming multimedia applications over Mobile Ad Hoc Networks (MANETs) create new challenges to routing protocols in terms of stringent performance requirements. Many routing protocols that have been proposed in the past could not completely address these issues. In the present paper, the original DSR protocol is modified to provide multi-path data transfer during the periods of congestion. NS-2 simulation was used to evaluate the performance of the modified DSR in predefined mobility scenarios. The performance was evaluated using throughput and end-to-end delay and compared with original DSR. The results showed that a significant improvement in the performance of modified DSR was achieved with the use of multi-path routing and congestion avoidance mechanism.

Keywords*: Mobile Ad Hoc Network – DSR-multi-path routing-NS-2*

1. Introduction

In recent years, many studies have been focused on MANETs and the decline in the cost of wireless products [1]. These advancements create new avenue for supporting bandwidth-restricted multimedia applications over wireless networks. To meet these critical requirements, a MANET inherently depends on the routing scheme employed. A multi-path routing scheme might improve the performance of the network in a significant manner. Many variants of multi-path DSR have been proposed in the past. Round trip time measurements are used to distribute load between paths in Multi-path Source Routing (MSR) [2]. A distributed multi-path DSR protocol (MP-DSR) was developed to improve QoS with respect to end-to-end reliability [3]. The protocol forwards outgoing packets along multiple paths that are subjected to an end-to-end reliability model. Split Multi-path Routing (SMR) utilized multiple routes of maximally disjoint paths which minimize route recovery process and control message overhead [4]. Kui Wu and Janelle Harms [5] proposed a path selection criteria and an on-demand multi-path calculation method for DSR protocol. Peter Pham and Sylvie Perreau [6] proposed a multi-path DSR protocol with a load balancing policy which spreads the traffic equally into multiple paths that are available for each source-destination pair. A dynamic load-aware based load-balanced routing (DLBL) algorithm was developed which considers intermediate node routing load as the primary route selection metric [7]. De Rango et al [8] proposed an energy aware multi-path routing protocol by considering minimum drain rate as a metric. Zhang XiangBo and Ki-Il Kim [9] proposed a multi-path routing protocol based on DSR which uses Multi-Probing and Round-Robin mechanisms (MRDSR) for updating alternate multiple paths.

2. Proposed Modifications

Whenever congestion occurs, the multi-path routing is invoked which will select unequal cost paths stored in the secondary cache. The modified DSR protocol transmits a RERR message when the energy level reach 10 percent and the queue reach their capacity of 50 packets. When the nodes in the downstream receive the RERR message, it enables multi-path routing and searches their primary and secondary caches for multiple routes to the intended destination.

3. Simulation Set-up

NS-2 version 2.30 [10] was used to simulate the performance of the modified DSR under different mobility scenarios. The initial battery capacity of each node assumed to be 100%. The battery capacity of a mobile node was decremented in a predefined manner by the txPower and rxPower levels which remains constant throughout the simulation. In order to conform to the IEEE 802.11b specification, the dataRate_ variable was set to 11 Mbps and the basicRate_ variable was set to 1 Mbps. The pre-defined topology was created in a 1200 x 1200 meter grid with 17 nodes. The packet sizes of CBR multimedia streams were fixed at 512 bytes with each node had a maximum queue size of 50 packets. The five destination nodes were placed close to the border of the topology in a circular manner and the two source nodes located at the center. The pause time was varied at 4 and 20 seconds, by keeping the traffic load and data rate constant at 5 CBR and 200 PPS, respectively. This will create low and high mobility scenarios.

4. Performance Metrics

In the present paper, the performance metrics such as average throughput and average end-to-end delay was calculated and evaluated for both normal DSR and modified DSR using the following relationships.

Average Throughput. The average throughput is calculated using the ratio of total number of processed data packets to the total simulation time.

Average end-to-end delay. The average end-to-end delay is a measure of average time taken to transmit each packet of data from the source to the destination. Network congestion is indicated by higher end-to-end delays.

5. Results and Discussion

5.1. Impact of Mobility

5.1.1. Low Mobility Scenario

The throughput of original and modified DSR at low mobility for destination 2 is shown on Figure 1.

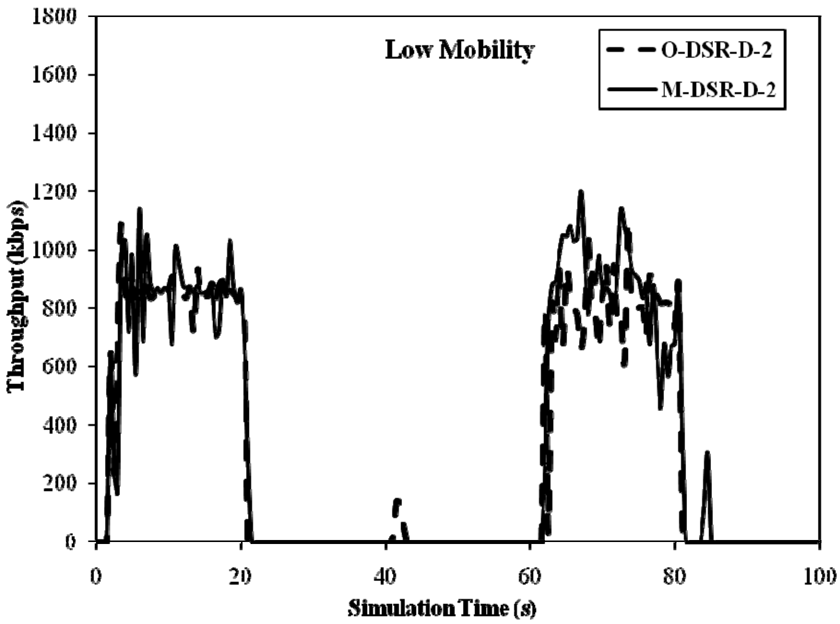

Figure 1. Throughput of original and modified DSR at low mobility for destination 2

A maximum throughput of 1200 kbps was achieved for the original DSR and 1150 kbps for the modified DSR. The performance of both the protocols are similar with little improvement in throughput was achieved when using the modified DSR. In low mobility scenario, the mobile nodes are stationary for a longer duration which may increase the validity of routes. This leads to extended data transfer for longer duration that resulted in higher average throughput in both cases. In addition, the occurrence of peaks is few, however with the increase in the spread of the curve.

The original DSR resulted in higher end-to-end delay at three instances as shown on Figure 2. During initial stages, the route discovery process has led to additional overhead which may lead to delay and when transfer of data continues as simulation progresses, the probability for congestion increases which again resulted in delay. In modified DSR, there is no such peaks were observed which exhibited superior performance compared to original DSR.

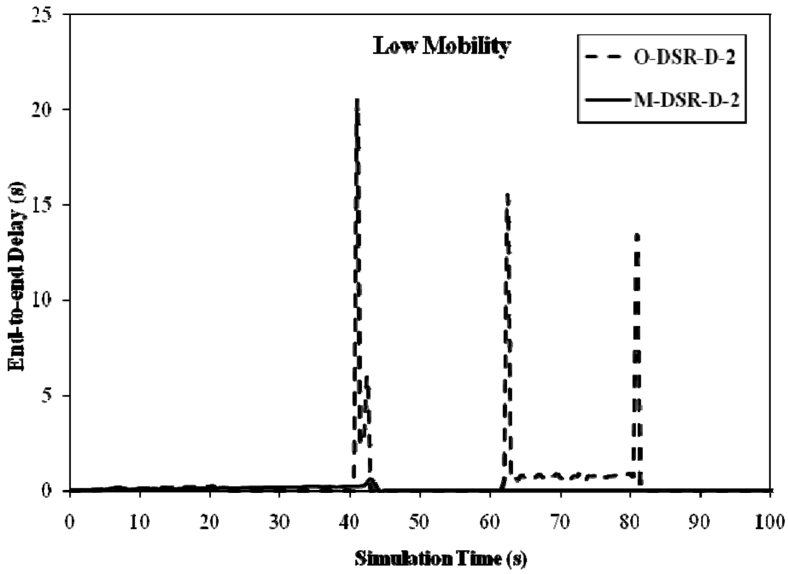

Figure 2. End-to-end delay of original and modified DSR at low mobility for destination 2

5.1.2. High mobility Scenario

In high mobility scenario, the pause time was further reduced to 4 seconds which makes rapid movement of nodes compared to the previous scenarios. An increase in mobility leads to more alternate routes to destination. This may result in better alternative multi hop paths than at low mobility. However, this also results in frequent route failures that lead to considerable routing overhead in searching for alternate routes. These two opposing factors influence the performance of the network. The throughput variations for destination-2 on Figure 3 indicate a notable reduction in throughout value compared to low mobility scenarios.

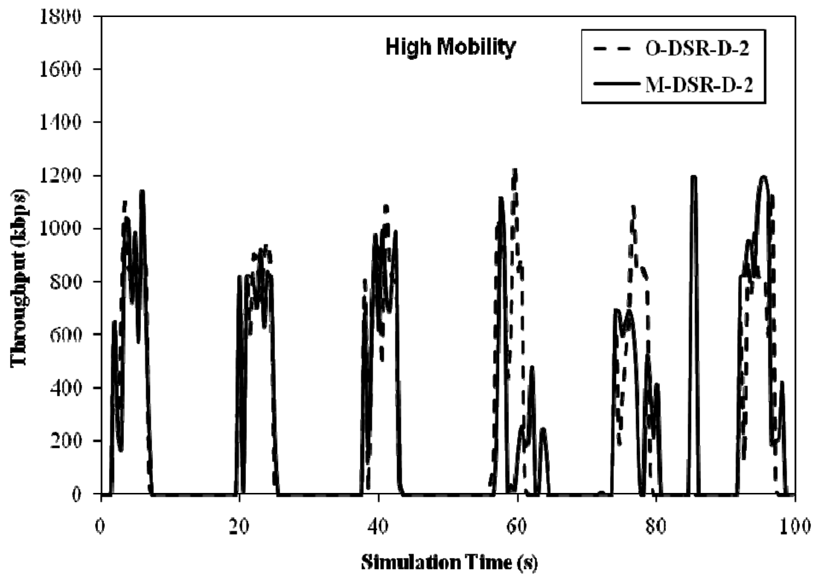

Figure 3. Throughput of original and modified DSR at high mobility for destination 2

However, the instances of peak appearance are higher compared to other scenarios. This discontinuity in data transfer might result from route failures and once a valid route has been found, the transfer of data was continued. The end-to-end delay variations in destinations 2 are shown on Figure 4.

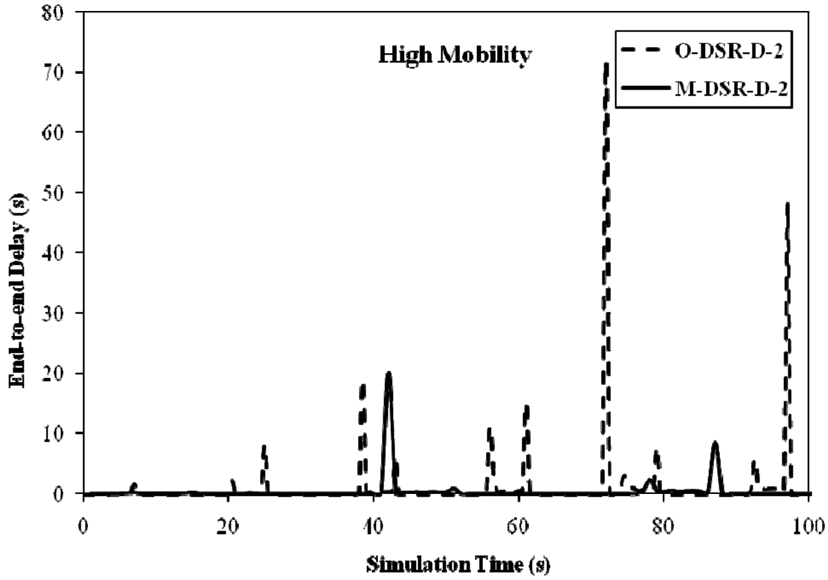

Figure 4. End-to-end delay of original and modified DSR at high mobility for destination 2

The delay is very high towards the end of simulation. This further supports the influence of congestion. In both the cases, the modified DSR exhibit improved performance over original DSR.

Conclusions

The existing DSR protocol was modified to use multi-path routing during the period of congestion. The effectiveness of the usage of multi-path was evaluated using NS-2 simulation by defining predefined mobility scenarios. The performance of the modified DSR was evaluated in terms of throughput and average end-to-end delay; Based on the simulation results, the following conclusion can be drawn.

The impact of mobility on the network performance in a pre-defined scenario was evaluated by varying the pause times. In low mobility, a maximum throughput of 1750 kbps was achieved. The original DSR resulted in higher end-to-end delay during the start and end points of data transfer. In modified DSR, the end-to-end delay is much lower due to the usage of multi-path routing. In high mobility scenario, the throughput is greatly influenced by the excessive routing overhead. However, the instances of peak appearance are higher due to discontinuity in data transfer that might result from route failures. In original DSR, large number of peaks of end-to-end delay appears and towards the end of simulation it is very high. Such peaks are reduced with the use of modified DSR.

References

1. Hoseini, S. A., Budiarto, R. & Wan, T. Survey and new approach in service discovery and advertisement for Mobile Ad Hoc Networks, *IJCSNS*, Vol. 7, 2007, pp. 275–284.
2. Wang, L., Zhang, L., Shu, Ya. & Dong, M. Multipath source routing in wireless ad hoc networks. In: *Proc. Canadian Conference on Electrical and Computer Engineering, Vol. 1*, 2000, pp. 479–483.
3. Leung, R., Jilei, Liu, Poon, E., Chan, A.-L.C. & Baochun, Li. MP-DSR: a QoS-aware multi-path dynamic source routing protocol for wireless ad-hoc networks. In: Proc. *Local Computer Networks, 26th Annual IEEE Conference,* 2001, pp. 132–141.
4. Lee, S.-Ju., Gerla, M. Dynamic load-aware routing in ad hoc networks. In: *IEEE Conference on Communications, Vol. 10*, 2001, pp. 3206–3210.
5. Wu, K. & Harms, J. Performance Study of a Multi-path Routing Method for Wireless Mobile Ad Hoc Network. In: *Proc. 9th IEEE International Symposium on modeling, Analysis, and Simulation of Computer and Telecommunications Systems (MASCOTS'01)*, 2001, pp. 1–7.

6. Pham, P., Perreau, S. Multi-path routing protocol with load balancing policy in Mobile Ad Hoc Network. In: *Proc 4th International Workshop on Mobile and Wireless Communications Network,* 2002, pp. 48–52.
7. Zheng, X., Guo, W., Liu, R., Tian, Yo. A New Dynamic Load-aware Based Load-balanced Routing for Ad Hoc Networks, *IEEE*, 2004, pp. 407–411.
8. De Rango, Lonetti, P., Marano, S. Energy-aware metrics impact on Multipath DSR in MANETs environment. In: *International Symposium on Performance Evaluation of Computer and Telecommunication Systems*, 2008, pp. 130–137.
9. Zhang XiangBo., Ki-Il Kim. Load-aware metric for efficient balancing on multipath DSR protocol in Mobile Ad Hoc Networks. In: *International Conference on Advanced Technologies for Communications,* 2008, pp. 395–398.
10. *The Network Simulator - NS-2.* – http://www.isi.edu/nsnam/ns/.

Received on the 12th of May, 2010

Computer Modelling & New Technologies, 2010, Volume 14, No. 3
Transport and Telecommunication Institute, Lomonosova Str.1, Riga, LV-1019, Latvia

Authors' index

Yuri N. Shunin (born in Riga, March 6, 1951)

- Vice-Rector on Academic Issues (Information Systems Management Institute), professor, Dr.Sc.Habil., Member of International Academy of Refrigeration
- Director of Professional Study Programme Information Systems (Information Systems Management Institute)
- Director of Master Study Programme Computer systems (Information Systems Management Institute)
- **University study**: Moscow physical and technical institute (1968–1974)
- Ph.D. (physics & mathematics) on solid state physics (1982, Physics Institute of Latvian Academy of Sciences), Dr.Sc.Habil (physics & mathematics) on solid state physics (1992, Ioffe Physical Institute of Russian Academy of Sciences)
- **Publications:** 400 publications, 1 patent
- **Scientific activities:** solid state physics, physics of disordered condensed media, amorphous semiconductors and glassy metals, semiconductor technologies, heavy ion induced excitations in solids, mathematical and computer modelling, system analysis

Igor V. Kabashkin (born in Riga, August 6, 1954)

- Vice-rector for Research and Development Affairs of Transport and Telecommunication Institute, Professor, Director of Telematics and Logistics Institute
- PhD in Aviation (1981, Moscow Institute of Civil Aviation Engineering) Dr.Sc.Habil. in Aviation (1992, Riga Aviation University), Member of the International Telecommunication Academy, Member of IEEE, Corresponding Member of Latvian Academy of Sciences (1998)
- **Publications:** 420 scientific papers and 67 patents
- **Research activities:** information technology applications, operations research, electronics and telecommunication, analysis and modelling of complex systems, transport telematics and logistics

Arnold E. Kiv, Professor, Dr.Sc.Habil. (phys&math)

- Chief of Mathematical and Computer Modelling Department
- South Ukrainian Pedagogical University, professor of the Department of Materials Engineering, Ben-Gurion University of the Negev P.O.B. 653, Beer-Sheva, 84105, Israel
- **Scientific activities**: sub-threshold radiation effects in solids. Present scientific activities: computer modelling of processes in physics, psychology and social sciences

N. L. Parthasarathi

- **University Studies**: BSc.E. (Mechanical Engineering), MSc. Tech. (Production Engineering)
- **International Publications**: 9 publications
- **Scientific Activities**: Principal Investigator of Fast track young scientist project sponsored by DST–SERC, New Delhi, India
- **Present position:** Research Scholar, Department of Production Engineering, National Institute of Technology, Tiruchirappalli-620 015, Tamil Nadu, India

M. Duraiselvam

- **University Studies**: BSc.E., (Mechanical Engineering), MSc.E., (Manufacturing Engineering), Ph.D., (Technical University of Clausthal, Germany), Dr.Sc.Ing.
- **International Publications**: 11 publications
- **Scientific Activities**: Principal Investigator of Fast track young scientist project sponsored by DST–SERC, New Delhi, India
- **Present position**: Assistant Professor, Department of Production Engineering, National Institute of Technology, Tiruchirappalli,Tamil Nadu, India 620 015

Ziya Uddin

- Assistant Professor in the Department of Applied Sciences and Humanities, ITM University, Gurgaon, Haryana-122017, India. Earlier he worked as a member of Faculty of Science and Technology, ICFAI University, Dehradun, India
- Ph.D. in Mathematics from G.B. Pant University of Agriculture and Technology, Pantnagar, 263145, India
- Qualification examination CSIR-UGC/NET-JRF, Junior research Fellowship from the Council of Scientific and Industrial Research, New Delhi, India, for his research
- **Research activities**: Computational Fluid Dynamics, Applied Numerical Methods and Mathematical Modelling
- **Publications**: 10 research papers in National and International Journals

Vyacheslav V. Golovanov

- Professor at the Faculty of Physics, South-Ukrainian University, where he is also Director of the Centre for Innovation Technologies, aimed at activities in manufacturing of semiconductor gas instruments
- **Scientific Grades**
  1983 – M.Sc. degree in material science
  1988 – Ph.D. degree in for studies in the fields of surface physics, solid-gas interfaces, and physics of semiconductors
  1998 – Dr.Sc. degree for studies in the fields of surface physics, solid-gas interfaces, and physics of semiconductors, from Odessa National University, Ukraine
- **Research activities**
  ab initio study of chemisorptions and catalytic effects on the surface of semiconductors and sensor systems for environmental monitoring

Dietmar Fink

- **PhD, Dr.Sc.,** Invited Professor of the Physics Department, Universidad Autónoma, Mexico
- Till 2008 a chief of laboratory of Hahn-Meitner Institute, Berlin
- **Research interests:**
  radiation defects including ion tracks, polymer/metal multilayers and interfaces, development of TEMPOS sensing structures
- **Publications:**
  about 410 publications, 14 patents and 4 books

Dinesh C. S. Bisht

- Department of Mathematics at *itm, University Gurgaon,* India
- **University Studies:**
  2004 – M.Sc. degree in Mathematics from Kumaon University, Nainital
  2009 – Ph.D. in Mathematics with major in Mathematics and minor in Electronics and Communication Engineering from G. B. Pant University of Agri. & Technology, Uttarakhand, India in Before joining I.T.M. he worked as visiting faculty at ICFAI Tech. University, Dehradun
- **Research interests:** Artificial Neural Networks, Genetic Algorithm, Fuzzy Logic

Vladimir M. Saptsin (born in Kremenchug, March 28, 1951)

- Associate Professor (Kremenchug State University)
- **University study:**
  Moscow State University (1968–1974)
  Ph.D. (physics & mathematics) on semiconductor physics (1981, Department of Semiconductor Physics, Moscow State University), prepared the dissertation of Doctor of physics and mathematical sciences on solid state physics (1995, Lykov ITMO in Minsk)
- **Publications:** 70 publications
- **Scientific activities:** complex systems modelling, quantum econo-physics, solid state physics, heat-vision physics, semiconductor technologies, mathematical and computer modelling, system analysis

Vladimir N. Soloviev (born in Kriviy Rih, September 15, 1952)

- Chairman of the Economic Cybernetics Department, Professor
- **University study:** Kriviy Rih State Pedagogical University (1970–1975)
- Ph.D. (physics & mathematics) on solid state physics (1981, Leningrad Polytechnical Institute named after M. Kalinin), Doctor (physics & mathematics) on solid state physics (1993, Physics Institute of Ukrainian Academy of Sciences)
- **Publications:** 295 publications
- **Scientific activities:** complex systems modelling, econo-physics, solid state physics, physics of disordered condensed media, amorphous semiconductors and glassy metals, mathematical and computer modelling, system analysis

Dmitry N. Chabanenko (born in Kriviy Rih, January 19, 1984)

- **University study:** Kriviy Rih State Pedagogical University (2001–2006), Post-graduate student (Cherkassy National University named after Bogdan Khmelnitsky)
- **Publications:** 27 publications
- **Scientific activities**: Complex systems, econo-physics, mathematical and computer modelling, system analysis, parallel programming, agent-based modelling

CUMULATIVE INDEX

COMPUTER MODELLING and NEW TECHNOLOGIES, volume 14, No. 3, 2010

(Abstracts)

D. Fink, D. Fuks, A. Kiv, V. Golovanov. Gas Sensor Arrays for Special Applications, *Computer Modelling and New Technologies*, vol. 14, No 3, 2010, pp. 7–11.

Different types of sensor arrays are discussed. Special cases are indicated when the application of sensor arrays is the only one way to solve the problems of the environment protection and defense. Nanotube sensor arrays are reviewed. New perspectives of the novel sensor arrays creation are connected with the development of the track electronics. The main features of the track electronics are indicated. Principal ways are shown that lead to the development of the multifunctional sensor arrays based on track electronics.

Keywords: *sensor arrays, nanotubes sensors, track electronics*

D. Fuks, A. Kiv, A. Nemtsoff. Mechanism of Strengthening of Nanocrystalline Tungsten, *Computer Modelling and New Technologies*, vol. 14, No 3, 2010, pp. 12–16.

The work is aimed to study the influence of interaction between nanocrystals in nanocrystalline tungsten on its mechanical properties. The modified Molecular Dynamics (MD) technique was used to calculate the potential relief (PR) for the mutual shifting of two nanocrystals inside the nanocrystalline tungsten. We considered two tungsten nanocrystals sliding relatively the common interface with one or two vacancies in the sliding lattice planes. It was found that defects in sliding planes lead to increase of potential barrier for mutual shifting of nanocrystals and thus cause the increase of microscopic “friction” in nanocrystalline material. This means that a creation of point defects in contacting layers of nanocrystals can provide the strengthening of such materials.

Keywords: *nanocrystalline materials (NCM), Molecular Dynamics Simulation*, *mechanical properties of nanocrystalline tungsten*

N. L. Parthasarathi, M. Duraiselvam. Effect of Sliding Velocity and Plasma Spraying Parameters on Wear Resistance of NiCrBSiCFe Plasma Sprayed on Austenitic Stainless Steel at High Temperature, *Computer Modelling and New Technologies*, vol. 14, No 3, 2010, pp. 17–29.

The tribological tests were carried out on AISI 316 austenitic stainless steel (ASS) plasma coated with NiCrBSiCFe alloy powder under two set of plasma spraying parameters (PSP 1 and PSP 2) using a pin-on-disc-apparatus. EN 8 medium carbon steel was used as a counterface material. The tests were carried out at load of 20 N with sliding velocities of 1m/s and 2m/s at room temperature (35°), 150°C, 250°C and 350°C. Metallographic characterization was carried out by optical microscope (OM) and Scanning electron microscope (SEM). Between PSP 1 and PSP2, a stand-off distance of 125 mm (PSP1) was found to be more suitable for producing uniform lamellar micro-structure with fewer amounts of pores with better wear resistance. The wear rate at 1m/s was comparatively more than 2m/s due to the adhesive wear and material softening. The worn debris during sliding at 350°C turn in to oxides which further behaves like a protective and lubricative film eliminating the chances of severe material loss. SEM was used to characterise the worn track and to identity the wear mechanism.

Keywords: *AISI 316 ASS, NiCrBSiCFe, sliding velocity, stand-off distance, abrasive wear, plasma spraying*

G. M. Balamurugan, M. Duraiselvam. Influence of Temperature on the Wear Behaviour of WC-Co Plasma Sprayed AISI 304 Austenitic Stainless Steel, *Computer Modelling and New Technologies*, vol. 14, No 3, 2010, pp. 30–40.

The study presented in this paper concerns the influence of the temperature on the wear behaviour of plasma sprayed WC-Co coated AISI 304 austenitic stainless steel (ASS) substrate. With higher hardness and the good adhesion with the substrate, the sprayed coating exhibits a better wear resistance. The deposit was characterized by hardness measurements, micro structural examination, coating density and sliding wear assessment.

Wear experiments were carried out by dry sliding contact of EN-24 medium carbon steel pin as counterpart in a pin-on-disc machine at various condition like room temperature, 100°C, 200°C, 300°C under the load of 30N at 2m/s sliding velocity. The wear rate was dependent on the interaction between applied load and tangential velocity. Compared to the uncoated substrate, the WC-Co coated specimens exhibited improved wear resistance up to 5 times. The study revealed significant weight loss at room temperature and abrupt decrease at high temperatures. From X-ray diffraction analysis (XRD), the wear behaviour at high temperature has been attributed to the formation of a protective oxide layer at the surface during sliding. The worn surfaces, plastic deformation and wear debris were analysed through scanning electron microscopy (SEM) and XRD.

Keywords: *sliding wear, austenitic stainless steel, WC–Co, plasma spraying*

Z. Uddin, M. Kumar. Unsteady Free Convection in a Fluid Past an Inclined Plate Immersed in a Porous Medium, *Computer Modelling and New Technologies*, vol. 14, No 3, 2010, pp. 41–47.

Unsteady free convection in a fluid past an infinite inclined plate immersed in a porous medium has been considered for viscous dissipative heat. The problem is governed by a coupled system of non-linear partial differential equations given by Darcy-Brinkman-Forchheimer model. The velocity profile and temperature distributions have been studied using a finite difference scheme. Boundary layer and Boussinesq approximations have been considered. The effect of different parameters entering in the problem, on velocity profile, temperature distribution, local friction factor and local Nusselt number have been computed and studied with the help of graphs. It is observed that as the angle of the plate from vertical direction increases, the value of friction factor and heat transfer coefficients decreases. This problem is interesting for the researchers belonging to chemical and related industry.

Keywords: *viscous dissipation, unsteady free convection, inclined plate, porous medium, non-linear partial differential equations, explicit finite-difference scheme*

D. C. S. Bisht, M. M. Raju, M. C. Joshi. Ann Based River Stage – Discharge Modelling for Godavari River, India, *Computer Modelling and New Technologies*, vol. 14, No 3, 2010, pp. 48–62.

The present study was carried out to develop river stage discharge modelling using Artificial Neural Network (ANN) and Linear Multiple Regression (LMR) methods. From the literature and the developed models, it is clear that ANN models for river stage-discharge are more efficient than the other traditional modelling methods. Twenty ANN models were developed in the study in which ten models were one hidden layer models and ten models with two hidden layers. The best five ANN models were selected in each one hidden layer methodology and two hidden layers methodology. Finally five best ANN models out of all the developed ANN models were selected.

The developed models were trained, tested & validated on the data of Godavari River at Rajahmundry, Dhawalaishwaram Barrage site in Andhra Pradesh. Comparing observed data and the estimated data through developed ANN models, it has been proved that the developed ANN models show good results and are better than the traditional models, like LMR.

Keywords: *artificial neural network, training, testing, validation, learning, stage-discharge*

V. Soloviev, V. Saptsin, D. Chabanenko. Financial Time Series Prediction with the Technology of Complex Markov Chains, *Computer Modelling and New Technologies*, vol. 14, No 3, 2010, pp. 63–67.

In this research the technology of complex Markov chains, i.e. Markov chains with a memory is applied to forecast financial time-series. The main distinction of complex or high-order Markov Chains [1] and simple first-order ones is the existing of after effect or memory. The high-order Markov chains can be simplified to first-order ones by generalizing the states in Markov chains. Considering the "generalized state" as the sequence of states makes a possibility to model high-order Markov chains like first-order ones. The adaptive method of defining the states is proposed, it is concerned with the statistic properties of price returns [2]. According to the fundamental principles of quantum measurement theories, the measurement procedure impacts not only on the result of the measurement, but also on the state of the measured system, and the behaviour of this system in the future remains undefined, despite of the precision of the measurement. This statement, in our opinion, is general and is true not only for physical systems, but to any complex systems [3].

Keywords: *high-order Markov chains, financial time-series*

A. Valarmathi, R. M. Chandrasekaran. Performance Enhancement of DSR Protocol with Congestion Avoidance Mechanism for Mobile Ad Hoc Networks, *Computer Modelling and New Technologies*, vol. 14, No 3, 2010, pp. 68–72.

Streaming multimedia applications over Mobile Ad Hoc Networks (MANETs) create new challenges to routing protocols in terms of stringent performance requirements. Many routing protocols that have been proposed in the past could not completely address these issues. In the present paper, the original DSR protocol is modified to provide multi-path data transfer during the periods of congestion. NS-2 simulation was used to evaluate the performance of the modified DSR in predefined mobility scenarios. The performance was evaluated using throughput and end-to-end delay and compared with original DSR. The results showed that a significant improvement in the performance of modified DSR was achieved with the use of multi-path routing and congestion avoidance mechanism.

Keywords: *Mobile Ad Hoc Network – DSR-multi-path routing-NS-2*

COMPUTER MODELLING and NEW TECHNOLOGIES, 14.sējums, Nr. 3, 2010
(Anotācijas)

D. Finks, D. Fuks, A. Kivs, V. Golovanovs. Gāzes sensoru sakārtojums speciāliem pielietojumiem, *Computer Modelling and New Technologies,* 14.sēj., Nr.3, 2010, 7.–11. lpp.

Rakstā tiek izskatīti dažādi sensoru sakārtojuma veidi. Tiek norādīti īpaši gadījumi, ja sensoru sakārtojuma pielietošana ir vienīgais veids, kā risināt vides aizsargāšanas problēmas. Nano-cauruļu sensoru sakārtojums tiek izskatīts. Nebijušu sensoru sakārtojumu radīšanas jaunās perspektīvas tiek saistītas ar ierakstu elektronikas attīstību. Galvenās ierakstu elektronikas īpašības tiek parādītas. Principiālie veidi ir parādīti, kas ved uz daudzfunkcionālu sensoru sakārtojumu attīstību, bāzētu uz ierakstu elektroniku.

Atslēgvārdi: *sensoru sakārtojums, nano-cauruiļu sensori, ierakstu elektronika*

D. Fuks, A. Kivs, A. Nemtsofs. Nano-kristāliskā volframa stiprināšanas mehānisms, *Computer Modelling and New Technologies,* 14.sēj., Nr.3, 2010, 12.–16. lpp.

Raksta mērķis ir izpētīt savstarpējās iedarbības starp nanokristāliem nanokristāliskajā volframā uz tā mehāniskajām īpašībām.

Tiek pielietota modificētā Molekulāro Dinamiku (MD) tehnika, lai aprēķinātu – potenciālo atvieglojumu (*angl.* potential relief (PR)) savstarpējai divu nanokristālu nanokristāliskajā volframā pārvietošanos. Autori izskatīja divus volframa nanokristālus, izbīdot nosacīti kopējam interfeisam ar vienu vai divām vakancēm bīdāmajā restes plaknē. Tika konstatēts, ka defekti bīdāmajās plaknēs palielina savstarpējās pārvietošanās potenciālo barjeru un tādējādi izsauc mikroskopiskas frikcijas palielinājumu nanokristāliskajā materiālā. Tas nozīmē, ka punkta defekta nanokristālu kontaktu slāņos radīšana var veicināt šādu materiālu stiprināšanu.

Atslēgvārdi: *nanokristāliskie materiāli, Molekulārās Dinamikas simulācija, nanokristāliskā volframa mehāniskās īpašības*

N. L. Partasarati, M. Duraiselvam. Slīdēšanas ātruma ietekme un plazmas smidzināšanas parametri uz NiCrBSiCFe plazmas, izsmidzinātas uz austenīta nerūsējošo tēraudu, nodilumizturība pie augstas temperatūras, *Computer Modelling and New Technologies,* 14.sēj., Nr.3, 2010, 17.–29. lpp.

Pētījumā tika veikti triboloģiskie testi uz AISI 316 austenīta nerūsējošā tērauda plazmas, pārklātas ar NiCrBSiCFe sakausējuma pulveri pie divu kārtu plazmas izsmidzināšanas parametriem (PSP 1 un PSP 2), pielietojot piespraustu uz diska aparātu. EN 8 vidēja oglekļa tērauds tika lietots kā pretspēka materiāls. Testi tika veikti pie 20 N sloga ar slīdošiem ātrumiem 1m/s un 2 m/s pie istabas temperatūras (35°), 150°C, 250°C un 350°C. Metalogrāfijas raksturojums tika veikts ar optiskā mikroskopa (OM) un skenēšanas elektronu mikroskopa (SEM) palīdzību. Starp PSP1 un PSP2 125 mm (PSP1) attālā distance tika atklāta kā vairāk piemērota veidot uniformu slāņainu mikrostruktūru ar mazāka daudzuma porām un labāku nodilumizturību.

Atslēgvārdi: *AISI 316 ASS; NiCrBSiCFe; slīdošs ātrums; attālā distance; plazmas izsmidzināšana*

G. M. Balamurugan, M. Duraiselvam. Temperatūras ietekme uz WC-Co plazmas nodiluma režīmu, apsmidzinot AISI 304 nerūsējoša austenīta tēraudu, *Computer Modelling and New Technologies,* 14.sēj., Nr.3, 2010, 30.–40. lpp.

Pētījums, kas tiek parādīts šajā rakstā skar temperatūras ietekmi uz plazmas nodiluma režīmu, izsmidzinātu WC-Co, pārklātu ar AISI 304 austenīta nerūsējoša tērauda substrātu. Ar augstāku cietību un labu salipšanu ar substrātu, izsmidzinātais pārklājums uzrāda labāku nodiluma rezistenci. Nogulsnes tika raksturotas ar cietības lielumiem, mikro strukturālo pārbaudi, pārklājuma blīvumu un slīdes nodiluma vērtējumu.

Nodiluma eksperimenti tika veikti ar sausas slīdes kontaktu EN-24 vidēja oglekļa tērauda tapas kā dublikāta *in a pin-on-disc-machine* pie dažādiem apstākļiem, tādiem kā istabas temperatūrā, 100°C, 200°C, 300°C pie sloga 30N slīdes ātrumā 2m/s. Nodiluma ātrums ir atkarīgs no savstarpējās darbības starp pielietoto slogu un tangenciālo ātrumu. Salīdzinot ar nepārklāto substrātu, WC-Co pārklātās daļas uzrādīja uzlabotu nodiluma rezistenci pat līdz 5 reizēm. Pētījums atklāja nozīmīgu svara zudumu istabas temperatūrā un pēkšņu lejupslīdi pie augstām temperatūrām.

Nodiluma virsmas, plastikāta deformācija un nodiluma drupas tika analizētas ar skenēšanas elektronu mikroskopijas palīdzību un ar rentgenstaru difrakcijas analīzi.

Atslēgvārdi: *slīdes nodilums, austenīta nerūsējošs tērauds, WC-Co, plazmas izsmidzināšana*

Z. Udins, M. Kumars. Nestabila brīva konvekcija šķidrumā gar slīpu plātni, iegremdētu porainā vidē, *Computer Modelling and New Technologies,* 14.sēj., Nr.3, 2010, 41.–47. lpp.

Nestabila brīva konvekcija šķidrumā gar neierobežotu slīpu plātni, iegremdētu porainā vidē, tiek izskatīta viskozam izkliedētam karstumam. Problēma tiek regulēta ar nelineāru parciālu diferenciālvienādojumu pāru sistēmu, ko sniedz Darcy-Brinkman-Forchheimer modelis. Ātruma diagramma un temperatūras distribūcijas tiek pētītas ar ierobežotu atšķirību shēmu. Robežas slānis un Boussinesq aproksimācijas tiek izskatītas. Dažādo parametru efekts, kas parādās izskatāmajā problēmā, ātruma diagrammā, temperatūras sadalījumā, lokālā frikcijas faktorā un lokālā Nusselt skaitlī, tiek aprēķināts un pētīts ar grafu palīdzību. Ir novērots, ka, ja plātnes leņķis no vertikālā stāvokļa palielinās, frikcijas faktora vērtība un karstuma vadāmības koeficienti samazinās. Šis jautājums interesē pētniekus, kas nodarbojas ar ķīmisko un ar to saistīto ražošanu.

Atslēgvārdi: *viskozā izkliede, nestabilā brīvā konvekcija, noliekta plātne, poraina vide, nelineārs parciāls diferenciālvienādojums*

D. C. S. Bišts, M. M. Raju, M. C. Joši. Upes posms, pamatots uz mākslīgo neironu tīklu (*ANN*) – izplūdes modelēšana Godavari upei, Indija, *Computer Modelling and New Technologies,* 14.sēj., Nr.3, 2010, 48.–62. lpp.

Dotais pētījums ir veikts, lai attīstītu upes posma izplūdes modelēšanu, pielietojot Mākslīgā Neironu Tīkla (ANN) un Lineārās Multiplās Regresijas (LMR) metodi. Pēc literatūras un attīstītiem modeļiem ir skaidrs, ka ANN modeļi upes posma izplūdei ir efektīvāki nekā citas tradicionālās modelēšanas metodes. Divdesmit ANN modeļi tika attīstīti pētījumā, kurā desmit bija viena noslēpta slāņa modeļi un desmit modeļi ar diviem slēptiem slāņiem. Vislabākie pieci ANN modeļi tika atlasīti katrā viena slēptā slāņa metodoloģijā un divu slēptu slāņu metodoloģijā. Visbeidzot, tika atlasīti pieci vislabākie ANN modeļi no visiem attīstītiem ANN modeļiem.

Attīstītie modeļi tika studēti, testēti un apstiprināti pēc Godavari upes datiem Rajahmundri, Dhawalaishwaram Barrage rajonā pie Andhra Pradesh, Indijā. Salīdzinot novērotos datus un sasniegtos rezultātus ar ANN modeļu palīdzību, tika pierādīts, ka attīstītie ANN modeļi parāda labus rezultātus un ir labāki nekā tradicionālie modeļi, tādi kā LMR.

Atslēgvārdi: *Mākslīgais Neironu Tīkls, studēšana, testēšana, vērtēšana, mācīšana, posma izplūde*

V. Solovjevs, V. Sapcins, D. Čabaņenko. Finansiālu laika sēriju paredzējums ar Markova ķēžu kompleksa tehnoloģiju, *Computer Modelling and New Technologies,* 14.sēj., Nr.3, 2010, 63.–67. lpp.

Šajā pētījumā Markova ķēžu kompleksa tehnoloģija, t.i., Markova ķēdes ar atmiņu tiek pielietotas, lai paredzētu finansiālās laika sērijas. Kompleksa galvenā īpatnība vai augstas secības Markova ķēdes un vienkāršas vienas secības ķēdes ir pēc efekta vai atmiņas eksistējošas. Augstas secības Markova ķēdes var tikt vienkāršotas līdz vienas secības ķēdēm, vispārinot stāvokļus Markova ķēdēs. Apskatot 'vispārinātos stāvokļus' kā stāvokļu secību, tiek dota iespēja modelēt augstas secības Markova ķēdes kā vienas secības ķēdes. Tiek piedāvāta adaptīvā stāvokļa noteikšanas metode, tā tiek saistīta ar cenu apgrozījuma statistiskām īpašībām [2]. Saskaņā ar kvantuma mērīšanas teoriju fundamentāliem principiem, mērīšanas procedūra ietekmē ne tikai mērījuma rezultātu, bet arī mērījamās sistēmas stāvokli, un šīs sistēmas uzvedība nākotnē paliek nenoteikta, par spīti mērījuma precizitātei, Šis stāvoklis, pēc mūsu domām, ir vispārējs un ir patiess ne tikai fizikālām sistēmām, bet jebkurai kompleksai sistēmai [3].

Atslēgvārdi: *augstas secības Markova ķēdes, finansiālās laika sērijas*

A. Valarmathi, R. M. Čandrasekaran. *DSR* protokola efektivitātes palielināšana ar mehānisma pārslodzes izvairīšanos mobilajiem speciālajiem tīkliem, *Computer Modelling and New Technologies,* 14.sēj., Nr.3, 2010, 68.–72. lpp.

Straumēšanas multimediju lietošana caur Mobilajiem Ad Hoc Tīkliem rada jaunus izaicinājumus maršrutēšanas protokoliem stingras veiktspējas prasības apstākļos. Daudzi maršrutēšanas protokoli, kas ir piedāvāti kādreiz, nevarētu būt pilnībā adresēti šīm publikācijām. Dotajā rakstā Oriģinālais *DSR* protokols ir pārveidots, lai nodrošinātu daudz-celiņu datu pārvietošanai pārblīves perioda laikā. *NS*-2 simulācija bija lietota, lai izvērtētu pārveidotā *DSR* veiktspēju iepriekš noteiktajā mobilitātes scenārijā. Veiktspēja bija novērtēta, lietojot pamatīgi liktu un beigu pie beigām aizkavi un, salīdzinot ar oriģinālo *DSR*. Rezultāti parādīja, ka nozīmīgs uzlabojums pārveidotā *DSR* veiktspējā bija panākts ar daudz-celiņu maršrutēšanas un pārblīves izvairīšanās mehānisma lietojumu.

Atslēgvārdi: *Mobilais Ad Hoc Tīkls – DSR daudz-celiņu maršrutēšana -NS-2*

COMPUTER MODELLING & NEW TECHNOLOGIES

ISSN 1407-5806 & ISSN 1407-5814(on-line)

Host Organization:
Transport and Telecommunication Institute

Supporting Organizations:
Latvian Transport Development and Education Association
Latvian Academy of Sciences
Latvian Operations Research Society

THE JOURNAL IS DESIGNED FOR PUBLISHING PAPERS CONCERNING THE FOLLOWING FIELDS OF RESEARCH:

- mathematical and computer modelling
- mathematical methods in natural and engineering sciences
- physical and technical sciences
- computer sciences and technologies
- semiconductor electronics and semiconductor technologies
- aviation and aerospace technologies
- electronics and telecommunication
- navigation and radar systems
- telematics and information technologies
- transport and logistics
- economics and management
- social sciences

In journal articles can be presented in English. All articles are reviewed.

EDITORIAL CORRESPONDENCE

Transporta un sakaru institūts (Transport and Telecommunication Institute)
Lomonosova iela 1, LV-1019, Riga, Latvia. Phone: (+371) 67100593. Fax: (+371) 67100535.
E-mail: journal@tsi.lv, www.tsi.lv

COMPUTER MODELLING AND NEW TECHNOLOGIES, 2010, Vol. 14, No.3

Scientific and research journal of Transport and Telecommunication Institute (Riga, Latvia)
The journal is being published since 1996.

PREPARATION OF CAMERA-READY TYPESCRIPT: COMPUTER MODELLING AND NEW TECHNOLOGIES

1. In order to format your manuscript correctly, see the Page Layout Guideline for A4 (21 cm x 29,7 cm) paper size. Page Layout should be as follows: Top – 3 cm, Bottom – 3 cm, Left – 3 cm, Right – 3 cm.
2. Maximum length for the article is 10 pages.
3. **Application of other Styles with the exception of Normal is impossible!**
4. ***Articles*** should be Times New Roman typeface, single-spaced.
5. The article should include:
   - title;
   - author's name(s) and information (organisation, city, country, present address, phones, and e-mail addresses);
   - abstract (100–150 words);
   - keywords (max. about six);
   - introduction – clearly explaining the nature of the problem, previous work, purpose and contribution of the research;
   - description of proper research;
   - conclusion section (this is mandatory) which should clearly indicate advantages, limitations and possible applications;
   - references.

   Attention! First name, last name, the title of the article, abstract and keywords must be submitted in the English and Latvian languages (in Latvian it is only for Latvian authors) as well as in the language of the original (when an article is written in different language).
6. The text should be in clear, concise English (or other declared language). Please be consistent in punctuation, abbreviations, spelling (***British English***), headings and the style of referencing.
7. ***The title of the article*** – 14 point, UPPERCASE, style Bold and centred.
8. ***Author's names*** – centred, type size 12 point, Upper and lower case, style Bold Italic.
9. ***Author's information*** – 10 point, Upper and lower case, style Italic, centred.
10. ***Abstract and keywords*** – 8 point size, style Normal, alignment Justify.
11. ***The first level Headings*** – 11 point, Upper and lower case, style Bold, alignment Left. Use one line space before the first level Heading and one line space after the first level Heading.
12. ***The second level Headings*** – 10 point, Upper and lower case, style Bold, alignment Left. One line space should be used before the second level Heading and 1/2 line space after the second level Heading.
13. ***The third level Headings*** – 10 point, Upper and lower case, style Italic, alignment Left. One line space should be used before the second level Heading and 1/2 line space after the third level Heading.
14. ***Text*** of the article – 10 point, single-spaced, alignment Justify.
15. The set of ***formulas*** on application of fonts, signs and a way of design should be uniform throughout the text. The set of formulas is carried out with use of editors of formulas MS Equation 3.0 or MathType. The formula with a number – the formula itself should be located on the left edge of the text, but a number – on the right. Font sizes for equations are: 11pt – full, 7pt – subscripts/superscripts, 5pt – sub- subscripts/superscripts, 16pt – symbols, 11pt – subsymbols.
16. All ***Figures*** – must be centred. Figure number and caption always appear below the Figure, type size 8 point.

Figure 1. This is figure caption

Diagrams, Figures and Photographs – must be of high quality, в in format *.TIFF, *.JPG, *.BMP with resolution not less than 300 dpi. Also formats *.CDR, *.PSD are possible. Combination of Figures in format, for instance, *.TIFF with elements of the in-built Figure Editor in MS Word is prohibited.

17. ***Table Number and Title*** – always appear above the Table. Alignment Left. Type size 8 point. Use one line space before the Table Title, one line space after the Table Title and 1/2 line space after the Table.

Table 1. This is an example of a Table

Heading	**Heading**	**Heading**
Text	Text	Text
Text	Text	Text

18. ***References*** in the text should be indicated by a number in square brackets, e.g. [1].
References should be numbered in the order cited in the manuscript. The correct format for references is the following:

Article: author, title, journal (in italics), volume and issue number, year, inclusive pages

Example: 1. Amrahamsson, M., Wandel, S. A Model of Tearing in Third – Party Logistics with a Service Parts Distribution Case Study, *Transport Logistics*, Vol. 1, No 3, 1998, pp. 181-194.

Book: author, title (in Italics), location of publishers, publishers, year

Example: 2. Kayston, M. and Fried, W. R. *Avionic Navigation Systems.* New York: John Wiley and Sons Inc, 1969.

Conference Proceedings: author; title of an article; proceedings (in italics); title of a conference, date and place of a conference; publishing house, year, pages.

Example: 3. Canales Romero J. A First Step to Consolidate the European Association of Aerospace Students in Latvia (Presented by the Munich Local Group). In: *Research and Technology – Step into the Future: Program and Abstracts. Research and Academic Conference, Riga, Latvia, April 7-11, 2003, Transport and Telecommunication Institute.* Riga: TTI, 2003, p. 20.

19. ***Authors Index***
Editors form the author's index of a whole Volume. Thus, all contributors are expected to present personal colour photos with the short information on the education, scientific titles and activities.
20. ***Acknowledgements***
Acknowledgements (if present) mention some specialists, grants and foundations connected with the presented paper. The first page of the contribution should start on page 1 (right-hand, upper, without computer page numbering). Please paginate the contributions, in the order in which they are to be published. Use simple pencil only.
21. **Articles poorly produced or incorrectly formatted may not be included in the proceedings**.